MECHANICAL REGULATION OF BONE REGENERATION AND VASCULAR GROWTH IN VIVO

A Dissertation
Presented to
The Academic Faculty

By
Joel D. Boerckel

In Partial Fulfillment
of the Requirements for the Degree
Doctorate of Philosophy in the
George W. Woodruff School of Mechanical Engineering

Georgia Institute of Technology
August 2011

MECHANICAL REGULATION OF BONE REGENERATION AND VASCULAR GROWTH IN VIVO

Approved by:

Dr. Robert E. Guldberg, Advisor
School of Mechanical Engineering
Georgia Institute of Technology

Dr. Rudolph L. Gleason
School of Mechanical Engineering
Department of Biomedical Engineering
Georgia Institute of Technology

Dr. Evan A. Zamir
School of Mechanical Engineering
Georgia Institute of Technology

Dr. Andrés J. García
School of Mechanical Engineering
Georgia Institute of Technology

Dr. W. Robert Taylor
Division of Cardiology, School of Medicine
Department of Biomedical Engineering
Emory University

Date Approved: April 27, 2011

To Monica, for her gracious support,
and to the one to come.

ACKNOWLEDGEMENTS

It is the glory of God to conceal a matter, to search out a matter is the glory of kings. Proverbs 25:2.

I would first like to express my sincere gratitude and respect for my advisor, Dr. Robert Guldberg. I was told by several people before coming to graduate school that the choice of an advisor is the single most important decision of one's graduate career. That advice was both wise and true. I have been blessed to spend the last 5 years working with Bob and have been challenged beyond anything I have ever experienced but also encouraged and mentored, and I owe a great deal of the intellectual and scientific growth I experienced here to him. It is a real honor to be a Guldberg lab alumnus.

I would also like to thank my thesis committee for their challenging questions which forced me to carefully consider results and conclusions, but also for their backing and support. Many thanks to Andrés for his continual encouragement, especially through the "brutal" years in which none of my experiments worked, but also for pushing me to dig deeper and ask the question "why?" Thanks to Bob T for asking the hard questions and forcing me to confront my results and take caution with my words. I would like to thank Rudy for his encouragement, both in and out of the lab, and for his excellent example of what it looks like to be a truly excellent researcher and a committed believer in Christ. Thanks also to Rudy for mentoring me in my teaching practicum, and for helping me understand how to be a great teacher. Finally, I would like to thank Evan for our many conversations regarding molecular mechanisms and techniques as well as theoretical solid mechanics.

None of this work would have been possible without the help of the entire Guldberg lab. The collegial and collaborative environment here is truly remarkable. Some of my fondest memories surround the excitement and stress of long surgery days and then the post-data-collection discussions and analyses. There have been many early mornings, late nights and weekends that these have given up for me. I can only hope I was able to repay even a little of all the time and effort and encouragement that they all have been to me. I would like to particularly thank Dr. Yash Kolambkar and Dr. Ken Dupont for their mentoring, friendship, ideas, and commiseration through the difficulties of the Ph.D. They are the giants on whose shoulders I stand (a literal giant in Ken's case). I would also like to especially thank Angela Lin, for her incredible expertise with microCT and her remarkable generosity with her time in teaching me – I'm sure I asked the same IPL questions over and over, but she never told me to go away. It was a great pleasure being office-mates and getting to know you, Angela. Thanks also to Brent Uhrig for his ever-willingness to help in surgery, perfusions, or anything else. Thanks to Jessica O'Neal for the data discussions and for introducing me to skewness and kurtosis. Thanks to Jason for the Matlab script that saved us all so much time. Thanks also to Dr. Nick Willet for his expertise in the vascular world. In a few years, we will be the same person. Thanks also for encouraging me to celebrate the milestones and victories. Finally, I would like to thank everyone else in the lab, all of whom have contributed significantly to the success of this work: Dr. Tamim Diab, Chris Dosier, Dr. Mela Johnson, Dr. Megan Oest, and to our latest additions, Ashley Allen, Tanushree Thote, Alice Mon Tzu Li, and Lauren Priddy – I encourage you to maintain the collaborative lab atmosphere; I know the lab continues in capable hands.

Many thanks also to the other members of Wing 2D: thank you for making this such a fun place to work, and one in which science is shared, not hoarded. Particular thanks to Ed Phelps, whose help on the protein tracking study was invaluable. What took a couple days for him would have taken me many months. Thanks also to Dave Dumbauld for the fun conversations about research and cell adhesion mechanics.

I would also like to recognize the hard work of the many IBB and PRL staff members who went out of their way to help me. Thanks to Dr. Laura O'Farrell for assistance in the animal studies, to Vivian for working through all the ordering headaches, Aqua for her help with histology, Kim and Andrea for taking care of our precious animals, and to Allan for the bike rides.

Finally, I want to thank my family for all of their support over the years. To Mom and Dad A., for letting their daughter marry a student with no immediate end in sight, and for their constant love and support. Thanks to Mom and Dad B. for their consistent affirmation and encouragement. Thanks to my brothers, Mark and Wyn, for being excited to hear about my life and work and for all the great times together. Mark, I'm glad we got to live close, if only for a year.

Lastly, and mostly, I would like to thank my amazing wife, Monica. Thank you for all your love and support, for your longsuffering patience through the years of 'failed' experiments and the incredible stress of qualifying exams. You gave up your dreams for mine, and I can't express my gratitude.

It truly is the glory of kings.

TABLE OF CONTENTS

LIST OF TABLES

LIST OF FIGURES

LIST OF SYMBOLS AND ABBREVIATIONS

rhBMP-2	recombinant human bone morphogenetic protein-2
BMP	Bone morphogenetic protein
Ihh	Indian hedgehog
Runx2	Runt-related transcription factor-2 (also know as Cbfa-1)
VEGF	Vascular endothelial growth factor
pQCT	peripheral quantitative computed tomography
BMU	Basic multicellular unit
LCS	Lacunar-canalicular system
FAK	Focal adhesion kinase
NO	Nitric oxide
cGMP	cyclic guanosine monophosphate
cAMP	cyclic adenosine monophosphate
PKA	Protein kinase A
PKB	Protein kinase B (also known as Akt)
PKC	Protein kinase C
PKG	Protein kinase G
PLC	Phospo-lipase C
PI-3K	Phosphatydilinositol-3 kinase
PIP_3	Phosphatydilinositol 3,4,5-triphosphate
IP_3	Inositol triphosphate
DAG	Diacylglycerol
MAPK	Mitogen-activated protein kinase

GSK-3β	Glycogen synthase kinase-3β
LRP5/6	Low-density lipoprotein receptor-related protein 4/5
GTPase	Guanosine triphosphatase
RhoA	Ras homolog gene family, member A
ROCK	Rho-associated coiled-coil containing protein kinase
ERK	Extracellular-related kinase
$G_{\alpha s}$	G_s protein alpha subunit
COX2	Cyclo-oxygenase-2
ATP	Adenosine triphosphate
Akt	Also known as PKB
PDGFRα	Platelet-derived growth factor receptor alpha
NFκB	Nuclear factor κ-light-chain-enhancer of activated B cells
JNK	c-Jun N-terminal kinase
US	United States of America
FDA	Food and Drug Administration
DFO	Desferioxamine
HIF-1α	Hypoxia-inducible factor-1α
OP-1	Osteogenic protein-1 (also known as BMP-7)
DBM	Demineralized bone matrix
PLA	Phospholipase A
PGA	Polyglycolic acid
TCP	tricalcium phosphate
HA	Hydroxyapatite

PEG	Poly-ethylene glycol
RGD	Argenine-Glycine-Apartic acid
IACUC	Institutional animal care and use committee
PCL	Poly(ε-caprolactone)
PBS	Phosphate buffered saline
VOI	Volume of interest
H&E	Haematoxylin and Eosin
GAG	Glycosaminoglycan
NIR	Near-infrared
95% CI	95% confidence interval
SDS-PAGE	Sodium dodecyl sulfate polyacrilamide gel electrophoresis
CM	Control medium
Dex	Dexamethasone
NS	Not significant
pMOI	polar moment of inertia
FE	Finite element
BW	Body weight
SEM	Standard error of the mean
ANOVA	Analysis of variance
ANCOVA	Analysis of covariance
FEA	Finite element analysis
CT	computed tomography
microCT	microcomputed tomography

PLDL	Poly(L-lactide-*co*-D,L-lactide 70:30)
BV	Bone volume
α-MEM	Minimum essential medium α
RSA	Rat serum albumin
2D	two-dimensions
3D	three-dimensions
TRAP	Tartrate-resistant acid phosphatase

SUMMARY

Regeneration of large bone defects presents a critical challenge to orthopaedic clinicians as the current treatment strategies are severely limited. Tissue engineering has therefore emerged as a promising alternative to bone grafting techniques. This approach features the delivery of bioactive agents such as stem cells, genes, or proteins using biomaterial delivery systems which together stimulate endogenous repair mechanisms to regenerate the tissue. Because bone is a highly mechanosensitive tissue which responds and adapts dynamically to its mechanical environment, application of mechanical stimuli may enhance endogenous tissue repair. While mechanical loading has been shown to stimulate bone fracture healing, the ability of loading to enhance large bone defect regeneration has not been evaluated.

The goal of this thesis was to evaluate the ability of sustained osteogenic growth factor delivery and functional biomechanical loading to stimulate vascularized repair of large bone defects in a rat segmental defect model. First, we evaluated the hypothesis that the relationship between protein dose and regenerative efficacy depends on delivery system. We determined the dose-response relationship between dose of recombinant human bone morphogenetic protein-2 (rhBMP-2) and bone regeneration in a hybrid alginate-based protein delivery system and compared with the current clinically-used collagen sponge. The hybrid delivery system improved bone formation and reduced the effective dose due to its sustained delivery properties in vivo. Next, we tested the hypothesis that transfer of compressive ambulatory loads during segmental defect repair enhances bone formation and subsequent limb regeneration. We found that delayed application of axial loads enhanced bone regeneration by altering bone formation, tissue

differentiation and remodeling, and local strain distribution. Finally, we evaluated the hypothesis that in vivo mechanical loading can enhance neovascular growth to influence bone formation. We found that early mechanical loading disrupted neovascular growth, resulting in impaired bone healing, while delayed loading induced vascular remodeling and enhanced bone formation.

Together, this thesis presents the effects of dose and delivery system on BMP-mediated bone regeneration and demonstrates for the first time the effects of in vivo mechanical loading on vascularized regeneration of large bone defects.

CHAPTER I: SPECIFIC AIMS

INTRODUCTION

The skeletal system is unique in its capacity for scar-free regeneration after injury through the mechanosensitive processes of bone modeling and remodeling, with the local mechanical environment determining the course and success of healing [1-2]. Other factors that influence the repair process, particularly in situations of challenging trauma or disease, include proper biological signals and sufficient vascularization. Like bone, the cardiovascular system is also regulated by mechanical conditions, as blood vessels and endothelial cells remodel and reorient in response to mechanical stimuli [3-4]. In addition, the regenerative processes of osteogenesis and angiogenesis are linked at both the cellular and molecular levels, and the responses of bone and vascular cells to mechanical conditions have been shown to be co-regulated in vitro [5]. However, despite such evidence that the local mechanical environment acutely influences bone healing and vascularization, the ability of mechanical stimulation to enhance vascularized large bone defect repair has not yet been studied.

Large bone defects exceeding 3 cm in length represent a particularly challenging problem for orthopaedic clinicians [6-7]. The gold standard of care, the autograft, in which bone graft particles are surgically transplanted from the patient's iliac crest, is limited by the available volume of graft material and significant donor site morbidity [8-9]. Therefore, structural bone allografts are often used clinically to bridge the defects; however, a high complication rate is directly attributable to their limited ability to revascularize and remodel [10]. Tissue engineering has therefore emerged as a promising alternative to grafting techniques. Numerous tissue engineering studies in vitro have

demonstrated the importance of the mechanical environment for tissue formation and maintenance [11-13]; however, the ability of mechanical loading to enhance tissue-engineered bone regeneration in vivo has not yet been evaluated. Clinically, fixation of segmental defects is typically performed using stiff metal plates that shield the defect region from potentially stimulatory loads. By altering fixation stiffness, it may be possible to improve clinical treatments of such challenging cases through functional load transfer.

These alterations in mechanical environment may also modulate neovascular network formation, which is critical in bone development, growth, and repair. While endothelial cells and individual blood vessels respond and remodel to various stress and strain profiles [3], the influence of matrix deformations on vascular network growth and remodeling in the context of bone repair is not well-known. The overall objective of this work was to investigate the role of mechanical stimuli in vascularized bone regeneration using customized implant systems designed to allow in vivo actuation. The governing hypothesis was that in vivo mechanical loading can enhance bone regeneration and vascular growth in large bone defects treated with sustained delivery of rhBMP-2.

This hypothesis was evaluated in the following specific aims:

SPECIFIC AIM I

Determine the dose- and delivery system-dependence of rhBMP-2 in a critically-sized segmental defect model. Delivery of recombinant human bone morphogenetic protein-2 (rhBMP-2) using a hybrid alginate-based delivery system has been shown in our lab to induce robust bone formation [14]. This aim evaluated the dose response of rhBMP-2 in this nanofiber mesh/alginate delivery system and compared with the current

clinically-used collagen sponge to establish a baseline model upon which to test the effects of mechanical stimulation. We *hypothesized* that the relationship between protein dose and regenerative efficacy depends on delivery system.

SPECIFIC AIM II

Evaluate the effects of in vivo mechanical loading on large bone defect regeneration. It is well-known that mechanical factors acutely influence the fracture healing process; however, the effects of mechanical loading on large bone defect regeneration have not been evaluated. For defects in load-bearing bones, the mechanical environment may be varied by altering the stiffness of the fixation plate, allowing transfer of ambulatory loads to the regenerating bone. This aim, therefore, compared the effects of continuous stiff fixation with electively-actuated compliant fixation that allowed load transfer beginning at week 4. We *hypothesized* that mechanical loading through compliant fixation enhances bone defect healing.

SPECIFIC AIM III

Evaluate the effects of in vivo mechanical loading on neovascular growth. The formation of new blood vessels is essential to provide oxygen and nutrients to regenerating tissues and is a primary limiting factor for many tissue engineering strategies [15-16]. In bone defect healing, vascular supply may be regulated by the mechanical environment. In this aim we evaluated the effects of early and delayed loading on neovascular network formation, in comparison with continuous stiff fixation. We *hypothesized* that early mechanical loading inhibits, while delayed loading enhances, growth of new blood vessels into the defect.

These aims were evaluated using the critically-sized rat segmental defect model developed in our laboratory. In this procedure, a bone segment is surgically removed from the rat femur and the remaining fragments are stabilized by a fixation plate which spans the defect. Using this model, numerous cellular, biomaterial, biomolecular, and biomechanical therapies can be directly and quantitatively compared.

SIGNIFICANCE

This thesis presents the dose-response and delivery system dependence of rhBMP-2 delivery in a hybrid alginate-based protein delivery system for bone regeneration and demonstrates for the first time that proper application of in vivo mechanical loading enhances large bone defect repair by altering bone formation, distribution, and tissue differentiation and also regulates vascular growth and remodeling to modulate the regenerative response. These observations highlight the importance of biomaterial carrier properties in the delivery of recombinant proteins, the influence of the biomechanical environment on regeneration, and the sensitivity of neovascular network formation and subsequent bone formation to the magnitude and timing of load application. Together, these experiments aim to elucidate the mechanoregulatory principles that influence the success of a tissue-engineering approach to vascularized bone regeneration.

CHAPTER II: LITERATURE REVIEW

BONE STRUCTURE AND FUNCTION

Bone serves a number of purposes in human physiology including: (1) a repository for calcium, a fundamental element necessary for cellular signaling and survival, (2) a vessel for stem cell-rich bone marrow, and (3) a structural framework for protecting internal organs and bearing mechanical loads. It adapts dynamically by a coordinated network of unique cell types to respond to both metabolic and mechanical demands. This tightly regulated turnover allows bone to actively respond to a deficit or surplus in soluble calcium and phosphate levels and gives bone a remarkable plasticity in response to its mechanical environment. Together, these cells and coordinated regulatory mechanisms link structure-function relationships across multiple hierarchical length scales.

Cortical and Trabecular Bone

At a whole bone level, human bone is divided into two compartments: cortical, or compact bone, and trabecular, or spongy bone. Cortical bone is characterized by a dense matrix with a relatively low porosity of approximately 10% and makes up 80% of total bone mass [17]. In contrast, trabecular bone is made up of numerous interconnected rod- and plate-shaped struts which give it a sponge-like appearance and a porosity ranging from 50 to 90% [17]. As a result of its low porosity, human cortical bone requires a sophisticated microstructure, called the Haversian system, that allows for vascular perfusion and waste and nutrient transport as well as a complex network of micro-tunnels, termed the lacunar-canalicular network, that provides for cross-talk between

matrix-embedded and surface-dwelling cells and facilitates transduction of mechanical stimuli into biochemical signals which effect cellular activation.

Bone Cells

There are three main cell types that regulate bone formation and remodeling. The first is the osteoblast, which is responsible for laying down new matrix, called osteoid. Osteoblasts are fibroblast-like cells which reside on bone surfaces and are derived primarily from the mesenchymal lineage, being replenished by osteogenic differentiation of bone marrow stromal cells (also known as mesenchymal stem cells) [18]. Additional osteoprogenitor sources such as satellite cells from the surrounding soft tissues or vasculature have also been proposed [19-22]. The second bone cell type is the osteoclast. Osteoclasts are large multinucleated cells, formed from fusion of cells from the monocyte/macrophage lineage, and are responsible for bone matrix resorption through excretion of H^+ ions through V-type ATPase proton pumps and Na/H antiporters [18]. Osteoblasts and osteoclasts communicate and regulate bone turnover through feedback mechanisms involving receptor activator of NFκB ligand (RANKL) and osteoprotegerin (OPG), which regulate osteoclast activity and osteoblast activation[18]. The third cell type is the osteocyte. Osteocytes are the most abundant cell type in bone, and are derived from differentiation of matrix-embedded osteoblasts [18]. Mature osteocytes are stellate shaped and feature large numbers of cytoplasmic processes that allow interactions between neighboring osteocytes through gap junctions [23]. Osteocytes reside within the bone matrix in small pockets called lacunae. These lacunae are connected to one another via canaliculi that allow cross-talk between osteocytes and communication with both osteoblasts and osteoclasts [24]. Osteocytes have been implicated as the master control

cells in bone which regulate matrix deposition and resorption by osteoblasts and osteoclasts, respectively [25-27].

Bone Matrix

On a nanostructural level, bone is made up of both mineral and organic phases, and unlike most other tissues, the matrix is primarily comprised of inorganic mineral (70-90%), which consists of hydroxyapatite, a calcium phosphate apatite whose molecular composition is: $Ca_{10}(PO_4)_6(OH)_2$ [28-29]. These mineral deposits are situated along or between the proteins of the organic phase [28]. Approximately 95% of the organic phase of bone matrix is type I collagen, with the remainder comprised of proteoglycans such as decorin and biglycan and other non-collagenous proteins including glycoproteins such as osteopontin, fibronectin, and bone sialoprotein [18]. Many of these proteins feature both structural and functional roles, modulating tissue properties as well as cellular adhesion, migration, proliferation, and differentiation [28]. Osteopontin, for example, is a phosphorylated glycoprotein expressed by all of the various bone cell types, and is implicated as an important signaling molecule in the early stages of osteogenesis by modulating adhesion of osteoblasts to the extracellular matrix as well as in osteoclast attachment and function [18, 30].

BONE DEVELOPMENT

During development, the long bones, such as those in the extremities, form through a process termed endochondral ossification, in which bone formation occurs via a cartilage template, which is subsequently vascularized and then remodeled by osteoclasts/chondroclasts and replaced with bone by osteoblasts. In endochondral bone formation, the processes of chondrogenesis, osteogenesis and angiogenesis are linked at

the molecular, cellular, and tissue levels, and disruption of any one results in altered limb formation and defects in the other two processes [5]. For example, many of the genes and signaling molecules important for the genesis of cartilage, bone, and vasculature, such as Indian Hedgehog (Ihh), Runx2, and VEGF, respectively, are shared such that knock-out animals lacking any of these three genes experience defects in each of the three tissues [5].

Flat bones, conversely, such as those of the skull, form through intramembranous or direct bone formation, in which mesenchymal cells differentiate directly down an osteoblastic lineage and bone is appositionally laid down without the use of a cartilage scaffold [31]. In both processes, newly formed woven bone is progressively remodeled to mature, lamellar bone. Woven bone is characterized by disorganized, randomly-oriented collagen fibrils, while in lamellar bone, the collagen is highly organized into parallel arrays that alternate in longitudinal and transverse patterns, giving bone its orthotropic material symmetry [31].

BONE REMODELING

Bone has a remarkable ability to adapt to its functional environment, such that its material properties and geometric features are continuously optimized to withstand applied loads [32]. For example, peripheral quantitative computed tomography (pQCT) scans of humerae of elite tennis players indicated a significant 26% increase in cortical cross sectional area in the humerus of the playing arm over the contralateral limb [33-35]. The mechanisms by which this regenerative and adaptive process occurs have only recently begun to be elucidated. The cellular players responsible for bone tissue remodeling were first systematically described in the early 1960's by Frost, who

demonstrated that modeling and remodeling are mediated by basic multicellular units (BMU), made up of osteoblasts, osteoclasts, and osteocytes [36-39]. Osteoblasts lay down bone matrix and osteoclasts degrade it within a highly regulated and interconnected milieu of biochemical signals. Osteocytes, residing within bone matrix and communicating with other cells through the lacunocanalicular network, are thought to be the primary mechanosensors that transduce mechanical stimuli into chemical signals [32, 40]. The adaptive activity of these BMUs is stimulated by changes in the mechanical loading history. Frost hypothesized that this mechanical mediation of bone remodeling was regulated by an inherent "mechanostat" such that there is a window of strain stimuli that maintains bone mass, below which the tissue is resorbed, and above which induces bone formation [41]. Frost hypothesized that the set-points for bone resorption and bone formation are approximately 100-300 microstrain and 1500-3000 microstrain, respectively [41].

Turner and others have since studied numerous mechanical variables affecting bone adaptation [42-46], and have proposed three rules for load-induced adaptation [47]. First, bone adapts to dynamic, but not static strains. Experimental observations revealed that the strain stimulus, or the strain needed to induce adaptation, was proportional to both strain magnitude and frequency:

$$E = k_1 \varepsilon f \quad , \qquad \text{Eqn. 2.1}$$

where E is the strain stimulus, k is a proportionality constant, ε is the peak-to-peak strain magnitude, and f is the loading frequency [46]. Second is the principal of diminishing returns, that is, as loading duration is increased, the bone formation response tends to level off. This effect was mathematically described by Carter and colleagues as:

$$S = k_2 \left[\sum_{j=1}^{n} N_j \sigma_j^m \right]^{1/m}, \qquad \text{Eqn. 2.2}$$

where k_2 is a constant, N is the number of loading cycles per day, σ is the effective stress, and m is a constant weighting-factor, which has been estimated at 3.5-4, based on published data [47-48]. Finally, bone adaptation is error-driven such that bone cells accommodate to "normal" strain waveforms, but adapt to abnormal strain changes [49]. This has been described mathematically as:

$$\frac{\partial M}{\partial t} = B(\varphi - F), \qquad \text{Eqn. 2.3}$$

where M is bone mass, t is time, φ is the local stress/strain state, and B and F are constants that describe the "normal" load state [50]. Thus, φ – F represents the error function driving bone mass adaptation.

These rules apply to both mechanical stimulation of new bone formation, and disuse-induced bone resorption. Astronauts, for example, experience significant reductions in bone mass: when the local stress/strain state, φ, becomes less than the normal earth-bound state, F, because of reduced gravitational loads, the negative error function drives bone resorption [51]. This tightly-regulated system can also become pathogenic in osteoporosis, in which the communication between constituents of the BMU is disrupted, and more bone is resorbed than can be replaced, leading to decreased bone mass and skeletal fragility.

BONE MECHANOTRANSDUCTION

The study of the cellular mechanisms underlying these adaptive phenomena is an active area of investigation. Initially, osteocytes were thought to be biologically quiescent; however, their abundance, distribution and extensive interconnectedness

through gap junctions uniquely situates osteocytes to act as mechanosensors [40]. These cells may therefore act as amplifiers that take in a variety of mechanical stimuli and signals to coordinate a tissue-level adaptive response. The intercellular process of converting mechanical stimuli into biochemical signals resulting in coordinated adaptation is termed mechanotransduction. Duncan and Turner described this process in terms of four distinct steps: (1) mechanocoupling, (2) biochemical coupling, (3) signal transmission, and (4) effector cell response [52].

The first step of mechanotransduction, mechanocoupling, involves the transmission of forces/deformations from the surrounding bone matrix to the cell. Several mechanisms of mechanocoupling have been proposed, and it is likely that all of them act in concert to result in the biochemical, cellular, and tissue-level changes associated with bone adaptation. Perhaps the most direct possibility is matrix-associated mechanical strain of an osteocyte. In vivo, bone matrix strains reach up to approximately 0.3%; however, in vitro studies of the effects of mechanical stretch on bone cells and cell lines have found that variable gene expression is not activated until approximately 3% cell strain, a full order of magnitude larger than that found in vivo [24, 53-54]. This suggests that other amplification mechanisms may play a role in mechanocoupling. Possibilities include shear forces caused by fluid flow through canaliculi [55], intramedullary pressure [56], transient pressure waves [57], and dynamic electric fields, known as streaming potentials [24, 32, 40]. Overall, the various effects of lacunar-canalicular fluid flow have been suggested to be the most probable mechanism of mechanocoupling [55, 57-62]. Recently, Price et al. demonstrated experimentally that bone loading significantly increases solute transport and fluid flow in the lacunar-canalicular system (LCS) under a

loading regime known to induce large scale bone adaptation [55]. This load-induced fluid flow also induces streaming potentials caused by the convective transport of charged solutes present in LCS fluid [56, 58]. Other amplification mechanisms have been proposed as well. For example, Han and colleagues have suggested that the large flexural rigidity of the osteocyte cell processes result in strain amplification [63]. Which mechanism is most important is difficult to determine as it is challenging to experimentally isolate these various effects, and it is likely that they combine in vivo to yield the observed results.

The second step in the mechanotransduction process is biochemical coupling. In this stage, the various mechanical stimuli experienced by a cell are converted to biochemical signals. Numerous signaling pathways have been shown to be activated by mechanical loads, initiated through coupling factors at the cell membrane. Proposed mechanisms include force transfer through integrins and/or focal adhesions and the cytoskeleton, stretch-activated ion/cation channels in the cell membrane, deformation of extracellular flagella known as primary cilia, and membrane structure alterations due to lipid raft and calveoli reorganization [32].

For example, blocking of G protein-coupled receptors has been shown to eliminate up to 80% of prostaglandin production in osteocytes under fluid shear [64]. Also implicated in this pathway are stretch-activated cation channels in the cell membrane, particularly those involving calcium signaling [65-68]. Recently, Guo and colleagues demonstrated the importance of T-type voltage-activated calcium channels in regulating the kinetics of calcium influx in osteocytes following exposure to fluid shear stress [69]. Mechanical stimuli have also been shown to recruit integrins to focal

adhesions in numerous cell types, including both osteoblasts and osteoclasts, resulting in reorganization of actin filaments into stress fibers and activation of focal adhesion kinase [64, 70-71]. Bone cells also possess solitary (primary) cilia that deflect in response to fluid flow and which mediate upregulation of various osteogenic signals including prostaglandin and osteopontin [72-73]. Other membrane structure alterations involving the small lipid rafts known as calveolae have been shown to activate intracellular signaling cascades in response to cell deformation [74-76]. Together, these coupling mechanisms link external loads to internal biochemical signals, though many questions remain.

The third step in mechanotransduction is signal transmission, in which intracellular signaling cascades are activated to bring about alterations in gene expression and protein synthesis and activity. Mechanical stimuli activate numerous signaling molecules and cascades, and many of these are shared across various cell types including monocytes, fibroblasts, endothelial cells, chondrocytes, osteocytes, and osteoblasts [32]. These pathways include the canonical Wnt pathway which regulates the degradation and activity of β-catenin, non-canonical Wnt signaling, integrin signaling through FAK and other receptor tyrosine kinases, NO and cGMP/PKG signaling, and various G-protein coupled receptor pathways including the cAMP activation of PKA, PLC processing of PIP_3 into IP_3 and DAG to stimulate intracellular Ca^{2+} signaling and PKC activity as well as the MAPK cascades and PI-3K activation of PKB.

Canonical Wnt signaling through the β-catenin pathway has recently received great interest as a mechanotransduction mechanism [77]. Intracellular β-catenin is normally controlled by binding to a “destruction complex,” containing glycogen synthase

kinase (GSK-3β) [78]. Under mechanical stimulation, cells produce small molecules known as Wnts that bind to the membrane receptor complex of LRP5/6 and Frizzled to phosphorylate GSK-3β, resulting in deactivation of the destruction complex [79-80]. This allows stabilization of intracellular β-catenin, which translocates to the nucleus to initiate gene expression and in osteoblasts, for example, induces bone formation [81-82]. Interestingly, mechanical stimulation of osteocytes has also been demonstrated to activate the β-catenin pathway independently of Wnt signaling through nitric oxide (NO) and phosphatydilinositol-3 kinase (PI3-K) [83]. In vivo, mice deficient in the transmembrane receptor LRP5 fail to adapt to an anabolic ulnar loading regime, demonstrating the importance of the pathway in functional bone adaptation [84].

Similarly, non-canonical, β-catenin-independent Wnt signaling is also sensitive to the mechanical environment through integrin-mediated activation of the GTPase RhoA, a critical mediator of actin stress fiber assembly [85]. Recently, Khatiwala and colleagues demonstrated that RhoA and the Rho-associated protein kinase (ROCK) differentially activate the extracellular related kinase (ERK) to stimulate osteogenic Runx2 gene expression through the MAPK cascade in response to changes in extracellular matrix compliance [86].

Other integrin-mediated signaling cascades have been shown to be upregulated by extracellular mechanical conditions. One such pathway is G protein-coupled receptor activation of cAMP signaling [87]. Osteoblasts have also been shown to undergo extensive cytoskeleton reorganization in response to both cyclic hydraulic pressure and fluid shear stress, resulting in changes in cell stiffness and cyclo-oxygenase (COX2) gene expression and ATP production [88]. This process is dependent on the focal adhesion

protein α-actinin, which is necessary for stress fiber formation and subsequent COX2 production in osteoblasts exposed to fluid shear stress [89].

Other important signaling cascades in mechanotransduction include the PI-3K and protein kinase B (PKB/Akt) axis and phospholipase C (PLC) activation of intracellular calcium release mediated by inositol-3 phosphate (IP3) and diacyl-glycerol (DAG) [90-91]. For example, Yang et al demonstrated that mechanical strain of osteoblasts results in phosphorylation of the receptor tyrosine kinase PDGFRα to stimulate matrix metalloproteinase expression through PI-3K and PLC [90]. This same signaling cascade has also been shown to upregulate ERK1/2 signaling in osteoblasts in a Ca^{++} dependent manner through the L-type voltage-sensitive calcium channels [91]. Further downstream, fluid shear stress-induced Ca^{++} release causes translocation of nuclear factor κB (NFκB) into the nucleus to induce COX2 gene expression [92]. In parallel, ERK1/2 activity causes mitogen activated protein kinase cascades involving p38 and c-Jun related kinase (JNK) [93-94]. These numerous and overlapping signaling cascades converge to provide these cells with remarkable specificity and sensitivity to their mechanical environment.

The final step in mechanotransduction is effector cell response, in which the basic multicellular units communicate to bring about the desired response. These communications occur directly through gap junctions and by diffusion of secreted signals such as NO [32]. The ultimate response of the BMU is dependent not only on the instantaneous mechanical environment, but also the stress/strain history, as cyclic loading is more stimulatory than single or isometric loads and long durations of loading or unloading may shift the mechanostat setpoint [52]. Overall, mechanical and biochemical regulation of bone remodeling have received much attention because of their influence on

the etiology of osteoporosis and other metabolic bone diseases as well as their importance in bone healing and regeneration.

BONE FRACTURE HEALING

Many of the molecular mechanisms and tissue differentiation profiles seen during fetal development have been shown to be recapitulated in bone fracture repair. As in bone development, bone repair can occur through both the endochondral and intramembranous pathways. Endochondral repair features cartilaginous callus formation followed by remodeling and replacement with bone, and occurs in the presence of compressive micromotion. Endochondral fracture repair begins with haematoma formation following injury, which forms a fibrinous clot that serves as a scaffold and a growth factor supply to facilitate cell migration and reparative function [31]. The early stages of fracture healing (within the first 24 hours) are characterized by an inflammatory phase that has been shown to be necessary for proper healing [95]. This is followed by osteoprogenitor cell migration and differentiation to develop the fracture callus over the first week after injury. These cells potentially come from three sources: the periosteum, the surrounding soft tissues, and the marrow space within the bone [96]. The periosteum is commonly considered to be the primary source of osteo/chondroprogenitors [96-98], though the potential of intramuscular implantation of demineralized bone to induce ectopic bone formation [99] and the ability of bone marrow stromal cells to undergo osteogenic and chondrogenic differentiation [100-101] suggest that the surrounding tissues and the endosteal bone marrow also play important roles in the repair process [96]. Upon arrival at the fracture site, these cells differentiate and begin formation of the cartilaginous callus that characterizes endochondral bone formation. This avascular callus formation serves to

stabilize the fracture gap and reduce interfragmentary motion, and allows for growth of vasculature into the callus from the periphery at around 2 weeks after injury [31, 96]. This facilitates rapid woven bone formation, chondrocyte apoptosis, and osteo/chondroclast recruitment to completely replace the cartilage template with disorganized woven bone (Figure 2.1). Finally, in the third week after injury and following, the external callus is resorbed by osteoclasts, the disorganized woven bone is replaced by mature lamellar bone and the marrow is reestablished [96].

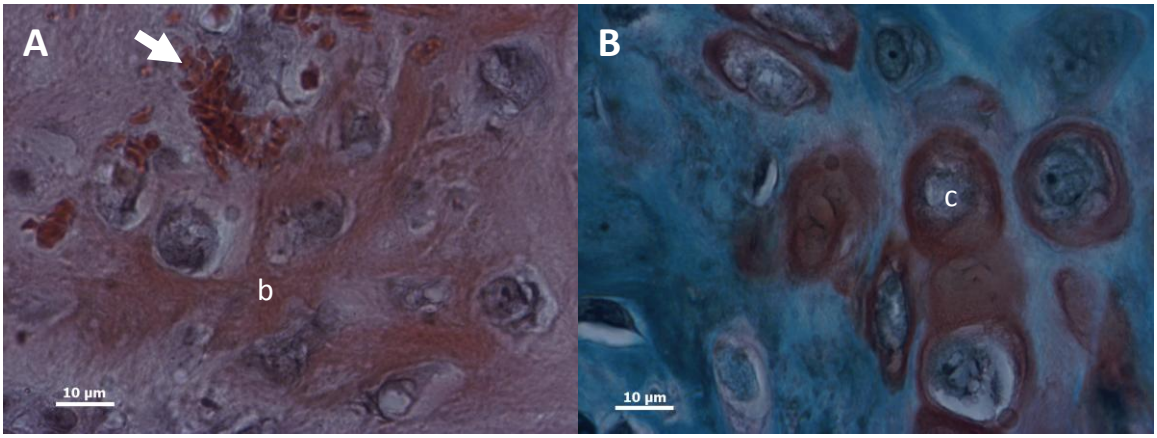

Figure 2.1. Histological images of endochondral ossification during bone repair. (A): Haematoxylin and Eosin-stained section showing hypertrophic chondrocytes, woven bone formation (b) and vascular invasion (arrow indicates erythrocytes). (B): Safranin-O-stained section showing glycosaminoglycan matrix (red) around hypertrophic chondrocytes (c). Images at 63x.

MECHANICAL STIMULATION OF BONE HEALING

Each stage of this process is highly sensitive to mechanical conditions, which have the potential to both accelerate and improve fracture repair as well as induce delayed healing or nonunion [1, 102-126]. The early stages of repair including haematoma formation, cellular recruitment, and initial tissue differentiation have been shown to particularly sensitive to mechanical stimuli [105, 109, 124].

The optimal mechanical environment for rapid and effective fracture healing remains controversial and elusive, though numerous biomechanical factors have been

shown to affect fracture healing, including load magnitude [102-103, 111, 127], timing [105, 113-114, 126], frequency [127-130], cyclic vs. constant application [121], rate [131], and loading mode (i.e. direct shear [112, 118, 120], torsion [112], compression [1, 103-104, 106, 108, 111, 115, 122-123, 125, 132-135], tension [119, 134-138], and bending [102, 125, 139-140]). Other studies have differentiated the effects on healing progression in terms of the stress/strain invariants, that is, the hydrostatic and deviatoric stresses/strains [141-142].

It is now well-accepted that moderate levels of compressive interfragmentary strain are anabolic to callus formation and subsequent healing [1, 115]; however, the effects of tension and shear remain controversial. In distraction osteogenesis, a technique pioneered by Gavril Ilizarov in the 1950's, the bone fragments are distracted at approximately 1mm/day, resulting in osteogenesis and ultimately limb lengthening [134]. In this method, the applied tensile stresses induce primarily intramembranous bone formation [143], though formation of cartilage has been observed in some studies [137, 144]. The Ilizarov technique has been used extensively and successfully in the treatment of limb length disparities, and in the healing of some nonunions and bone defects [145]. In contrast, application of cyclic tensile stains, without progressive lengthening has yielded conflicting results, with some studies showing little to no beneficial effect and others indicating a deleterious effect [119, 135]. The effects of shear are similarly ambiguous, with some studies showing drastic inhibition of healing, to the point of causing nonunion [110, 112, 120, 124] while others have shown positive effects [118]. These differences are likely due to differences in shear strain magnitude, timing, fixation

device, and animal model. Further research is warranted to determine the importance of biomechanical conditions in bone repair.

Several groups have attempted to synthesize these various data into mechanobiological theories that describe the tissue differentiation patterns under different mechanical environments. Pauwels, for example, distinguished between the volume changing effects of hydrostatic stresses and the "distortional" octahedral shear stresses which induce shape change without altering volume [141]. From studying tissue differentiation patterns in pseudarthroses and angulated fractures, he concluded that hydrostatic stresses specifically induce cartilage formation, while the deviatoric stresses, which by necessity feature tension in some direction, cause collagen fiber development [141, 146]. Perren [147] and Perren and Cordey [148], basing their differentiation theory on local strain magnitude, rather than stress invariants, proposed the "interfragmentary strain theory," which states that following fracture, differentiation will occur to produce a tissue which has a higher ultimate strain than the current interfragmentary strain. As tissues grow in and increase the stiffness of the fracture gap, the interfragmentary strain is reduced, allowing further differentiation into a tissue with a lower failure strain and higher modulus. Thus, following fracture, the tissues differentiate from granulation tissue, which features a low stiffness but high ultimate strain, to cartilage, to fibrocartilage, and finally is remodeled to bone, which is characterized by a low ultimate failure strain, but a high modulus of elasticity that limits deformation and confers a high toughness to withstand transient loads [148].

More recently, Carter and colleagues have combined and expanded upon these theories to relate tissue differentiation to mechanical loading conditions and history

[146]. They suggest that tissue differentiation profiles are related to the cyclic load history of both the principal tensile strains and hydrostatic stresses. For example, fibrocartilage differentiation is preferential in regions of high tensile strains with superimposed compressive hydrostatic stress, while bone formation occurs in regions of relatively low tensile strain and low hydrostatic stress [146]. It is important to note that these profiles are also highly dependent on local biochemical signals and oxygen tension. In an adverse biological environment, or in hypoxic conditions, for example, bone formation may not occur despite stimulatory mechanical conditions. To date, however, the most desirable stress/strain history for bone repair remains unknown, and must account for the complicated biological events associated with the different stages of bone healing, including haematoma formation, cell proliferation, and vascularization.

While appropriate levels of mechanical stimuli can play a positive role in bone healing, excessive loading or instability may delay or even prevent successful bone union [110, 149]. These considerations are important when designing and implementing fracture fixation devices, and may be equally valuable in the treatment of large bone defects, which like fracture non-unions fail to heal without further intervention.

BONE DEFECTS & CLINICAL NEED

Large bone defects exceeding 3cm in length, caused by high-energy trauma, fracture nonunion, or tumor resection, represent a particularly challenging problem for orthopaedic clinicians [6-7]. It is estimated that more than 500,000 bone grafting procedures are performed annually in the US and 2.2 million worldwide [150]. These represent an annual cost of $2.5 billion per year in the US alone [150]. The clinical gold standard of care is implantation of morselized autograft bone, taken from the patient's

iliac crest; however, this treatment is restricted by lack of mechanical integrity, significant donor site morbidity and limited graft availability [8-9]. To overcome these limitations, structural bone allografts are often used clinically to bridge the defects; however, a high complication rate is directly attributable to their limited ability to revascularize and remodel [10, 151-154]. Another concern with allograft treatment is risk of disease transmission, which, despite rigorous sterilization efforts, has been reported as recently as 2002 [155-156]. Together, these limitations have stimulated great interest in the development of bone graft substitutes, and tissue engineering has emerged as a promising alternative. In recent years, several tissue engineering strategies have been approved by the US Food and Drug Administration (FDA) for clinical application including various biomaterial scaffolds and several growth factors [157-158].

BONE TISSUE ENGINEERING

A tissue engineering approach which shows particular promise involves recapitulating or stimulating endogenous repair mechanisms to capture the body's innate capacity for self-renewal. The repair of challenging large bone defects is an attractive application of this strategy as bone tissue, unlike most soft tissue injuries, possesses an intrinsic capacity for scar-free regeneration, given proper mechanical and biochemical conditions.

Biologics

One such strategy is the delivery of osteogenic or angiogenic biologics. These can be small molecules, genes, proteins, stem cells, or terminally-differentiated cells. Small molecules are attractive as many may be synthetically synthesized in large amounts with high purity at relatively low cost [159-160]. One such example which shows great

promise in bone repair is desferrioxamine (DFO), which acts as a prolyl-hydroxylase inhibitor to stimulate the hypoxia inducible factor-1α (HIF-1α) pathway, an upstream regulator of the potent angiogenic growth factor, vascular endothelial growth factor (VEGF) [159-160]. Another method is delivery of genes which stimulate endogenous cells to differentiate or produce growth factors [161-162]. For patients with depleted numbers or reduced activity of endogenous cells, stem and differentiated cell delivery is a promising strategy [101, 163-164]. While there has been much attention placed on the possibility of inducing stem cells to reconstitute a tissue defect, and many studies have shown a beneficial effect of such treatments, the cells frequently fail to become engrafted in the regenerate tissue [101]. This has led to the idea of using stem cells as programmable factories and delivery vehicles for target proteins. In this approach, the cells are not necessarily expected or desired to integrate into the functional tissue, but rather to provide the factors necessary for endogenous regeneration in a physiologically relevant manner. Finally, a much-studied and clinically successful strategy is the delivery of recombinant growth factor proteins. While dose and delivery requirements must be tailored for various applications and implant sites, this approach is one of the most successful tissue engineering strategies to date [165].

The introduction of osteoinductive agents as a potential strategy for bone regeneration dates back to Marshal Urist's seminal discovery in 1965 of the potential of devitalized, decalcified allografts to induce bone formation in both ectopic and orthotopic sites [99]. Urist and others subsequently extracted and identified the active biological agents, the bone morphogenetic proteins (BMPs), of which there are at least 15 known types, and which belong to the transforming growth factor-β (TGF-β) supergene family

[166-170]. Identification of the genetic sequence of BMP-2 by Wozney and colleagues enabled mass manufacture of highly purified BMP through recombinant gene technology, which has facilitated its use as a clinical therapy [8, 157, 166, 171].

The BMPs are some of the most important growth factors in bone development, post-natal bone formation, and repair [172-174]. BMP-2, 4, and 7 are all known to play critical roles in bone healing through stimulation of mesenchymal cell differentiation down osteogenic pathways [157]. For example, mice deficient in these proteins develop with significant skeletal abnormalities [175]. The BMPs, like all members of the TGFβ supergene family, bind to serine-threonine kinase receptors. BMP signaling occurs through both type I and type II TGFβ receptors [176-178], and are transduced primarily through the Smad signaling pathway [175-176]. However, MAPK pathways have also been implicated in BMP signal transduction [175-176]. Downstream of BMP binding, several transcription factors are activated, the most-studied of which is the Runt-related transcription factor-2 (Runx-2), a master-regulator of osteoblastic differentiation of mesenchymal cells [175, 179-181]. These mechanisms give the BMPs remarkable potential as therapeutic agents. To date, two of the BMPs have been approved by the FDA for use in humans: rhBMP-2 and rhBMP-7, also known as human osteogenic protein-1 (hOP-1) [182].

Despite robust responses to both rhBMP-2 and rhBMP-7 in numerous animal models, results of clinical trials in human patients have not been as impressive, likely as a result of shortcomings in current delivery methods or lack of sufficient numbers of native responding cells [182]. The FDA-approved and commercially available rhBMP-2 product, Infuse®, from Medtronic, consists of a large dose (3.5 to 12 mg) of soluble

protein, injected onto a bovine collagen I sponge prior to implantation [183]. This delivery system yields a bolus dose with fast release kinetics and may result in protein degradation prior to effective interaction with host cells, suggesting that sustained-release delivery systems may improve efficacy in humans [157].

Biomaterials

Numerous biomaterials are under investigation today as bone tissue engineering scaffolds and biologic delivery systems including biodegradable polymers, bioactive ceramics, and permanent or non-resorbable scaffolds. Natural polymers exhibit good cytocompatibility and bioactivity; however, they may be immunogenic, their degradation rates are difficult to modify, and they generally have low mechanical properties. Natural materials used for bone tissue engineering include demineralized bone matrix (DBM), type I collagen [184], fibrin [185], chitosan [186-187], and silk [188-189]. DBM and type I collagen have both been used clinically to treat craniofacial defects and to perform spinal fusions [190-191].

Synthetic polymers have the advantage of being chemically engineered to possess minimal danger of immunogenicity or disease transmission as well as improved control of degradation rate, mechanical strength, porosity, and microarchitecture [192]. García and colleagues have shown improved cell adhesion to synthetic scaffolds through adsorption of extracellular matrix proteins such as fibronectin or presentation of bio-adhesive motifs (i.e. GFOGER) on biomaterial surfaces [193-194]. Poly-α-hydroxy esters such as PLA, PGA, and their co-polymers have received heavy attention due to their common use in clinical practice as suture and fixation implant materials [195-196], though some inflammatory response has been observed due to their bulk resorption

kinetics and acidic degradation products [197]. Poly(ε-caprolactone) (PCL) scaffolds have the advantage of easy manufacture through rapid-prototyping techniques and have been FDA approved for clinical use in the healing of critically-sized cranial defects; however, degradation is very slow and cell adhesion poor [198]. Scaffolds of polyanhydrides and poly(propylene fumarate) have been developed to be conformal filling, that is, they crosslink *in situ* into porous three-dimensional constructs, allowing conformation to complex geometries. These injectable scaffolds must be designed for minimal heat release during solidification to mitigate damage to surrounding or delivered cells [199-200].

A tremendous amount of research has been performed on biocompatible ceramic materials that mimic the mineral phase of bone. Ceramic scaffolds provide an osteoconductive surface and have specifically been shown to encourage absorption of bioactive proteins [201], promote vascular ingrowth [202], and foster osteoblast adhesion, growth, and differentiation [203-204]. This class of scaffold materials offers a range of resorption rates, but they are often characterized by poor fracture toughness and mechanical strength, especially in porous forms, making them ill-suited to load-bearing situations [205]. Clinically, 45S5 Bioglass® is successfully used to treat periodontal disease, as a bone-filler material, and to replace damaged middle ear bones [205-206]. Porous cements made of calcium phosphates such as β-tricalcium phosphate (β-TCP) are often used as bone void fillers and have been used clinically to repair craniofacial defects [207-209]. Although these scaffolds often exhibit monotonic stiffness and strength similar to bone, mechanical properties relevant to cyclic functional loading such as fracture toughness and fatigue resistance are typically unacceptably low due to limited

ability to arrest crack propagation [210]. Hydroxyapatite (HA) is a biocompatible ceramic with similar chemical composition to the mineral phase of bone which is used clinically for craniofacial defect repair, and as a coating for femoral components of hip replacements in humans [210]. Coralline HA, derived from sea coral, has been used clinically in spinal fusions as well as management of fractures of the tibial plateau [211-212]. A recent study comparing the performance of different porous ceramic scaffolds in vivo found that biphasic calcium phosphate and TCP scaffolds showed better osteoconduction than HA scaffolds in a goat spinal fusion model [213].

Ceramic scaffolds feature osteoconductivity and bioactivity but are limited by brittleness, incomplete interconnectivity, slow degradation rates, and relatively low porosity. Conversely, synthetic porous polymer scaffolds typically offer more controllable architecture but, alone or unmodified, typically present a poor interface for cell attachment and mineralized matrix synthesis. Composite scaffold materials may therefore provide the opportunity to combine the best features of ceramics and polymers and achieve better performance than can be provided by single phase scaffolds. A common strategy has been to incorporate ceramic particles into natural or synthetic polymer matrices [198, 214-218]. In addition to potentially improving mechanical properties, composite scaffolds improve bone cell adhesion and accelerate resorption due to an increase in surface area available for hydrolysis.

Optimizing scaffold design for growth factor delivery requires an additional set of design criteria. Important factors include the protein release kinetics, protein binding affinity, released protein bioactivity, capacity for adhesion and migration of endogenous cells, and degradation rate and by-products. Different materials and conformations

provide varying degrees of control of these considerations. For example, Griffith and colleagues have tethered growth factors to biomaterial substrates to regulate spatiotemporal protein presentation to mesenchymal stem cells and hepatocytes [219-221], and Phelps et al. covalently linked PEG hydrogels with VEGF and cell adhesive peptides to enhance vascular network formation in vivo [222]. Others, such as Stayton and Mooney, have focused on modifying the degradation properties of various hydrogels to modulate growth factor delivery [223-224], while Johnson and colleagues instead used biomaterials to modulate the degradation kinetics of the proteins themselves (Johnson et al in press CORR). These inexhaustive examples illustrate the variety and power of the biomaterial delivery approach; however, degradation properties, release kinetics, and other material properties must be designed and tailored for application as well as implant site, and the optimal delivery methods for growth factor-mediate bone regeneration have not yet been determined [165, 225].

This thesis will employ an alginate hydrogel developed by Mooney and colleagues for use as a spatiotemporal BMP-2 delivery vehicle [226-227]. Alginate is a natural polysaccharide derived from brown algae which may be functionalized with adhesive motifs and irradiated to decrease molecular weight and modulate degradation kinetics [224, 227]. This work will use a method developed in our laboratory by Kolambkar et al., in which the growth factor-loaded alginate is injected into the defect after a biodegradable PCL mesh is wrapped around the native bone ends to contain the alginate and guide bone regeneration [228].

Biomechanics

Mechanical stimulation is another emerging strategy for enhancing regeneration in tissue-engineering. In bone fracture healing, it is clear that the mechanical environment acutely influences regeneration, and these principles are now being applied to tissue-engineered bone repair, both in vitro and, in this thesis, in vivo. Bioreactors, which allow culture of cells and constructs in both 2- and 3-dimensional environments, have been developed to investigate the influence of fluid shear stress and mechanical strain in vitro. These systems have been used to demonstrate the sensitivity of bone cells [229-232], intact tissue explants [233-234], and tissue-engineered constructs [11-12, 235-239]. In general, mechanical stimulation enhances osteogenic differentiation and matrix production in osteoblast precursors and mature bone cells, and may enhance cell viability and matrix distribution in tissue-engineered constructs. Duty et al. have confirmed these effects in MSC-seeded scaffolds loaded in vivo in the hydraulic bone chamber model [13]. Together, these data implicate mechanical loading as a potential method for stimulating endogenous repair mechanisms in tissue-engineered bone regeneration. However, the ability of mechanical loading to enhance large bone defect regeneration has not yet been evaluated.

BLOOD VESSELS & ANGIOGENESIS

Structure and Function

A key component of bone formation, remodeling, and repair is the ability to develop and maintain sufficient vascular supply. Blood vessels carry oxygen, nutrients, growth factors, and circulating cells, and due to the low diffusivity of the dense bone matrix, proximity to capillaries is essential for bone viability and regeneration [15].

Arterial vessels consist of three layers, the intima, the media, and the adventitia. The intima is the innermost layer of the arterial wall, and features a continuous layer of endothelial cells that line the vessels [240]. The next layer, the media, is a "porous heterogeneous medium" which contains an extracellular matrix phase of collagen and elastin fibers embedded with smooth muscle cells, and is responsible for the distensibility of the vessels [240]. The final layer, the adventitia, connects the vessel to the surrounding matrix and consists of primarily fibrous connective tissue and a sparse distribution of fibroblastic cells [240]. This structure provides the vessels with elasticity to physiologic demands as well as the ability to grow and develop new networks in response to regenerative signals.

Angiogenesis, Vasculogenesis, Arteriogenesis.

In the developing embryo, blood vessels form through a process called vasculogenesis, in which the endothelial precursor angioblasts differentiate into endothelial cells, which then assemble in situ to form connected networks [241]. Postnatal vascular growth, however, occurs primarily through two mechanisms: arteriogenesis and angiogenesis [240]. Arteriogenesis features growth and dilation of existing arterioles by proliferation of endothelial and smooth muscle cells in response to demands for increased blood flow [240]. This mechanism is responsible for collateral vessel formation from pre-existing vessels and is thought to be the most rapid method for re-establishing blood supply in intact tissues [242]. However, arteriogenesis is incapable of establishing perfusion of newly-developed tissues, which requires a process of new blood vessel formation termed angiogenesis. Angiogenesis is defined as the sprouting of new capillaries from existing blood vessels and is triggered by hypoxia, resulting in

upregulation of the hypoxia-inducible factor-1 pathway, an upstream regulator of the potent angiogenic protein, VEGF, and matrix remodeling to allow for sprouting of nascent vessels and/or division of existing vessels [240].

VASCULATURE, BONE AND MECHANICAL LOADING

Bone is a highly vascularized tissue, and angiogenesis is essential to skeletal development [243-245]. Mature bone viability and healing are also fundamentally dependent on the vascular supply [15, 246]. Superior bone healing therefore requires both an optimal mechanical environment and a sufficient blood supply, and indeed, one of the primary limiting factors in successful bone defect healing is achieving sufficient vascular perfusion [15-16].

In long bone fracture healing, fixation stiffness regulates the canonical healing patterns, with interfragmentary motions caused by non-rigid fixation stimulating endochondral ossification and rigid fixation leading to intramembranous ossification [1, 105-106, 116]. Likewise, the timing of vascular ingrowth is also known to alter healing patterns, as early vascularization is associated with intramembranous ossification and delayed ingrowth with endochondral ossification. Interfragmentary strains have been implicated as the driving force behind these tissue differentiation paradigms as a result of the homeostatic cellular response to maintain the capacity of the callus tissues to withstand the applied loads [247]. However, another potential rationale is that large interfragmentary strains disrupt microvessel formation leading to an avascular cartilaginous callus. This stiffening reduces interfragmentary motion, allowing initiation of vascular ingrowth and subsequent endochondral bone formation. Regardless of

pathway, sufficient vascularization is essential for timely healing, and insufficient vascular ingrowth can lead to delayed healing or even atrophic nonunion [159, 248-249].

Several ovine studies have indicated that altering the local mechanical environment results in modified vascular ingrowth and consequent fracture healing, though the window of therapeutic effect remains elusive. Wallace and colleagues found increased cortical and medullary blood flow as a result of decreased fixation stiffness [250], while Claes and co-workers showed decreased vascular ingrowth and increased fibrocartilage for increased interfragmentary strains [117]. Likewise, Lienau and colleagues demonstrated differential vessel formation and angiogenic gene expression in response to decreased fixation stability [149, 251].

While critically-sized segmental bone defect repair may not follow the same canonical patterns found in fracture healing, vascularization may play an even more critical role given the larger size of the defect. Mechanical stimulation remains a potent regulator of angiogenesis which may enhance vascularized bone defect repair by influencing tissue differentiation, vascular network formation, and subsequent mineral deposition. This thesis therefore investigated the ability of mechanical loading to regulate bone formation and vascular growth in tissue-engineered bone defect repair.

CHAPTER III: EFFECTS OF PROTEIN DOSE AND DELIVERY SYSTEM ON BMP-MEDIATED LARGE BONE DEFECT REGENERATION*

ABSTRACT

Delivery of recombinant proteins is a proven therapeutic strategy to promote endogenous repair mechanisms and tissue regeneration. Bone morphogenetic protein-2 (rhBMP-2) has been used to promote spinal fusion and repair of challenging bone defects; however, the current clinically-used carrier, absorbable collagen sponge, requires high doses and has been associated with adverse complications. We evaluated the hypothesis that the relationship between protein dose and regenerative efficacy depends on delivery system. First, we determined the dose-response relationship for rhBMP-2 delivered to 8-mm rat bone defects in a hybrid nanofiber mesh/alginate delivery system at six doses ranging from 0 to 5 μg rhBMP-2. Next, we directly compared the hybrid delivery system to the collagen sponge at 0.1 and 1.0 μg. Finally, we compared the *in vivo* protein release profiles of the two delivery methods. In the hybrid delivery system, bone volume, connectivity and mechanical properties increased in a dose-dependent manner to rhBMP-2. Consistent bridging of the defect was observed for doses of 1.0 μg

---

* This chapter is currently in press for publication in Biomaterials (DOI: 10.1016/j.biomaterials.2011.03.063). Authors: Boerckel JD, Kolambkar YM, Dupont KM, Uhrig BA, Phelps HY, García AJ, Guldberg RE.

and greater. Compared to collagen sponge delivery at the same 1.0 μg dose, the hybrid system yielded greater connectivity by week 4 and 2.5-fold greater bone volume by week 12. These differences may be explained by the significantly greater protein retention in the hybrid system compared to collagen sponge. This study demonstrates a clear dose-dependent effect of rhBMP-2 delivered using a hybrid nanofiber mesh/alginate delivery system. Furthermore, the effective dose was found to vary with delivery system, demonstrating the importance of biomaterial carrier properties in the delivery of recombinant proteins.

INTRODUCTION

Large bone defects associated with high-energy trauma, fracture nonunion, and bone tumor resection present a difficult challenge to orthopaedic surgeons accentuated by the limited effectiveness of current treatment options. The gold standard of care, the autograft, in which bone graft particles are surgically transplanted from the patient's iliac crest, is limited by the available volume of graft material and significant donor site morbidity [9, 252]. Allografts are therefore often used to bridge the defects; however, these frequently fail to revascularize and remodel, resulting in graft fracture or tissue necrosis, requiring debridement and retreatment [10, 152, 253].

Biomaterials-mediated delivery of biologic agents including growth factors, stem cells, and genes has been used to stimulate regeneration of the structure and function of various tissues and has specifically emerged as a promising alternative to bone grafting techniques [254]. Delivery of recombinant proteins is a particularly attractive therapeutic strategy to promote endogenous repair mechanisms and tissue regeneration [254]. For a

given protein, the delivery system may affect regenerative response by modulating protein stability and release kinetics. Langer and Folkman first demonstrated in 1976 the possibility of sustaining protein release via encapsulation in biocompatible polymers [255]. Since then, investigators have explored numerous materials and encapsulation and tethering techniques for tissue regenerative applications. For example, Griffith and colleagues have tethered growth factors to biomaterial substrates to regulate spatiotemporal presentation to mesenchymal stem cells and hepatocytes [219-221], and Phelps et al. covalently linked PEG hydrogels with vascular endothelial growth factor (VEGF) and cell adhesive peptides to enhance vascular network formation *in vivo* [222]. Others, such as Stayton and Mooney, have focused on modifying the degradation properties of various hydrogels to modulate growth factor delivery [223-224]. These inexhaustive examples illustrate the variety and power of the biomaterial delivery approach; however, degradation properties, release kinetics, and other material properties must be designed and tailored for each application [165, 225].

Delivery of recombinant human osteoinductive growth factors is one of the most successful and clinically-applicable bone tissue engineering strategies to date [165]. The principle of bone induction dates back to Marshal Urist's seminal discovery in 1965 of the potential of devitalized, decalcified allografts to induce heterotopic bone formation [99]. Subsequently, Urist, Reddi, and others extracted and identified the active biological agents, the bone morphogenetic proteins (BMPs), which belong to the transforming growth factor-β (TGF-β) supergene family [167, 171, 256-259]. Identification of the genetic sequence of BMP-2 by Wozney and colleagues enabled production of highly purified BMPs through recombinant gene technology, which has facilitated its use as a

clinical therapy [8, 157, 166, 171]. To date, two of the BMPs have been approved by the FDA for use in humans: BMP-2 and BMP-7, also known as human osteogenic protein-1 (hOP-1) [182].

Portending the tissue engineering paradigm in the early 1980's, Reddi and colleagues first isolated and combined these soluble osteoinductive factors with insoluble substrata to induce bone formation [256-257]. This approach has seen continued success and aims to stimulate the endogenous regenerative potential of the host by recapitulating the molecular cascades that lead to bone formation during development [260-261]. However, as animal model and clinical data accumulate, the importance of the biomaterial carrier has become increasingly evident [173, 182], and while hOP-1 and rhBMP-2 have been successfully used in spinal fusion and open tibial fractures [262-266], significant limitations to current delivery systems remain [173]. In current clinical practice, rhBMP-2 is delivered by implanting an absorbable collagen sponge soaked in water-solubilized protein [173]. However, complications associated with rapid protein degradation and diffusion (such as soft tissue inflammation and ectopic bone formation) [267-269], the cost of the high doses required for efficacy [183, 270-273], and concerns over a correlation between extremely high doses of rhBMP-2 and cancer incidence [274] suggest that spatiotemporal delivery strategies may improve the efficacy, efficiency, and safety of recombinant growth factor delivery.

Of particular importance for growth factor delivery vehicles is the release profile of the protein from the scaffold, which must maintain a sufficient concentration to induce the desired response for a long enough time to promote recruitment of endogenous progenitor cells [165]. Development and assessment of such delivery vehicles requires

systematic evaluation of protein dose-response relationships as well as comparison to the current clinical standard for both protein release and function. Such studies will facilitate comparison between different carrier systems, animal models, and associated protein doses.

The goal of this study was therefore to characterize and evaluate the dose-response of rhBMP-2 in a recently described protein delivery system designed to provide controlled spatial and temporal protein delivery [14], to compare this system with the clinically-used collagen sponge, and to explain the differences in response by quantifying the *in vivo* protein release profile of each. We hypothesized that bone regeneration responds in a dose-dependent manner to recombinant rhBMP-2 delivery in the nanofiber mesh/alginate delivery system and that this delivery system enhances bone regeneration over the currently used collagen sponge delivery method due to sustained protein release, thereby reducing the necessary effective dose.

MATERIALS AND METHODS

Surgical Procedure

Bilateral, critically-sized (8 mm) segmental defects were surgically created in femora of 13 week-old SASCO Sprague Dawley rats, as previously described [14, 275-276]. Limbs were stabilized by custom radiolucent fixation plates that allowed *in vivo* monitoring with X-ray and microcomputed tomography (microCT). The experimental design featured 8 groups (Table 1, n = 9-10 per group). In 6 groups, the dose response of bone regeneration to rhBMP-2, when delivered in an alginate hydrogel, was evaluated at 0.0, 0.1, 0.5, 1.0, 2.5, and 5.0 μg rhBMP-2, respectively. In these groups, a nanofiber

mesh tube was fitted over the bone ends, and RGD-functionalized alginate hydrogel [224] containing rhBMP-2 was injected into the defect space, as described previously [14]. In the remaining 2 groups, 0.1 and 1.0 μg soluble rhBMP-2 was adsorbed onto an 8 mm x 5 mm diameter collagen sponge, which was then press-fit into the defect. Post-surgery, animals were given subcutaneous injections of buprenorphine every 8 hours for three days. All procedures were approved by the Georgia Institute of Technology Institutional Animal Care and Use Committee (IACUC, protocol # A08032).

Table 3.1. Groups, analysis methods, and sample sizes.

Groups		Analysis Methods & Sample Sizes				
Dose (μg rhBMP-2)	**Delivery System**	**X-ray**	**MicroCT**	**Mechanical Testing**	**Histology**	**Protein Release**
0.0	**Mesh/Alginate**	10	10	9	1	-
0.1	**Mesh/Alginate**	10	10	9	1	-
0.5	**Mesh/Alginate**	10	10	9	1	-
1.0	**Mesh/Alginate**	9	9	8	1	-
2.5	**Mesh/Alginate**	10	10	9	1	6
5.0	**Mesh/Alginate**	10	10	9	1	-
0.1	**Collagen Sponge**	9	9	8	1	-
1.0	**Collagen Sponge**	10	10	9	1	-
2.5	**Collagen Sponge**	-	-	-	-	6

Nanofiber Mesh Production

Nanofiber meshes were produced as previously described [14]. Briefly, poly-(ε-caprolactone) (PCL) was dissolved at a concentration of 12% (w/v) in a 90:10 volume ratio of hexaflouro-2-propanol:dimethylformamide (Sigma-Aldrich) and electrospun onto a static collector. Twenty-four 1-mm diameter perforations were patterned into the nanofiber mesh sheets, which were then glued into tubes of 4.5 mm diameter and 12 mm

length. Mesh tubes were sterilized by 100% ethanol evaporation, and were stored in sterile phosphate buffered saline (PBS) prior to implantation.

Alginate Gel & Collagen Sponge Growth Factor Loading

Recombinant human BMP-2 (R&D Systems) was reconstituted in 0.1% rat serum albumin in 4 mM HCl, according to manufacturer instructions. For the mesh/alginate delivery groups, the BMP-2 was then mixed at 6 different concentrations with RGD-functionalized alginate [224, 277] to a final concentration of 2% alginate, which was cross-linked by mixing rapidly with 0.84% (m/v) $CaSO_4$. The alginate hydrogel was covalently coupled with G_4RGDASSP peptide sequences at 2 sequences per polymer chain using carbodiimide chemistry. Each defect received 200 µl of the pre-gelled alginate containing 0.0, 0.1, 0.5, 1.0, 2.5, or 5.0 µg rhBMP-2, depending on group. For the collagen sponge delivery groups, rhBMP-2 was pipetted onto the scaffolds 10 minutes prior to implantation at either 2 or 20 µg/ml, for the 0.1 and 1.0 µg groups, respectively.

Faxitron and MicroCT

Digital radiographs (Faxitron MX-20 Digital; Faxitron X-ray Corp.) were taken at 2, 4, 8, and 12 weeks post-surgery with an exposure time of 15 s and a voltage of 25 kV (n=10 per group). Bridging was defined by appearance of continuous bone crossing the defect. Bridging rates were blindly assessed by two independent observers, with differences determined by a third independent arbiter. At weeks 4, 8, and 12 post-surgery, animals were scanned using in vivo microCT (Viva-CT 40; Scanco Medical) at medium resolution and 38.5 µm isometric voxel size, with the scanner set at a voltage of 55 kVp and a current of 109 µA. The volume of interest (VOI) encompassed all bone formation

within the center 120 slices (4.56 mm) between the native bone ends. New bone formation was segmented by application of a global threshold (386 mg hydroxylapatite/cm^3) corresponding to 50% of the native cortical bone density, and a Gaussian filter (sigma = 1.2, support = 1) was used to suppress noise.

Biomechanical Testing

After 12 weeks, animals were euthanized by CO_2 asphyxiation, and femora (n = 8-9 per group) were excised for biomechanical testing in torsion to failure as described previously [275]. Briefly, limbs were cleaned of soft tissues and the ends potted in Wood's metal (Alfa Aesar). The fixation plates were then removed, and limbs were mounted on a Bose ElectroForce system (ELF 3200, Bose EnduraTEC) and tested to failure at a rate of 3º/sec. Maximum torque at failure and torsional stiffness, given by the slope of the line fitted to the linear region of the torque-rotation curve, were computed for each sample.

Histology

One representative sample per group was taken for histology at week 12 post-surgery. Samples were chosen based on microCT-calculated average bone volume at week 8. Samples were fixed in 10% neutral buffered formalin for 48 hours at 4ºC and then transferred to a formic acid-based decalcifier (Cal-ExII, Fisher Scientific) for 2 weeks under mild agitation on a rocker plate. Following paraffin processing, 5 µm-thick mid-saggital sections were cut and stained with Safranin-O/Fast-green [278] and Haematoxylin and Eosin (H&E). Due to the presence of carboxyl groups, alginate carries a negative charge [279], allowing high contrast staining with Safranin-O.

BMP-2 Tracking

A separate study was conducted to compare the protein release and degradation over time in vivo. Segmental defects were created as described above and were treated with 2.5 µg near-infrared (NIR) fluorophore-tagged rhBMP-2, delivered in either collagen sponge or nanofiber mesh/alginate. rhBMP-2 was tagged with an in vivo NIR fluorochrome label (VivoTag-S 750, VisEn Medical) using NHS-ester chemistry. Briefly, rhBMP-2 was reconstituted in 4 mM HCl at a concentration of 100 µg/ml. Due to presence of glycine in the lyophilization buffer, the buffer was exchanged to 100 mM $NaPO_4$ at pH 7.5 by two rounds of filtration through a 3 kDa centrifugal filter (Millipore Amicon Ultra, Millipore). The protein was then labeled by 4 hour incubation with 6 M excess of the fluorophore at room temperature. Excess fluorophore was removed by gel filtration through Zeba Spin Desalting Columns (7K MWCO, Fisher Scientific). Protein tagging was verified by SDS-PAGE. Labeled protein fluorescence was tracked over 21 days in vivo using a 700 series Xenogen IVIS Imaging System. Animals were imaged at 745 nm excitation, 780 nm emission and 60 s exposure time at 0, 3, 7, 14, and 21 days post-surgery. Fluorescence intensity was measured as background-subtracted average efficiency within a fixed region of interest (ROI) centered on the defect site. Values from each sample were normalized to that sample's initial intensity to represent percentage of protein remaining [225, 280]. Nonlinear regression analysis of release profiles were performed on raw data in GraphPad Prism using a one-phase exponential decay model (GraphPad Software, Inc.).

Statistical Analyses

All data are presented as mean ± standard error of the mean (SEM). Differences between groups and among time points were assessed by analysis of variance (ANOVA) with pairwise comparisons made by Tukey's post hoc analysis, Chi-squared analysis with individual comparisons made by Fisher's Exact test, analysis of covariance (ANCOVA) and Student's t-test, where appropriate ($\alpha = 0.05$). A natural log transformation was applied to maintain normality of residuals and homogeneity of variance, when necessary and appropriate. Minitab® 15 (Minitab, Inc.) was used to perform the statistical analysis.

RESULTS: DOSE-DEPENDENCY

First, the dose response of rhBMP-2 in the nanofiber mesh/alginate delivery system was evaluated over 12 weeks in critically-sized rat femoral bone defects.

Faxitron

In vivo digital radiographs (Figure 3.1) qualitatively demonstrated a dose-dependent bone formation response to rhBMP-2, and longitudinal evaluation of bridging rates likewise revealed significant dose-dependency of defect bridging to amount of delivered rhBMP-2 (Table 3.2). Groups with 1.0 µg rhBMP-2 or greater achieved consistent (80-100%) bridging by week 12 post-surgery. Doses less than or equal to 0.5 µg rhBMP-2 failed to bridge consistently, regardless of delivery system.

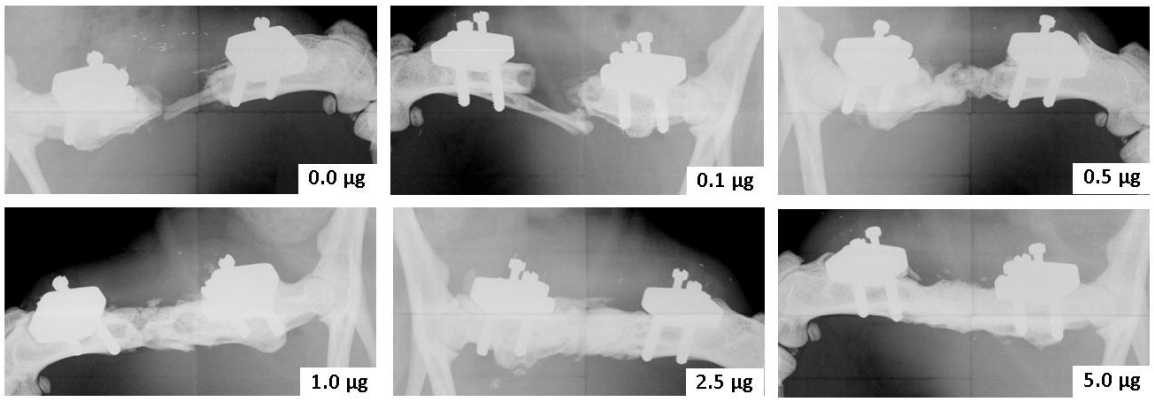

Figure 3.1. Representative digital radiographs of segmental defects treated with 0.0, 0.1, 0.5, 1.0, 2.5, and 5.0 µg rhBMP-2, as indicated, delivered in the nanofiber mesh/alginate delivery system. Images taken at week 12.

Table 3.2. Defect bridging results vs. rhBMP-2 dose delivered in the mesh/alginate system. a: $p < 0.05$ vs. 0.0 µg group, b: $p < 0.05$ vs. 0.1 µg group, c: $p < 0.05$ vs. 0.5 µg group.

Dose	Week 2	Week 4	Week 8	Week 12
0.0 µg	0/10	0/10	1/10	1/10
0.1 µg	0/10	0/10	1/10	3/10
0.5 µg	0/10	0/10	4/10	5/10
1.0 µg	1/9	6/9 [a, b, c]	8/9 [a, b]	9/9 [a, b, c]
2.5 µg	2/10	6/10 [a, b, c]	8/10 [a]	8/10 [a]
5.0 µg	3/10	9/10 [a, b, c]	10/10 [a, b, c]	10/10 [a, b, c]

Microcomputed Tomography

MicroCT scans confirmed the two-dimensional X-ray results. Minimal bone formation occurred at low doses. Beginning at the 0.5 µg dose, however, bone formation was evident at the center of the defects as well as on the surfaces of the nanofiber mesh, where the holes in the newly formed bone corresponded with mesh perforations (Figure 3.2). Local density maps on saggital cross sections demonstrated the distribution and maturity of bone within the defects (Figure 3.2). At doses larger than 1.0 µg, bone formed throughout the defects, with dose-dependent increases in defect filling.

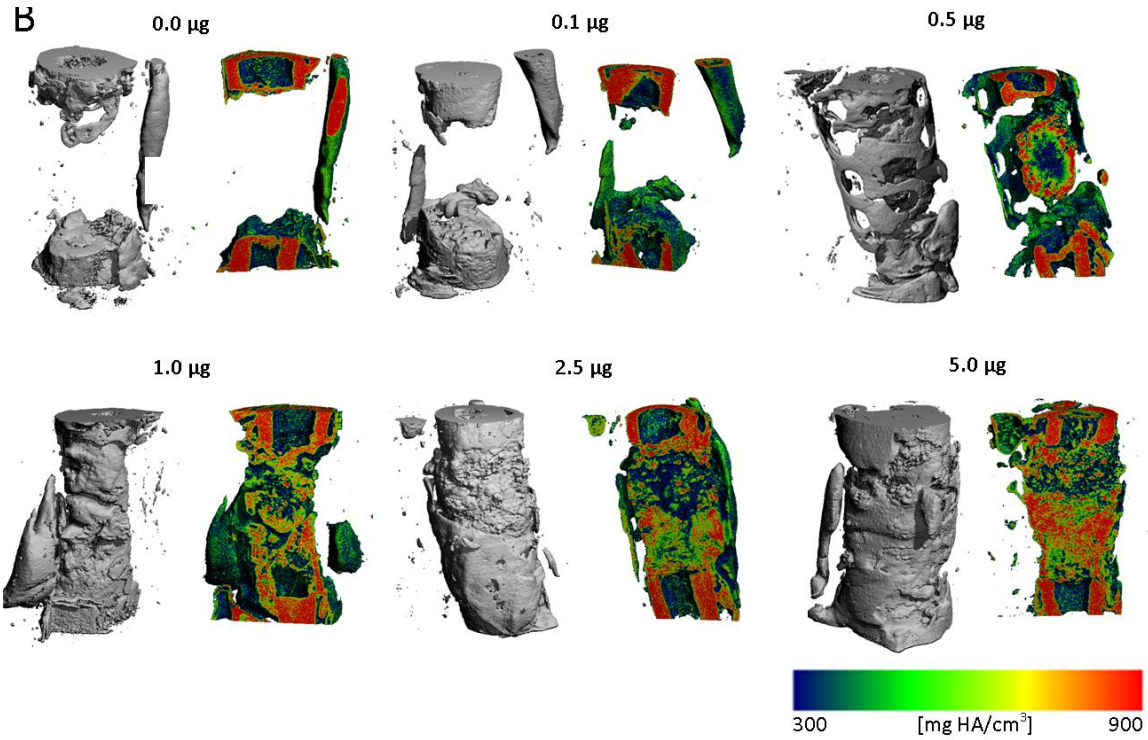

Figure 3.2. MicroCT reconstructions showing 3D structure and saggital cross sections illustrating local mineral density mapping. Segmental defects were treated with 0.0, 0.1, 0.5, 1.0, 2.5, and 5.0 µg rhBMP-2, as indicated, delivered in the nanofiber mesh/alginate delivery system.

MicroCT was used to quantify 3D tissue ingrowth parameters including volume, density, and connectivity of the newly formed bone. In the mesh/alginate groups, bone formation responded in a nonlinear, dose-dependent manner to rhBMP-2. By week 12, the 1.0 and 2.5 µg doses had significantly greater bone volume than 0.0, 0.1, and 0.5 µg doses, and the 5.0 µg dose group exhibited significantly greater bone volume than all other groups (Figure 3.3A). The dose-response curve exhibited linear biphasic behavior, with the slope (m_bv) of the bone volume vs. dose curve decreasing significantly ($p < 0.0001$) at 1.0 µg or greater ($m\_bv_{0.0\text{-}1.0} = 50.1 \pm 4.8$ mm^3/µg and $m\_bv_{1.0\text{-}5.0} = 9.21 \pm 2.8$ mm^3/µg, $R^2 = 0.75$ and 0.30, respectively, at week 12). Connectivity increased with rhBMP-2 dose in a similar manner to bone volume. However, unlike bone volume, the

connectivity of the bone microstructure decreased with time as the initial finely-trabeculated structure was remodeled between 4 and 12 weeks (Figure 3.3B). There were no differences in mean mineral density among the dose groups at any time point, though the density increased with time for all groups (Figure 3.3C).

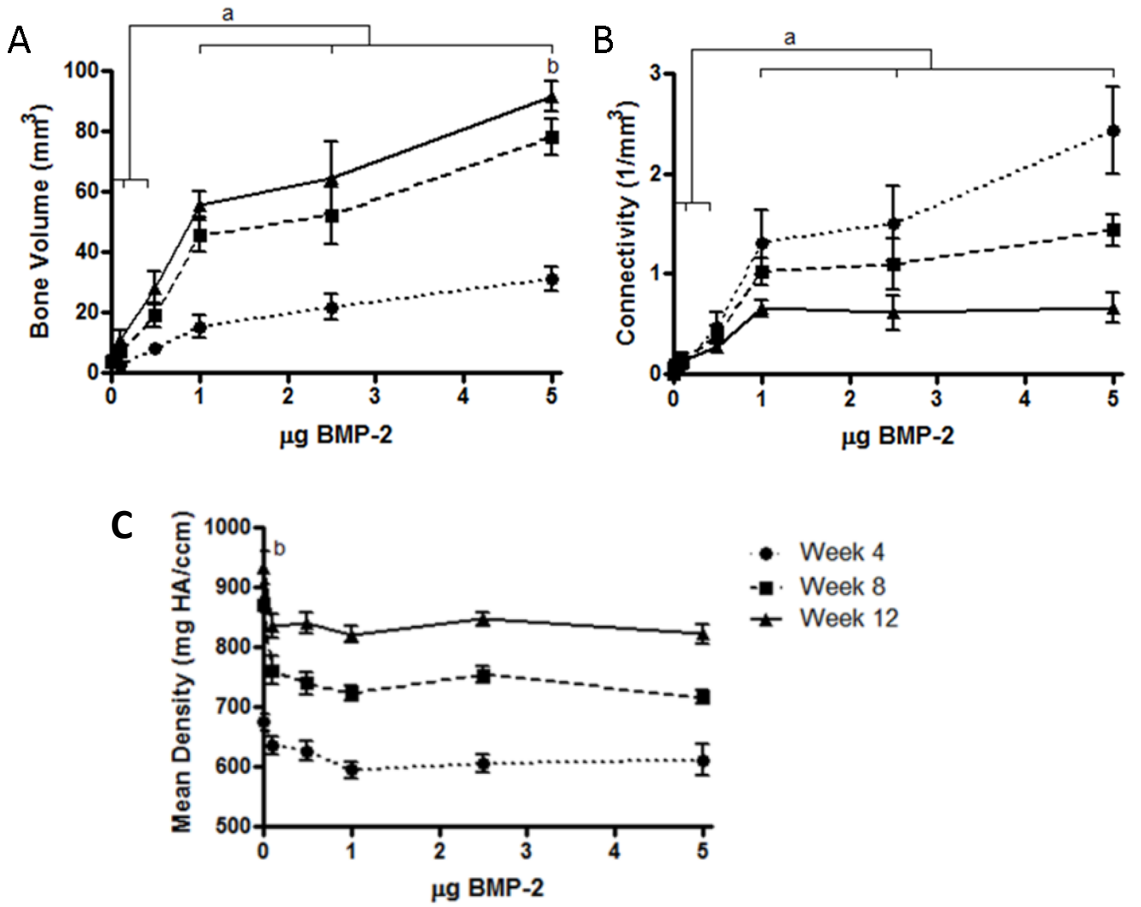

Figure 3.3. MicroCT quantification of bone volume, connectivity, and mean density as a function of rhBMP-2 dose at week 4 (light dashed lines), week 8 (bold dashed lines), and week 12 (solid lines). Bone volume (A) and connectivity (B) demonstrated nonlinear dose-dependent responses to rhBMP-2, with a reduction in response to increased dose above 1.0 µg. No differences between groups were found for mean density (C). a: $p < 0.05$ as indicated, b: $p < 0.05$ vs. all other groups.

Biomechanical Testing

To evaluate the degree of functional restoration, biomechanical testing in torsion to failure was performed on potted femurs. Biomechanical properties increased continuously with increasing dose of rhBMP-2, with the 1.0, 2.5, and 5.0 µg groups having significantly greater torsional stiffness (Figure 3.4A) and maximum torque at failure (Figure 3.4B) than the 0.0, 0.1, and 0.5 µg groups. In contrast to bone volume and

connectivity, which featured a reduction in response to increasing dose at doses greater than 1.0 µg rhBMP-2, mechanical properties exhibited continuously increasing stiffness and torque with increasing protein dose, and the dose-response curves did not significantly change slope over the range of doses evaluated ($p = 0.47$ and $p = 0.65$ for stiffness and torque, respectively).

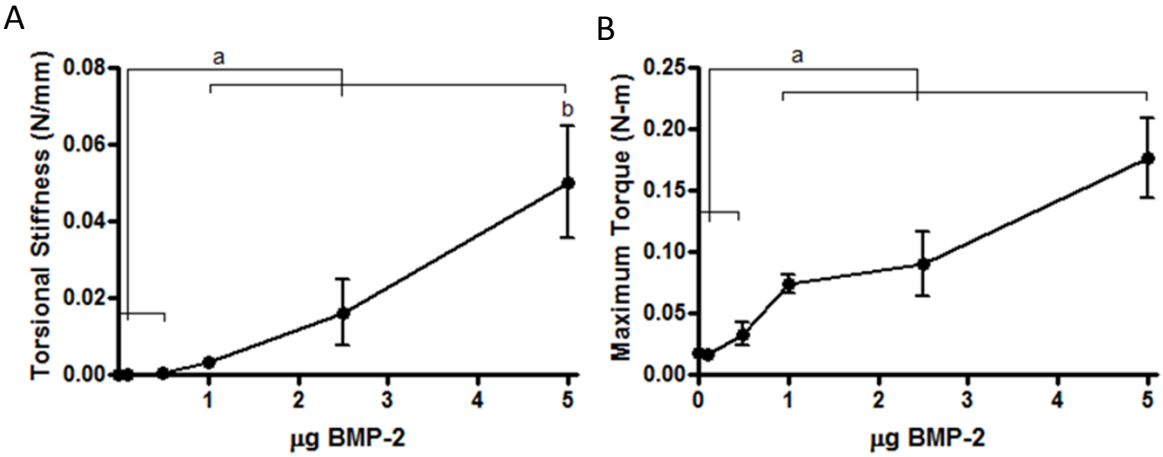

Figure 3.4. Post-mortem biomechanical properties as a function of rhBMP-2 dose. Torsional stiffness (A) and failure torque (B) continuously increased with increasing dose of rhBMP-2. a: $p < 0.05$ as indicated, b: $p < 0.05$ vs. all other groups.

Histology

Histological staining allowed evaluation of tissue morphology, cellular infiltration, and alginate gel degradation at week 12. Haematoxylin and Eosin staining revealed a mixture of osteocyte-populated woven and lamellar bone in groups with bone formation (Figure 3.5A). In the 0.0 µg group, the defect space appeared highly homogeneous and filled with alginate gel. In this group, very few cells had migrated into the defect space, and tissue invasion into the alginate was minimal. In contrast, large numbers of invading cells were present in all other groups, even at very low doses of BMP, though cellular infiltration appeared to increase in a dose-dependent manner. The

degree of fragmentation of the alginate gel was found through Safranin-O/fast green staining to likewise be dose-dependent, featuring negligible dissolution in the 0.0 µg group and increased tissue invasion and alginate fragmentation with increasing amounts of rhBMP-2 (Figure 3.5B). Regardless of protein dose, the gel did not completely degrade by 12 weeks, as indicated by the presence of small regions of alginate embedded in mineralized matrix even at the 5 µg dose.

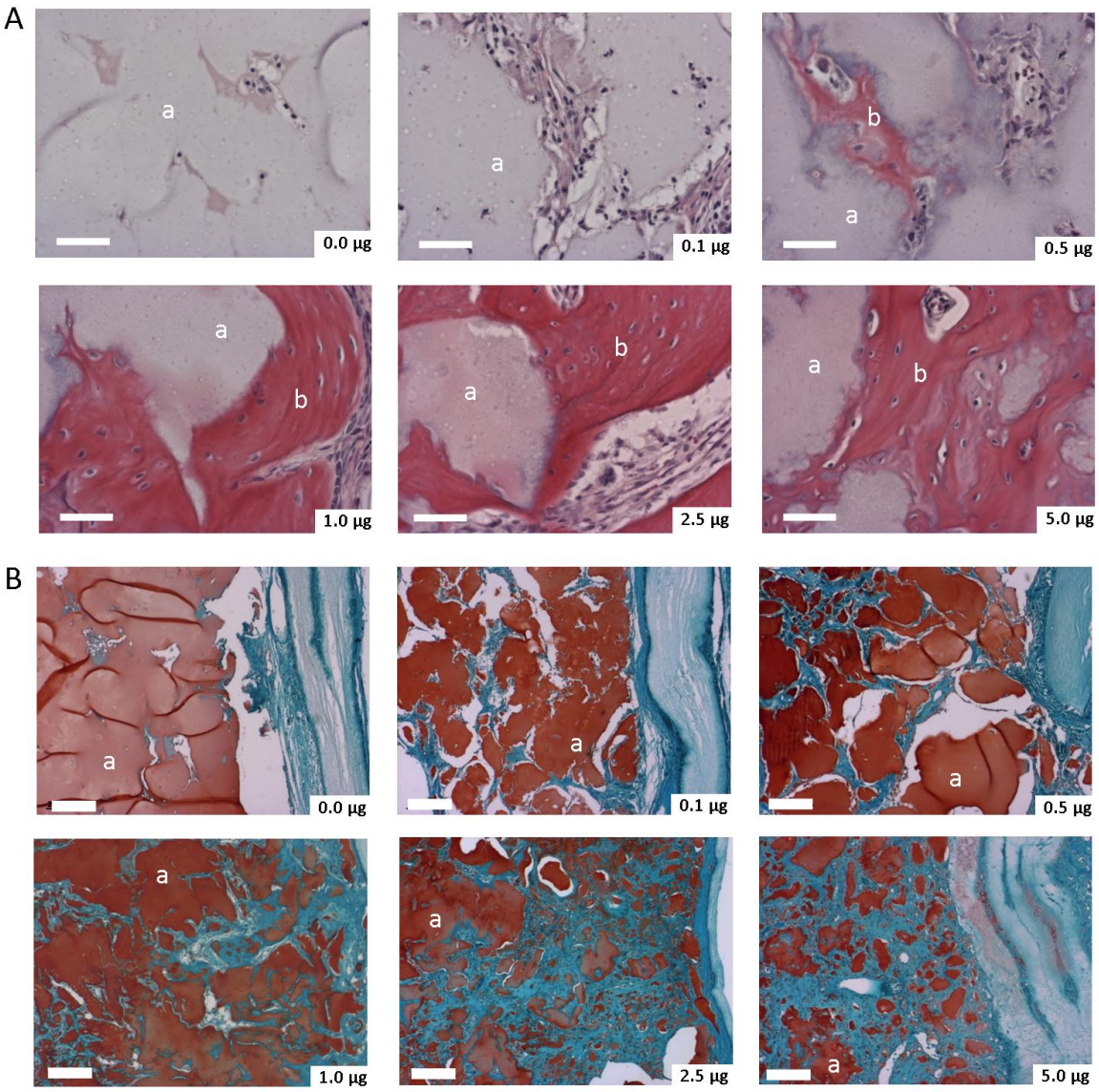

Figure 3.5. Week 12 histological staining of saggital sections at each dose of BMP-2, delivered in the mesh/alginate delivery system. H&E staining (A) illustrated bone formation (white arrow) and cellular invasion. Images at 20x, scale bars: 50 µm. Safranin-O/fast green staining at 4x (B) illustrated dose-dependent increases in alginate gel (black arrow) fragmentation and degradation as well as tissue infiltration (fast green counterstain). Images at 4x, scale bars: 200 µm.

RESULTS: DELIVERY SYSTEM COMPARISON

Next, we compared the nanofiber mesh/alginate delivery system at a non-bridging dose (0.1 µg) and a bridging dose (1.0 µg) with the clinically-used collagen sponge delivery system at the same doses. Finally, we compared the in vivo protein release kinetics of the two delivery methods using fluorophore-tagged rhBMP-2.

Faxitron

In vivo digital radiographs (Figure 3.6) qualitatively demonstrated a delivery system-dependent bone formation response to rhBMP-2. At 1.0 µg rhBMP-2, the mesh/alginate delivery system resulted in 100% defect bridging by week 12, while collagen sponge delivery resulted in 60% bridging, though this difference was not statistically significant with $p = 0.0867$ (Table 3.3). 0.1 µg rhBMP-2 was insufficient to induce robust bone formation in either delivery system.

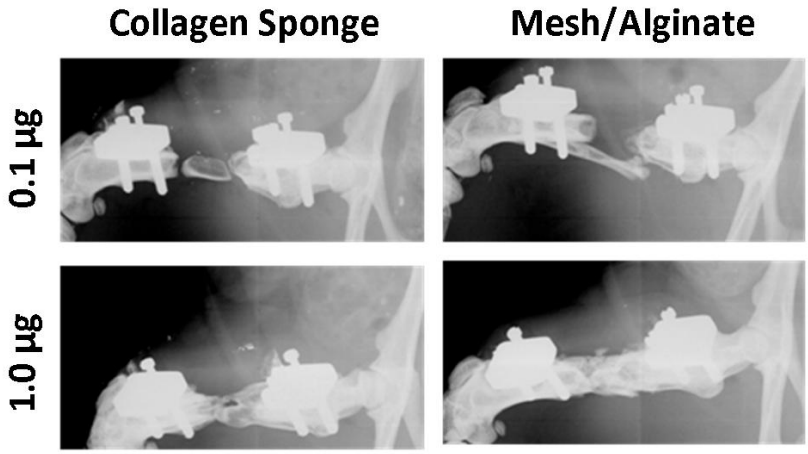

Figure 3.6. Representative digital radiographs of segmental defects treated with 0.1 or 1.0 µg rhBMP-2, delivered in either collagen sponge or in the nanofiber mesh/alginate delivery system.

Table 3.3. Defect bridging results based on delivery system. d: $p < 0.05$ vs. collagen 0.1 µg group.

Group	Week 2	Week 4	Week 8	Week 12
M/A 0.1 µg	0/10	0/10	1/10	3/10
Col 0.1 µg	0/9	0/9	0/9	0/9
M/A 1.0 µg	1/9	6/9	8/9	9/9
Col 1.0 µg	1/10	3/10	4/10	6/10 [d]

Microcomputed Tomography

MicroCT scans again confirmed the two-dimensional X-ray results and clearly illustrated differences in delivery systems at 1.0 µg rhBMP-2 (Figure 3.7). Local density maps on saggital cross sections demonstrated the distribution and maturity of bone within the defects (Figure 3.7). Collagen groups exhibited formation of thin bony shells containing small amounts of trabeculated bone, while the mesh/alginate group featured bone formation throughout the defect at 1.0 µg.

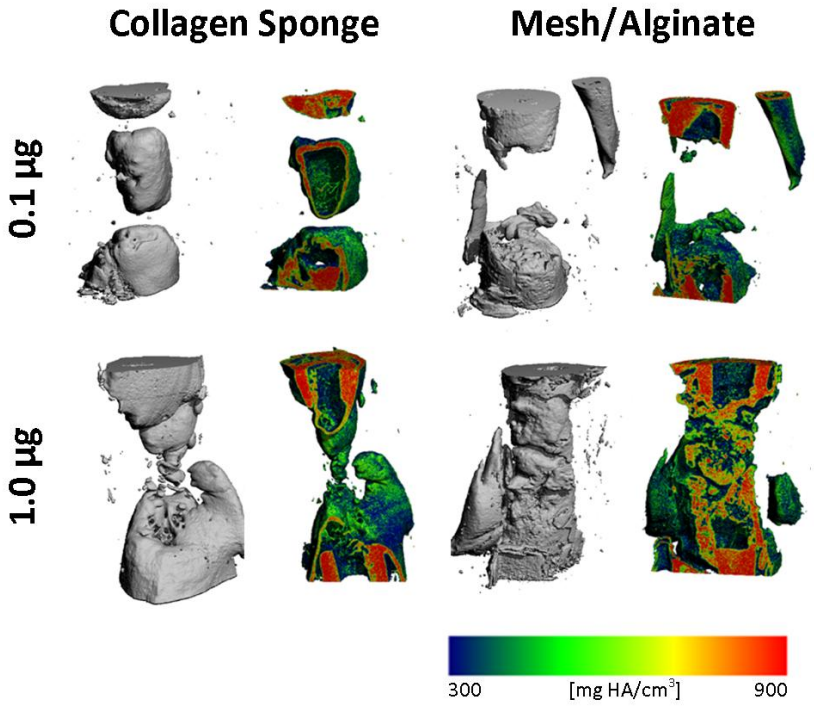

Figure 3.7. MicroCT reconstructions showing 3D structure and saggital cross sections with local mineral density mapping to illustrate bone formation, defect bridging and tissue maturity.

Quantification of microCT images revealed significant differences in bone formation between the collagen sponge and mesh/alginate delivery systems (Figure 3.8A-I). At week 4, there were no differences in bone volume between groups at either 0.1 or 1.0 μg dose (Figure 3.8A). However, by week 8, the bone volume in the mesh/alginate 1.0 μg group was significantly greater than the collagen sponge 1.0 μg group, and this effect widened to 2.5-fold greater by week 12 (Figure 3.8B, C). Temporally, bone volume increased significantly from week 4 to weeks 8 and 12 with mesh/alginate delivery, whereas with collagen sponge delivery, bone formation occurred rapidly over the first 4 weeks but did not increase significantly after week 4. Connectivity was significantly greater in the mesh/alginate 1.0 μg group than the collagen sponge 1.0 μg group at both weeks 4 and 8 (Figure 3.8D, E); however, by week 12, the connectivity had normalized in both groups (Figure 3.8F). As among the mesh/alginate groups, no differences in mean mineral density were found between groups, though the density increased with time in each group (Figure 3.8G-I). No differences in bone formation were found between collagen and mesh/alginate delivery at the low dose of 0.1 μg at any time point for any measure.

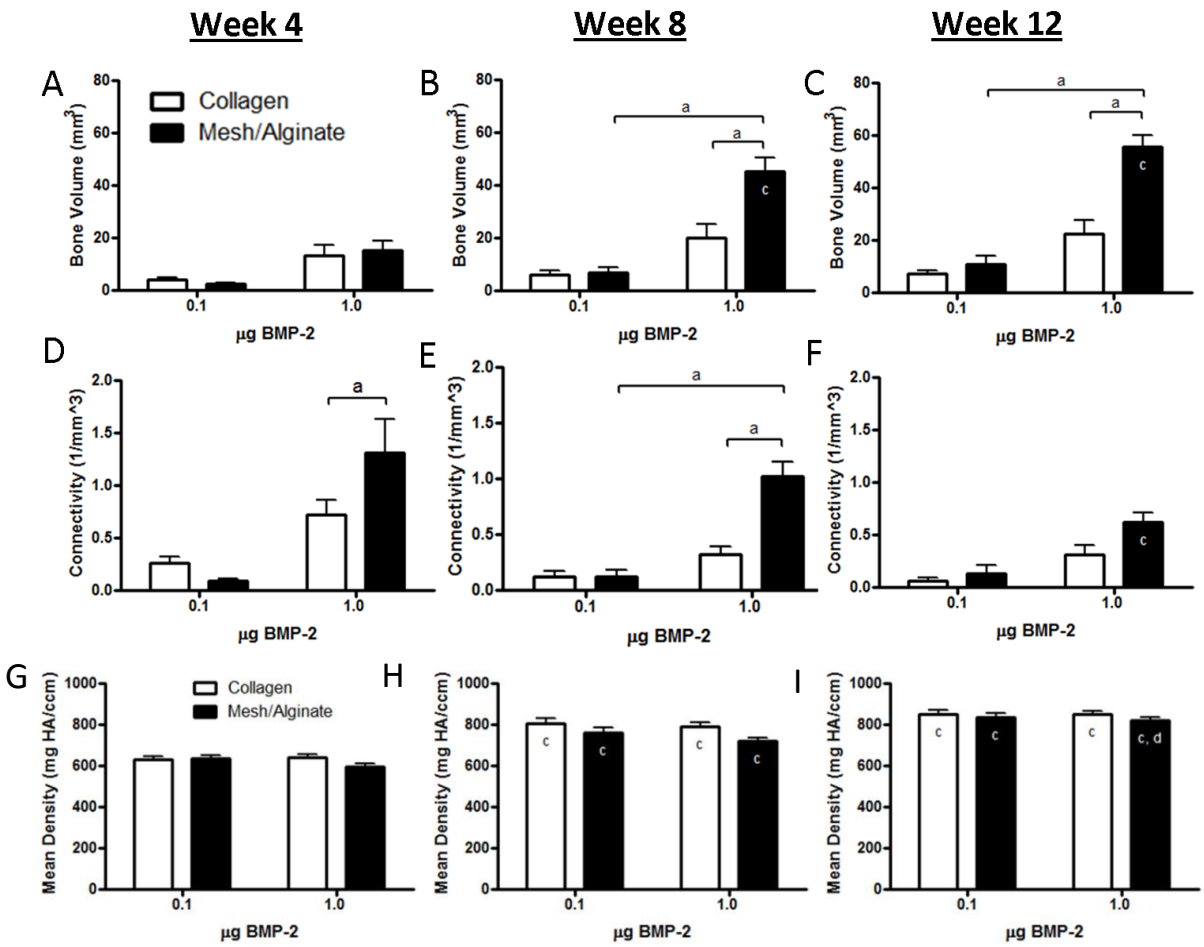

Figure 3.8. MicroCT quantification of bone volume (A-C), connectivity (D-E), and mean density (G-I) at week 4 (A, D, G), week 8 (B, E, H) and week 12 (C, F, I) post-surgery. Dark bars represent mesh/alginate delivery system and light bars represent collagen sponge delivery system. Mesh/alginate delivery yielded an early increase in connectivity (D) and conferred a 2.5-fold greater bone volume by week 12 (C) in comparison to collagen sponge delivery. Mean mineral density was not significantly dose- or delivery system-dependent. a: $p < 0.05$ as indicated, c: $p < 0.05$ vs. week 4, d: $p < 0.05$ vs. week 8.

Biomechanical Testing

Differences in torsional stiffness and maximum torque did not reach significance between collagen and mesh/alginate delivery, $p = 0.057$ and $p = 0.082$, respectively, though dose-dependent differences were apparent as before (Figure 3.9A, B).

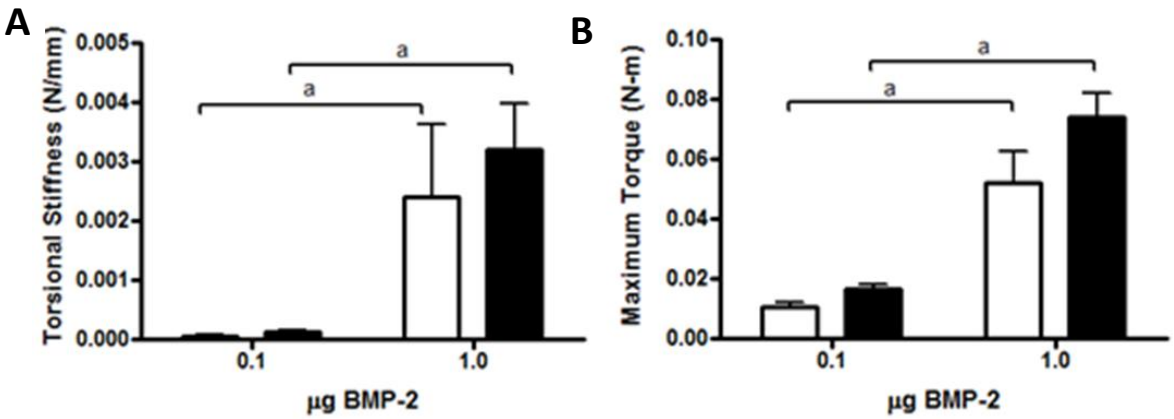

Figure 3.9. Post-mortem biomechanical testing revealed significant dose-dependent increases in stiffness (A) and failure torque (B) but differences between delivery systems did not reach significance at either dose. a: $p < 0.05$ as indicated.

Histology

Histological staining with Safranin-O was performed to compare tissue morphology and composition between delivery systems at week 12 (Figure 3.10). In contrast to the mesh/alginate groups which contained substantial amounts of non-degraded hydrogel through week 12, the collagen sponges had completely resorbed. In the collagen sponge 0.1 µg group, defects were filled primarily with fibrous tissue, while in the collagen sponge 1.0 µg group, the new bone formed thin shells, containing trabeculated bone and marrow.

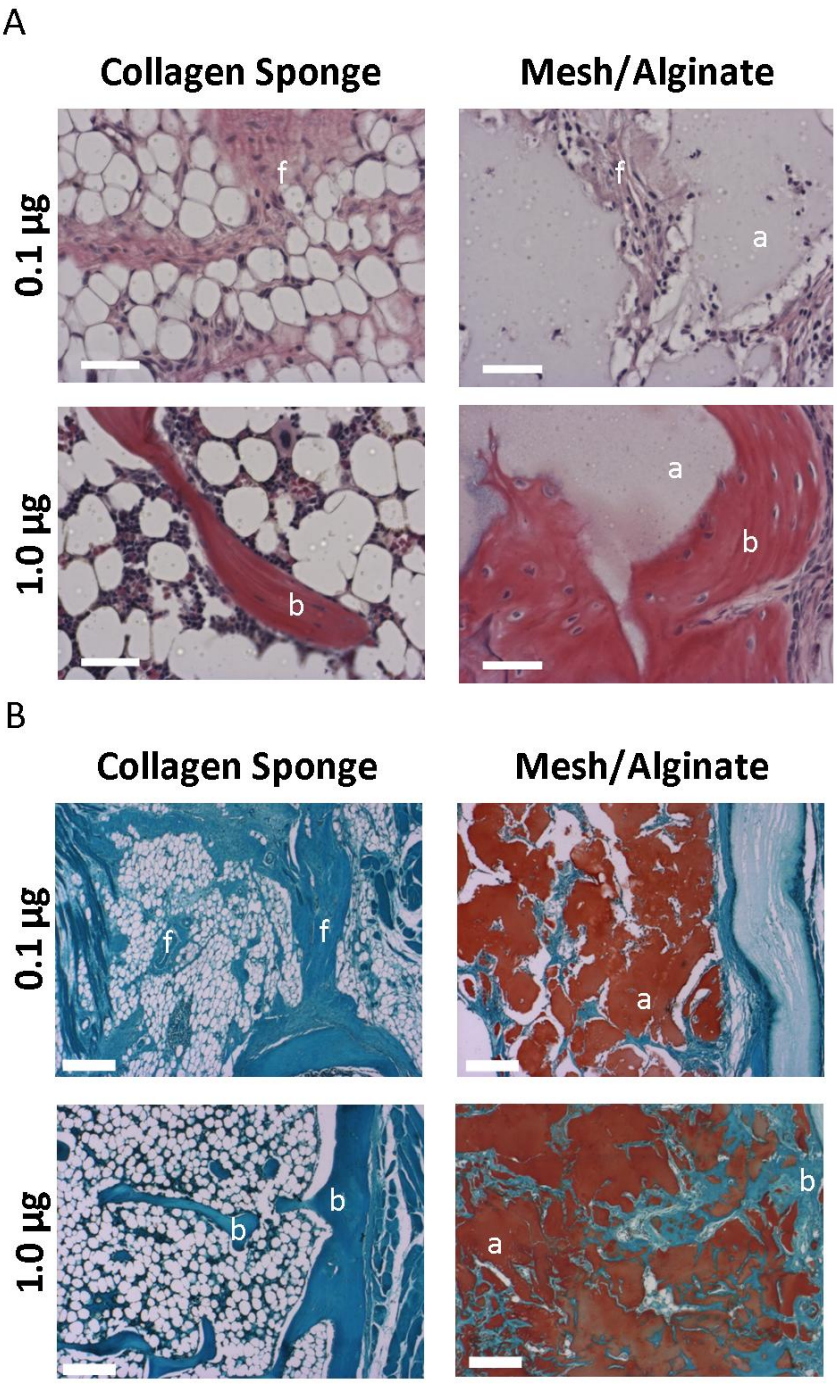

Figure 3.10. Week 12 histological staining of saggital sections. H&E staining (A) illustrated bone (b) and fibrous tissue (f) formation and residual alginate (a). Images at 20x, scale bars: 50 µm. Staining with Safranin-O (B) revealed a significant persistence of alginate gel (a) through week 12 in the mesh/alginate group. Large amounts of fibrous tissue (f) were apparent in the collagen sponge group at 0.1 µg, while at 1.0 µg small amounts of trabecular bone (b) and fatty marrow filled the defect. The collagen sponge had entirely absorbed by week 12 in both collagen sponge groups. Images at 4x, scale bars: 200 µm.

BMP Release

To investigate a possible mechanism for the observed delivery system-dependent increases in bone formation, fluorescently-labeled protein was tracked over 3 weeks (Figure 3.11). For both delivery systems, the labeled protein profile decreased monotonically with time and >90% of the initial dose delivered was released by 21 days. The percentage of protein remaining in the defect region was significantly elevated in the mesh/alginate group compared to collagen sponge at both 3 and 7 days post-implantation. Based on a simple release model, the protein profiles were fit to an exponential decay to estimate the half-life of release (R^2= 0.946 and 0.857 for collagen sponge and mesh/alginate groups, respectively). Overall, the half-life of release was 1.87 days (95% CI: 1.49 - 2.49 days) and 3.19 days (95% CI: 2.23 - 5.59 days) for the collagen sponge and mesh/alginate, respectively, though the difference did not reach statistical significance with p = 0.094. No significant differences in spatial distribution were found between the groups at any time point (data not shown).

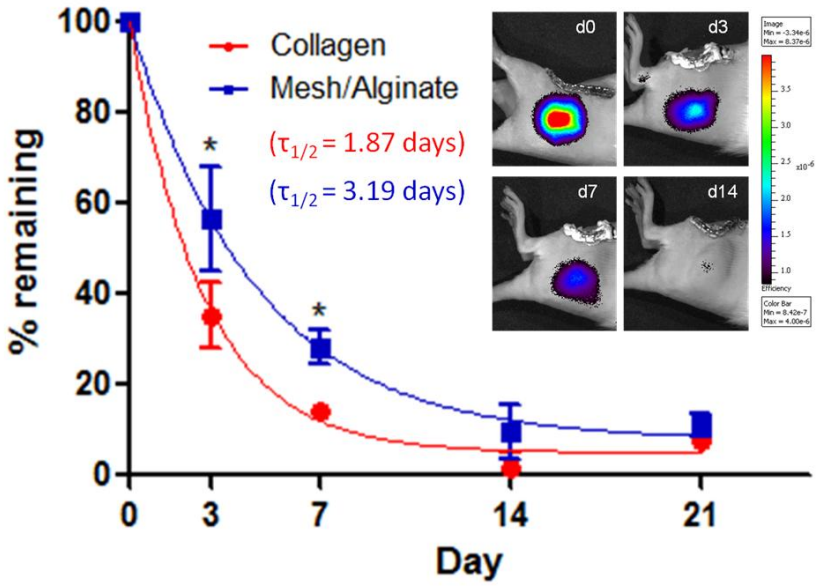

Figure 3.11. BMP release: in vivo tracking of fluorescent tag-labeled rhBMP-2 (inset) over 21 days revealed a significantly elevated protein retention in the mesh/alginate group compared to collagen sponge at day 3 and 7 post-implantation. Solid lines represent curve fit to exponential decay (R^2 = 0.946 and 0.857 for collagen sponge and mesh/alginate groups, respectively). The half life of release was 1.87 days (95% CI: 1.49 to 2.49 days) and 3.19 days (95% CI: 2.23 to 5.59 days), for the collagen sponge and mesh/alginate, respectively. *: $p < 0.05$ mesh/alginate vs. collagen sponge.

SDS-PAGE analysis verified that the tagged protein had similar molecular weight to the untagged protein (Figure 3.12). In vitro bioactivity assays and bone formation in vivo demonstrated that the tagged rhBMP-2 maintained biofunctionality, capable of inducing osteogenic differentiation of mesenchymal stem cells to a similar degree as un-tagged protein, as measured by calcium deposition in vitro (Figure 3.13A), though tagged protein induced a lesser amount of bone formation in vivo suggesting a somewhat reduced activity (Figure 3.13B).

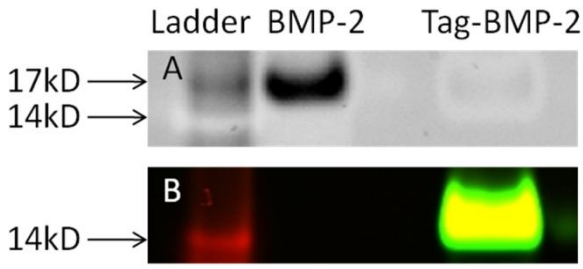

Figure 3.12. SDS-PAGE analysis of rhBMP-2 and fluorophore-tagged rhBMP-2 under reducing conditions. (A): SYPRO-Ruby protein gel stain illustrating untagged rhBMP-2 and tagged rhBMP-2 at similar molecular weight. (B): fluorescence imaging further verified the presence of tagged protein with functional fluorophore. Both labeled and unlabeled protein weighed approximately 17 kDa.

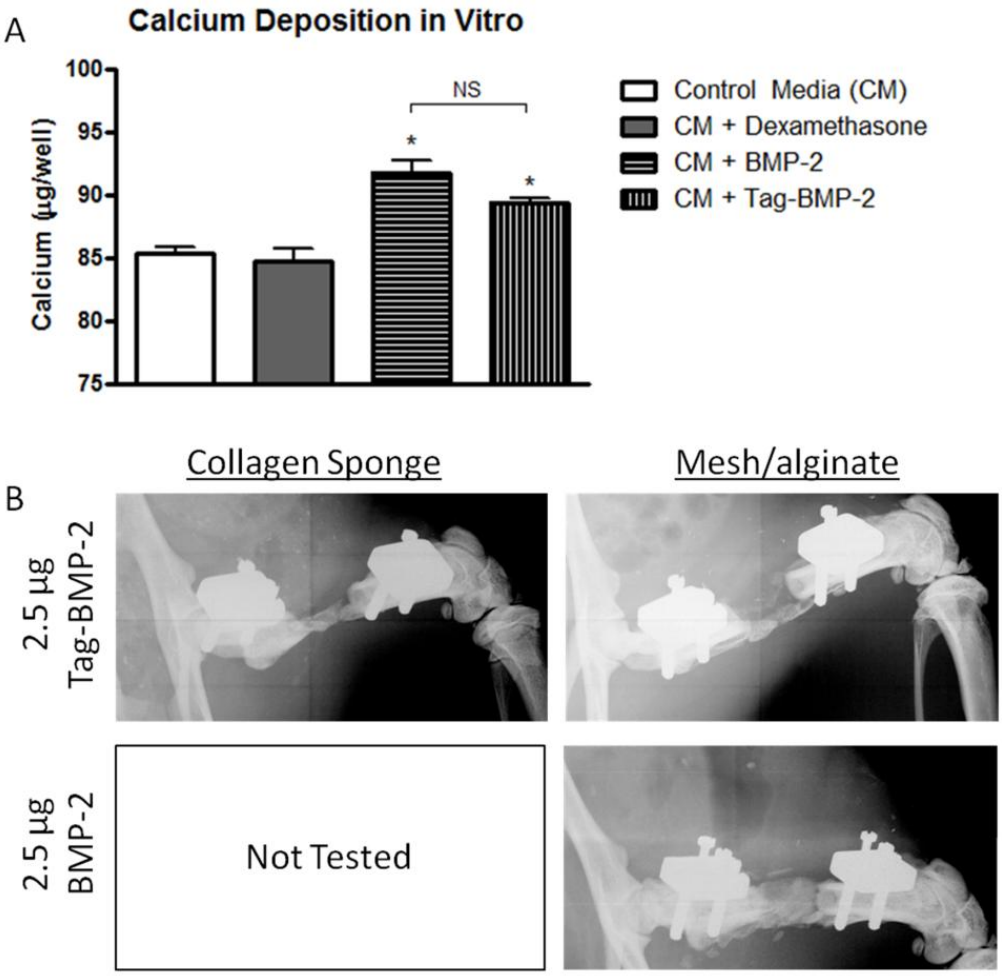

Figure 3.13. Labeled protein bioactivity analyses. (A): In vitro calcium deposition of MSCs after exposure to rhBMP-2 and fluorophore-tagged rhBMP-2. * indicates $p < 0.05$ vs. both CM and CM + Dex. NS = not significant. (B): Faxitron images of bone formation under tagged bmp-2 vs. non-tagged rhBMP-2 at 2.5 µg. In vitro bioactivity assays and bone formation in vivo demonstrated that the tagged rhBMP-2 maintained biofunctionality, capable of inducing osteogenic differentiation of mesenchymal stem cells to a similar degree as un-tagged protein, though tagged protein induced a lesser amount of bone formation in vivo suggesting a somewhat reduced activity.

DISCUSSION

Delivery of recombinant proteins carries great promise for the field of regenerative medicine; however, optimal doses and delivery vehicles have not yet been

determined. This study presents the dose-response relationships for rhBMP-2 delivered in a controlled-release hydrogel in comparison to the currently-used collagen sponge carrier, and revealed a reduction in the necessary effective dose for the spatiotemporal delivery system.

Dose-dependency

When delivered in the nanofiber mesh/alginate delivery system, rhBMP-2 induced bone regeneration in a nonlinear dose-dependent manner, as evaluated by bridging rate, bone volume, connectivity, and mechanical properties. Interestingly, the dose-response curves for bone volume and connectivity exhibited linear biphasic characteristics, with the slope significantly decreasing after the onset of bridging at 1.0 μg. This decrease in responsiveness to rhBMP-2 with increasing dose is likely due to saturation of BMP receptors and responding cell supply or simply from bone filling up available space in the defect region. Consistent with the onset of defect bridging, torsional stiffness and strength were not dose-responsive at less than 1.0 μg, but at higher doses, exhibited significant dose-dependent increases in mechanical properties.

The observation that mechanical properties did not level off within the range of growth factor dose analyzed may be explained by the histological observation that alginate degradation also proceeded in a dose-dependent manner, such that at higher doses, increased gel degradation allowed improved mechanical integrity. Since alginate is algae-derived, it cannot be enzymatically degraded *in vivo*, requiring hydrolysis or loss of the cross-linking Ca^{2+} ions for degradation [224]. The observed increase in cell and tissue infiltration with increasing dose may have increased the number of cells responsible for clearing foreign material and exposed more of the alginate surface for hydrolysis,

contributing to the dose-dependence of gel degradation. Another possible explanation is that the presence of the rhBMP-2 in the gel directly affected mechanical properties or degradation profiles independent of cellular and tissue interactions. Together, these effects allowed increased mechanical integrity in the higher doses which contained more bone and lower amounts of residual hydrogel.

For comparison, the mechanical properties of age-matched intact femurs were 0.030 ± 0.001 N-m/deg and 0.31 ± 0.02 N-m for torsional stiffness and failure torque, respectively [276]. At the 5.0 μg dose, the torsional stiffness of the regenerated defects exceeded the intact bone stiffness, while the failure torque reached about 60% of that of the intact bone. A previous study using this model demonstrated similar results, with mesh/alginate delivery of 5 μg rhBMP-2 reaching about 75% of intact bone properties for both stiffness and torque, though these were not statistically different from the native bone properties [14].

The nanofiber mesh tube, while serving to spatially retain the alginate and resulting bone formation within the defect, also appeared to be supportive of bone formation. Osteocyte-populated woven bone developed on the surfaces of the nanofiber meshes, in some cases creating sheets of bone which highlighted the presence of the mesh perforations. This observation was most clearly observed in the 0.5 μg group and, though present, was less noticeable in the higher dose groups as the defects were filled with bone. This suggests that rhBMP-2 was either binding to the nanofiber mesh and inducing bone formation locally, or perhaps more likely, the mesh was conducive to cellular migration and differentiation, allowing migration of periosteal cells along the mesh. This later possibility is corroborated by in vitro studies conducted in our laboratory

which demonstrated increased mesenchymal stem cell migration and osteogenic differentiation on nanofiber meshes compared with tissue culture plastic [281].

Delivery System Comparison

Bone formation was significantly increased in the nanofiber mesh/alginate delivery system over the current clinically-used collagen sponge delivery method for the 1.0 μg groups. Although the amount of bone formation was similar at week 4, by week 8 there was significantly greater bone volume in the mesh/alginate group compared to the collagen sponge group, and this difference increased through week 12. By week 4, the amount of active rhBMP-2 remaining in the defect would likely be minimal for both groups, however, this enhancement in bone formation between week 4 and week 8 in the mesh/alginate system may be attributed to an increased attraction of cells into the defect at earlier time points or enhanced activation of those cells from the released rhBMP-2, resulting in elevated activity through week 8. 0.1 μg rhBMP-2 was not sufficient to induce robust bone formation; however, 0.1 μg caused substantial increases in cellular migration into the defect compared to mesh/alginate-only treatment, demonstrating that even a low dose of rhBMP-2 possesses potent chemoattractant capacity for endogenous cells [282] and suggesting that low doses of rhBMP-2 may be useful for combination strategies involving gene therapy or growth factor co-delivery which require a strong host cell response. To facilitate cellular invasion, the alginate gel was functionalized with RGD peptides. RGD (Arg-Gly-Asp) is the primary sequence motif of fibronectin responsible for integrin binding, and may have enhanced protein-cell-matrix interactions and the ability of cells to migrate into the defect [224]. The RGD alone was not sufficient to induce cellular invasion or gel dissolution, as evident in the 0.0 μg group, though

cellular infiltration and associated gel fragmentation increased in an rhBMP-2 dose-dependent manner.

Although early bone formation occurred at a similar rate between delivery systems, an early enhancement in connectivity was observed in the mesh/alginate group, and this difference persisted through week 8. In both delivery systems, however, the connectivity decreased with time, despite increasing with dose of rhBMP-2, resulting in similar connectivity at week 12. As connectivity is a normalized measure of the number of redundant structures, the dose-dependent increase may be explained by an increase in the number of bone nucleation sites. However, as time progressed, spaces between distinct islands of bone filled in, reducing the total number of unique structures within the defect space, causing a reduction in connectivity over time, though the actual integrity increased.

Differences in mechanical properties between the collagen and mesh/alginate systems did not reach statistical significance, though the trends were consistent with the observed differences in bone formation. As seen histologically, the alginate hydrogel did not fully degrade over the time course of the study, and the extant alginate gel may have interfered with the mechanical integrity of the resulting bone by preventing complete interconnectivity. This underscores the importance of optimizing carrier degradation kinetics and protein-carrier concentrations for effective sustained delivery.

To explain the differences in bone formation between the two delivery systems, we quantified the *in vivo* protein release profiles of each. Sustained delivery vehicles for recombinant proteins have been studied previously, primarily using ^{125}I-labeled proteins [225, 280, 283-288]. In this study, the protein release kinetics from the collagen sponge

were similar to those reported previously in ectopic bone formation models, in which the retention half-life ranged from several hours to several days [289-292]. In comparison to collagen sponge, the sustained delivery method examined here increased the protein retention, and resulted in a 2.5-fold increase in bone volume over collagen sponge delivery.

A possible limitation of the protein tagging technique is that the fluorophore attachment may have altered the release properties of the protein. However, since the protein was not substantially changed in size as a result of complexation and did maintain bioactivity, albeit somewhat reduced *in vivo* compared to un-tagged protein, it is likely that the diffusion properties were not substantially changed. Regardless, both collagen sponge and mesh/alginate delivery systems were analyzed with the same tagged protein, allowing direct comparison. As with all protein labeling techniques, the entity being tracked is the fluorophore, with the degree of fluorophore-protein dissociation an unknown. Dissociation would result in measurement of faster release kinetics than actually exist as the fluorophore is substantially smaller in size than the fluorophore-protein complex, resulting in greater diffusivity according to the Einstein-Stokes relation. However, in this experiment, both groups received the same labeled protein, processed identically, and the fluorophore-protein dissociation rate is not likely to differ between delivery systems. Together, these limitations accentuate the importance of including the collagen group when evaluating sustained delivery vehicles for recombinant proteins to provide direct comparison of the novel therapeutic with the clinical standard.

In this study, several combined factors may have prolonged the protein release in the mesh/alginate system. First, the alginate hydrogel mesh structure provides a

diffusional barrier to BMP release, whereas the collagen sponge relies mostly on desorption. Second, the slow degradation kinetics of the alginate gel, despite inhibiting whole bone remodeling, may have contributed to the slower release kinetics. Third, the presence of the nanofiber mesh tube has been shown to maintain spatial retention of alginate in the defect [14] and may contribute to protein retention as well. Finally, since alginate carries a negative charge [293], and rhBMP-2 carries a positive charge of 10.5 at pH 7.4 [294], the opposite protein-matrix charge interactions may also have contributed to protein retention. Specifically, alginate has been shown to reversibly bind to heparin-binding proteins such as BMP-2 due to the abundance of basic residues in the heparin binding sequence, promoting interaction with negatively charged carboxyl groups on the alginate chain [295-296]. This interaction has been shown to enhance the biological activity of these proteins, likely through protection from degradation [286].

Much attention has recently been placed on developing improved carriers for both rhBMP-2 and hOP-1 [225, 297-298]. Likewise, the kinetics of protein release have been shown to have profound effects on protein effectiveness and efficiency [225, 280]. For example, Li et al. evaluated the bone formation capacity of rhBMP-2 when delivered in polyurethane scaffolds possessing different release kinetics, and found improved healing in scaffolds featuring an initial burst followed by sustained release [299]. Subsequently, Brown et al. demonstrated that a burst followed by a sustained release of rhBMP-2 regenerated 50% more bone compared to collagen sponge [300]. These results suggest that some amount of early release combined with sustained delivery may enhance growth factor efficacy, and together with the present data emphasize the importance of spatiotemporal growth factor presentation in tissue-engineered bone regeneration.

Conclusions

These data demonstrate the dose-response and temporal release of rhBMP-2 in a spatiotemporal protein delivery system, in comparison to the clinical standard collagen sponge. This work demonstrates an improvement in bone formation over current rhBMP-2 delivery methods, and highlights the importance of quantification of release kinetics and scaffold degradation properties for evaluating novel recombinant protein carriers.

CHAPTER IV: EFFECTS OF IN VIVO MECHANICAL LOADING ON LARGE BONE DEFECT REGENERATION*

ABSTRACT

Fracture healing is highly sensitive to mechanical conditions; however, the effects of mechanical loading on large bone defect regeneration have not been evaluated. In this study, we investigated the effects of functional loading on repair of critically sized segmental bone defects. Six-mm defects were created in rat femora, and each defect received 5 μg recombinant human bone morphogenetic protein-2 (rhBMP-2), delivered in alginate hydrogel. Limbs were stabilized by either stiff fixation plates for the duration of the study or compliant plates that allowed transfer of compressive ambulatory loads beginning at week 4. Healing was assessed by digital radiography, microcomputed tomography, mechanical testing, histology, and finite element modeling. Loading significantly increased regenerate bone volume and average polar moment of inertia. The response to loading was location-dependent with the polar moment of inertia increased at the proximal end of the defect but not the distal end. As a result, torsional stiffness was 58% higher in the compliant plate group, but failure torque was not altered. In the limited number of samples assessed for histology, a qualitatively greater amount of cartilage and a lesser degree of remodeling to lamellar bone occurred in the loaded group compared to the stiff plate group. Finally, principal strain histograms, calculated by FE modeling,

* This chapter is under review for publication in the Journal of Orthopaedic Research.

revealed that the compliant plate samples had adapted to more efficiently distribute loads in the defects. Together, these data demonstrate that functional transfer of axial loads alters BMP-induced large bone defect repair by increasing the amount and distribution of bone formed within the defect.

INTRODUCTION

Bone uniquely adapts and remodels its architecture and properties to respond to its mechanical environment, and mechanical forces are essential for proper morphogenesis and maintenance of normal bone structure and function [301]. Bone repair is also acutely responsive to loading, and both fracture healing and distraction osteogenesis are highly sensitive to mechanical stimuli, with the local mechanical environment being a primary determinant of the course and success of healing [1-2].

The benefits of mechanical stimulation in bone repair have only recently been recognized, as it was long held that complete immobilization was imperative for successful fracture healing and that the resorptive effect of disuse was necessary to release calcium for callus mineralization [302]. However, the continued study of biomechanical factors in fracture healing has drastically changed the way that fractures are clinically addressed [106-107, 111]. It is now known that limited compressive interfragmentary movements induce endochondral ossification and have a stimulatory effect on callus formation and subsequent healing [1, 105, 109, 114].

Although biomechanical modulation of fracture healing has been well studied, the ability of mechanical stimulation to enhance large bone defect repair has not yet been quantitatively evaluated. Large bone defects, caused by traumatic injury, tumor resection,

or degenerative disease, remain a significant challenge for orthopaedic surgeons, as the current treatment options are limited by tissue availability and donor site morbidity, in the case of autografts, and failure to revitalize and remodel, in the case of allografts [9-10, 152]. Tissue engineering, the use of biomaterial scaffolds in combination with biologics and/or cells, has therefore emerged as a promising alternative to grafting techniques. One tissue engineering strategy that shows immense potential is the delivery of recombinant osteoinductive growth factors, such as members of the bone morphogenetic protein (BMP) family. Two of these, BMP-2 and BMP-7, have been approved for use in humans by the United States Food and Drug Administration (FDA), and have shown great promise in numerous animal models and clinical trials [182, 303-304]. The clinical delivery method for these proteins, however, may be inefficient as large doses are required, contributing to prohibitively-high costs and potential complications due to protein diffusion [182, 303]. A recently-developed growth factor delivery system, using an alginate hydrogel injected into a nanofiber mesh tube placed around the defect, has been shown to enhance functional repair of bone defects [305]. Such advances are increasing the potential to safely and effectively restore bone function in challenging segmental defects.

However, few studies have directly investigated the influence of mechanical conditions in tissue-engineered bone repair. While a number of laboratories have explored mechanical deformations of bone cells and tissue-engineered constructs in vitro [11, 232, 236, 238-239], very few have studied these in vivo [13, 306-307], and the potential of mechanical loading to enhance the regeneration of large bone defects has not been evaluated. This approach has the potential to improve clinical treatment of such

challenging defects as well as advance our understanding of the role of mechanical factors in bone tissue formation, differentiation, and remodeling. The aim of this study was therefore to test the hypothesis that transfer of compressive ambulatory loads during segmental bone repair enhances bone formation and subsequent regeneration.

MATERIALS AND METHODS

Surgical Procedure

Bilateral 6 mm femoral defects were surgically created in 13 week old female SASCO Sprague Dawley rats (Charles River Labs, Wilmington, MA) under isoflurane anesthesia as previously described [275]. Limbs were stabilized by either stiff or axially-compliant fixation plates as characterized previously [276] (n = 10 per group, Figure 4.1A-C). The compliant plates maintained a high stiffness to bending and torsional loads, but allowed transfer of compressive ambulatory loads through integrated elastomer segments (RTV Silicone Adhesive, Factor II, Inc., Lakeside, AZ) that conferred a low axial stiffness [276]. The compliant plates also featured a locking mechanism to allow elective actuation of load-sharing after an initial healing period, selected to be 4 weeks in the current study. The axial, torsional, and bending properties of the plates in each configuration are shown in Table 4.1. In the locked configuration, the compliant plates featured an axial stiffness of 349.5 ± 35.1 N/mm, which was reduced to 8.4 ± 0.4 N/mm by plate actuation. By comparison, the stiff plates featured an axial stiffness of 214.3 ± 4.1 N/mm [276].

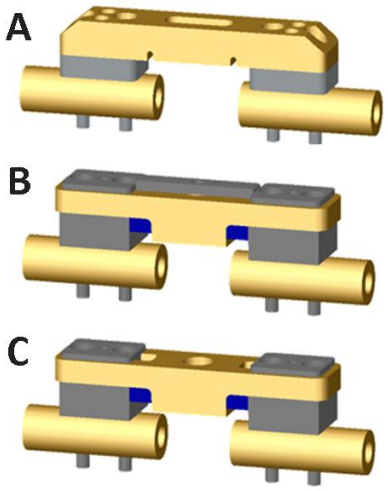

Figure 4.1. Fixation plate designs. (A): Stiff plate. (B): Locked compliant plate. (C): Actuated compliant plate.

Table 4.1. Fixation plate mechanical characterization. All values given as mean ± standard deviation.

	Stiff Plate	Compliant Plate	
		Actuated	Locked
Axial Stiffness (k) without scaffold [N/mm]	214.3 ± 4.1	8.4 ± 0.4	349.5 ± 35.1
Axial Stiffness (k) with scaffold [N/mm]	256.3 ± 32.8	87.0 ± 28.3	404.9 ± 60.3
Torsional Stiffness (GJ/L) [kN-m/deg]	14.8 ± 1.61	6.95 ± 0.18	9.14 ± 2.94
Flexural Rigidity (EI) concave [N-mm^2]	29236.3 ± 260.8	25688.3 ± 657.4	26938.7 ± 629.5
Flexural Rigidity (EI) convex [N-mm^2]	30472.0 ± 736.8	28015.0 ± 2076.1	42392.0 ± 8350.1

Preliminary experiments (not shown) suggested that without defect bridging, mechanical loading may not have a beneficial effect. Therefore, in this experiment, 6 mm defects were used to ensure bridging of the defects at the onset of mechanical loading at week 4. An initial pilot study verified that these defects were critically sized, and bony bridging was not observed in empty defects or defects with a mesh tube-only (Figure 4.2A, B).

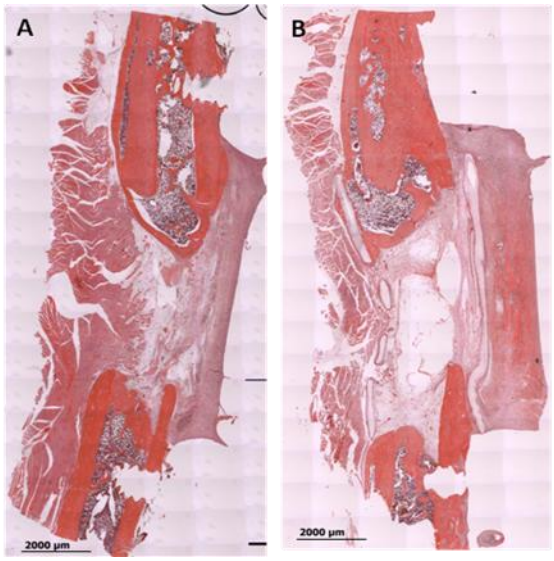

Figure 4.2. Week 12 histological staining: Haematoxylin and Eosin-stained sections of empty (A) and nanofiber mesh-only treated (B) defects at week 12 post-surgery. In the absence of rhBMP-2, the defects filled with fibrous tissue and resulted in non-union. Histological assessment demonstrated that in both groups, the defect ends were capped off by new bone (red), with muscle and fibrous tissue invasion (pink) into the defect from the periphery in the empty group and fibrous tissue and regions of empty space in the nanofiber mesh-only group. Limbs failed to bridge without treatment, confirming the critical nature of the model.

After limb stabilization, a nanofiber mesh tube was inserted over the native bone ends, surrounding the defect as described in Chapter 1. 100 µl of alginate hydrogel, containing 5 µg of BMP-2, was then injected into each mesh using a blunt-tipped 22g needle, filling the defect space.

Animals were given subcutaneous injections of 0.04 mg/kg buprenorphine every 8 h for the first 48 h post-surgery and 0.013 mg/kg every 8 h for the following 24 h. All procedures were reviewed and approved by the Georgia Institute of Technology Institutional Animal Care and Use Committee (Protocol No. A08032).

Nanofiber Mesh Production

Nanofiber meshes were produced as described previously by electrospinning poly-(ε-caprolactone) (PCL) onto a static collector [308]. Briefly, PCL was dissolved at a concentration of 12% (w/v) in a 90:10 volume ratio of hexaflouro-2-propanol:dimethylformamide (Sigma-Aldrich) and electrospun onto a collector. Twenty-four 1 mm diameter perforations were patterned into the sheets, which were then glued into tubes of 4.5 mm diameter and 10 mm length. Mesh tubes were sterilized by 100% ethanol evaporation.

Alginate & Growth Factor Loading

Recombinant human BMP-2 (R&D Systems, Minneapolis, MN) was reconstituted in 0.1% rat serum albumin in 4mM HCl, and mixed with RGD-functionalized alginate (courtesy of David Mooney, Harvard University) [277] to a final concentration of 50 µg/ml in 2% alginate. To crosslink the alginate, this solution was mixed rapidly with 0.84% (m/v) $CaSO_4$. Each defect received a total of 5 µg BMP-2.

Faxitron and MicroCT

Two-dimensional digital radiographs (Faxitron MX-20 Digital; Faxitron X-ray Corp., Wheeling, IL) were taken at 2, 4, 8, and 12 weeks post-surgery with an exposure time of 15 s and a voltage of 25 kV (n=10 per group). In vivo micro-computed tomography (microCT) scans (Viva-CT 40; Scanco Medical, Basserdorf, Switzerland) were performed at 4, 8, and 12 weeks post-surgery at medium resolution and 38.5 µm isometric voxel size with the scanner set at a voltage of 55 kVp and a current of 109 µA. The volume of interest (VOI) used for quantification of bone volume and bone density encompassed all bone formation within the center 100 slices (3.85 mm) between the

native bone ends. New bone formation was segmented by application of a global threshold (386 mg hydroxylapatite/cm^3) corresponding to 50% of the native cortical bone density, and a Gaussian filter (sigma = 1.2, support = 1) was used to suppress noise.

After 12 weeks (8 weeks after compliant plate actuation), the animals were euthanized by CO_2 asphyxiation, and the limbs were excised for microCT scanning to quantify bone distribution (n=8 per group). Ex vivo scans were performed as above at medium resolution with a 21 μm voxel size. The ex vivo VOI included the defect plus 2 mm of native bone on each end, to encompass the entire region exposed to a torsional moment during mechanical testing. To assess the cross-sectional bone distribution, the "Bone Midshaft" evaluation script (Scanco Medical, Basserdorf, Switzerland) was used to quantify polar moment of inertia (pMOI).

Biomechanical Testing

Femora (n=8 per group) were then biomechanically tested in torsion to failure as described previously [275]. Briefly, limbs were cleaned of soft tissues and the ends potted in Wood's metal (Alfa Aesar, Wood Hill, MA). The fixation plates were then removed, and limbs were mounted on a Bose ElectroForce system (ELF 3200, Bose EnduraTEC, Minnetonka, MN) and tested to failure at a rate of 3º/sec. Maximum torque at failure and torsional stiffness, given by the slope of the line fitted to the linear region of the torque-rotation curve, were computed for each sample.

Histology

One sample per group was taken for histology at week 5 (one week after compliant plate actuation) and at week 12 post-surgery. Samples were fixed in 10% neutral buffered formalin for 24 hours at 4ºC, and then transferred to a formic acid-based

decalcifier (Cal-ExII, Fisher Scientific) for 2 weeks, under mild agitation on a rocker plate. Following paraffin processing, 5 μm-thick mid-saggital sections were cut and stained with Picrosirius red [309] and Safranin-O/Fast-green [278]. Cartilage areas in Safranin-O sections were segmented and evaluated by using a colorimetric threshold (Axiovision, Carl Zeiss, Germany). Manual contouring of lamellar and woven bone areas in ImageJ [310] allowed comparison of organization and maturity in Picrosirius red sections.

Finite Element Modeling

MicroCT-generated reconstructions of three representative defects per group were subjected to finite element (FE) analysis following voxel to element conversion (voxel size: 42 μm), and the spatial and frequency distributions of maximum and minimum principal strains were determined under physiologic loads. Rat femoral loads caused by gravitational impact during ambulation have previously been estimated as one half the body weight (BW) [311]; however, there is increasing evidence that muscle contraction loads contribute significantly to adaptive signals [312]. Therefore, in vivo femoral loads, P_{femur}, were assumed to be axially-oriented at a magnitude of $1.0 \cdot BW$. Traction boundary conditions on the in-grown bone, P_{defect}, were then determined by the "rule of mixtures," to account for load-sharing with the fixation plate:

$$P_{defect} = P_{femur} \cdot \frac{k_{defect}}{k_{defect} + k_{plate}}, \qquad \text{(Eqn. 4.1)}$$

where k_i = axial stiffness of the i^{th} species, and P_i = axial load on the i^{th} species, for both stiff and compliant plate samples. A sensitivity study was conducted to evaluate the effect of error in femoral load estimation on local mechanical conditions. The cortical bone ends were segmented and given a modulus of 10 GPa [313], while the newly-formed

bone properties were determined by back-calculation from physical tests. The Poisson ratio was assumed to be 0.33.

To estimate a modulus for newly-formed bone, separate samples were tested nondestructively in axial compression to an effective strain of 1200 μstrain. Axial loads and effective defect strains, measured by laser extensometer (LX 500, MTS, Eden Prairie, MN), were used to determine axial stiffness (k_{actual}). Corresponding microCT reconstructions were subjected to the analogous FE analysis to yield an axial stiffness (k_{FE}) based upon an arbitrary elastic modulus (E_{FE} = 2000MPa). Linear correlation between measured and calculated stiffness values [306] provided the elastic tissue modulus,

$$E_{actual} = E_{FE} \cdot \frac{k_{actual}}{k_{FE}} \qquad \text{(Eqn. 4.2)}$$

Statistical Analyses

All data are presented as mean ± standard error of the mean (SEM). Differences between groups, among time points, and among spatial regions, accounting for animal variability, were assessed by two- and three-factor analysis of variance (ANOVA), as appropriate. Individual comparisons were made by Tukey's post hoc analysis. Comparison of regression lines was performed by analysis of covariance (ANCOVA). A p-value < 0.05 was considered significant. Minitab® 15 (Minitab Inc., State College, PA) was used to perform the statistical analysis. A list of analyses performed and associated sample sizes is shown in Table 4.2.

Table 4.2: Analyses performed and sample sizes for both stiff and compliant plate groups.

Analysis Method	Time Points (week)	N (per group)
Faxitron	4, 8, 12	10
MicroCT	4, 8, 12	8
Mechanical Testing	12	8
Histology	5	1
Histology	12	1
FE Modeling	12	3

RESULTS

Faxitron

Faxitron radiographs taken at weeks 4, 8 and 12 post-surgery confirmed that both stiff and compliant plates maintained limb stability, and the delivered growth factor induced bridging of the defects prior to compliant plate actuation at week 4, with bone completely filling the defect space by week 12 (Figure 4.3).

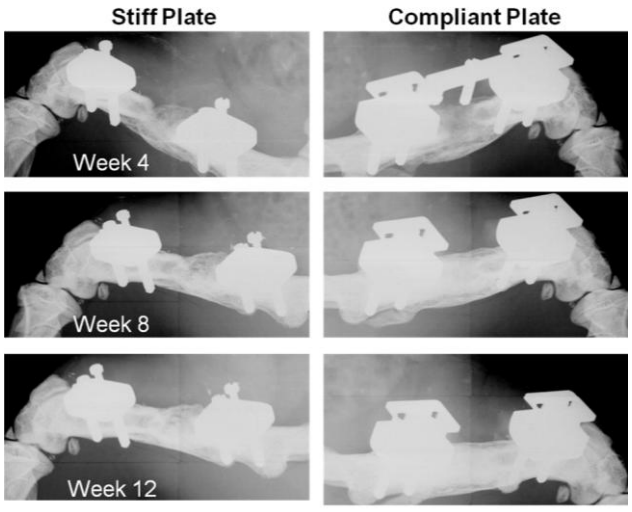

Figure 4.3. Representative digital radiographs taken at weeks 4, 8 and 12 post-surgery. The compliant plate was locked until plate actuation at week 4, followed by 8 weeks of functional loading.

MicroCT

In vivo microCT scans were performed every four weeks post-surgery. Prior to compliant plate actuation at week 4, the bone volume was not significantly different between groups; however, after 4 weeks of load transfer, at week 8, the compliant plate group featured a significantly greater bone volume than the stiff plate group, and this difference continued through week 12 (Figure 4.4A). Though both groups featured a continuous increase in mean density throughout the experiment, there were no differences in mean density between groups at any time point (Figure 4.4B). Three-dimensional reconstructions of the defects at week 12 demonstrated qualitative differences in bone distribution as a function of axial position (Figure 4.4C), though the local density distribution within the defect did not change along the bone axis or between groups (Figure 4.4D, data not shown).

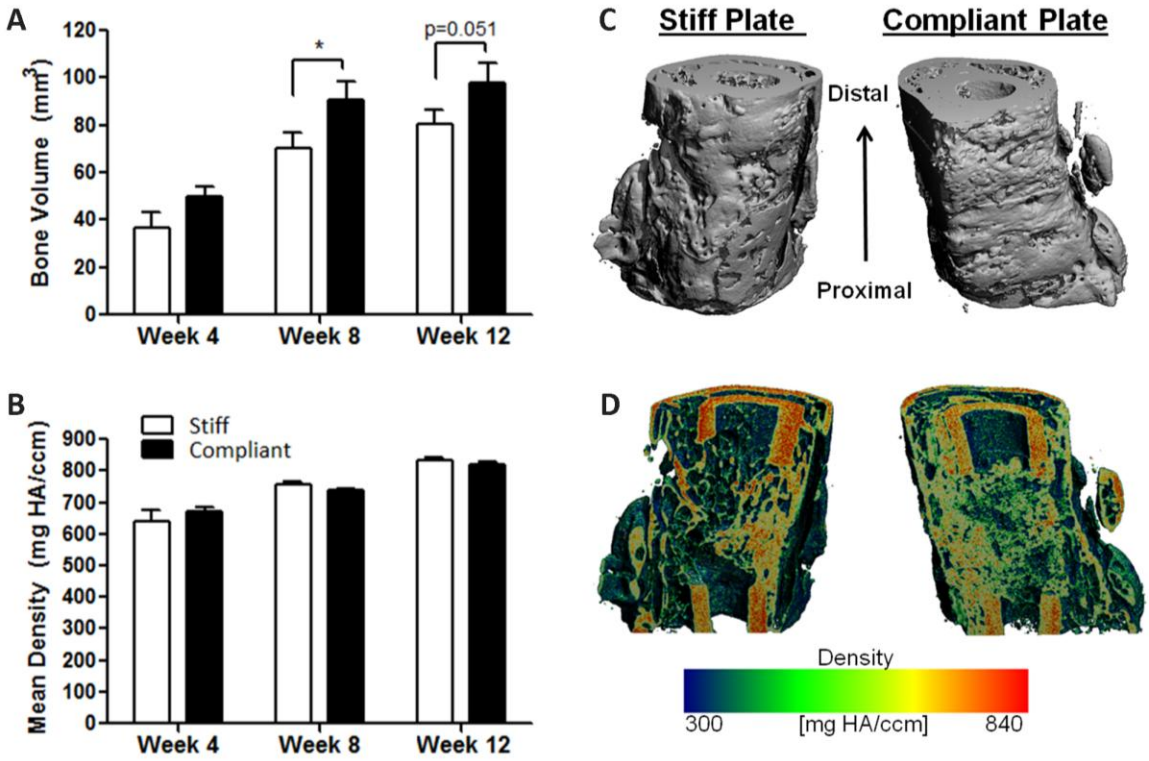

Figure 4.4. MicroCT analysis. Bone volume (A) and mean density (B) at weeks 4, 8, and 12 post-surgery. Bone formation was significantly increased after 4 weeks of loading in the compliant plate group over the stiff plate group. (C): Representative 3D reconstructions of limbs qualitatively demonstrated a difference in distribution between the proximal and distal ends of the defects. (D): Local density mapping on saggital cross sections illustrated internal distribution and maturity.

Biomechanical Testing

Post mortem mechanical testing was performed to assess the degree of functional regeneration of the limbs. Torsion tests demonstrated a significant 58.2% increase in torsional stiffness as a result of compliant fixation (Figure 4.5A); however, loading did not alter the maximum torque at failure (Figure 4.5B) or the work to failure (data not shown).

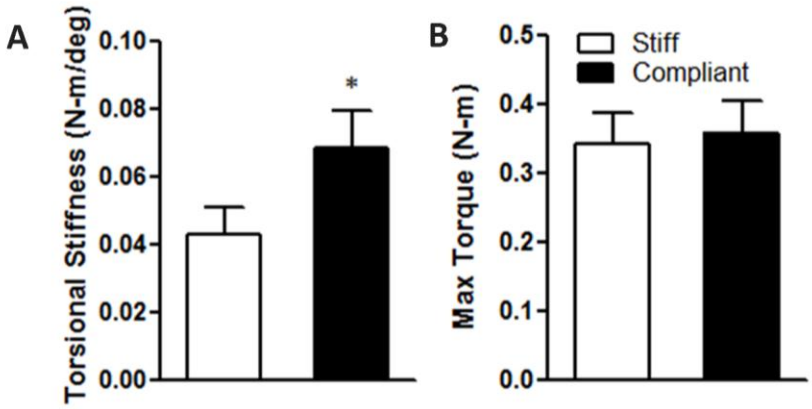

Figure 4.5. Biomechanical testing. Torsional stiffness (A), but not maximum torque at failure (B), was significantly enhanced by compliant fixation.

Bone Distribution

Compliant fixation resulted in a significant 30.4% increase in average polar moment of inertia (pMOI, Figure 4.6A). To quantify the location dependence of the bone distribution, the pMOI was graphed as a function of position from the defect center, x (Figure 4.6B). In both groups, linear regression indicated a significantly positive slope in pMOI vs. x (from distal to proximal end). The regression lines differed significantly, with the compliant plate group having both greater slope and intercept (Stiff: m=4.35 ± 0.386, b = 56.69 ± 1.05, R^2 = 0.7468; Compliant: m = 7.65 ± 0.448, b = 66.2 ± 1.22, R^2 = 0.8715).

As each data set more closely approximated a tri-phasic curve, with inflection points at the native bone ends, the pMOI values were binned into three regions, determined by the edges of the defect (Figure 4.6C). At the distal end, where the pMOI was a minimum, there was no significant effect of loading on bone distribution; however, in both the defect and proximal regions, loading significantly increased the bone distribution (Figure 4.6D).

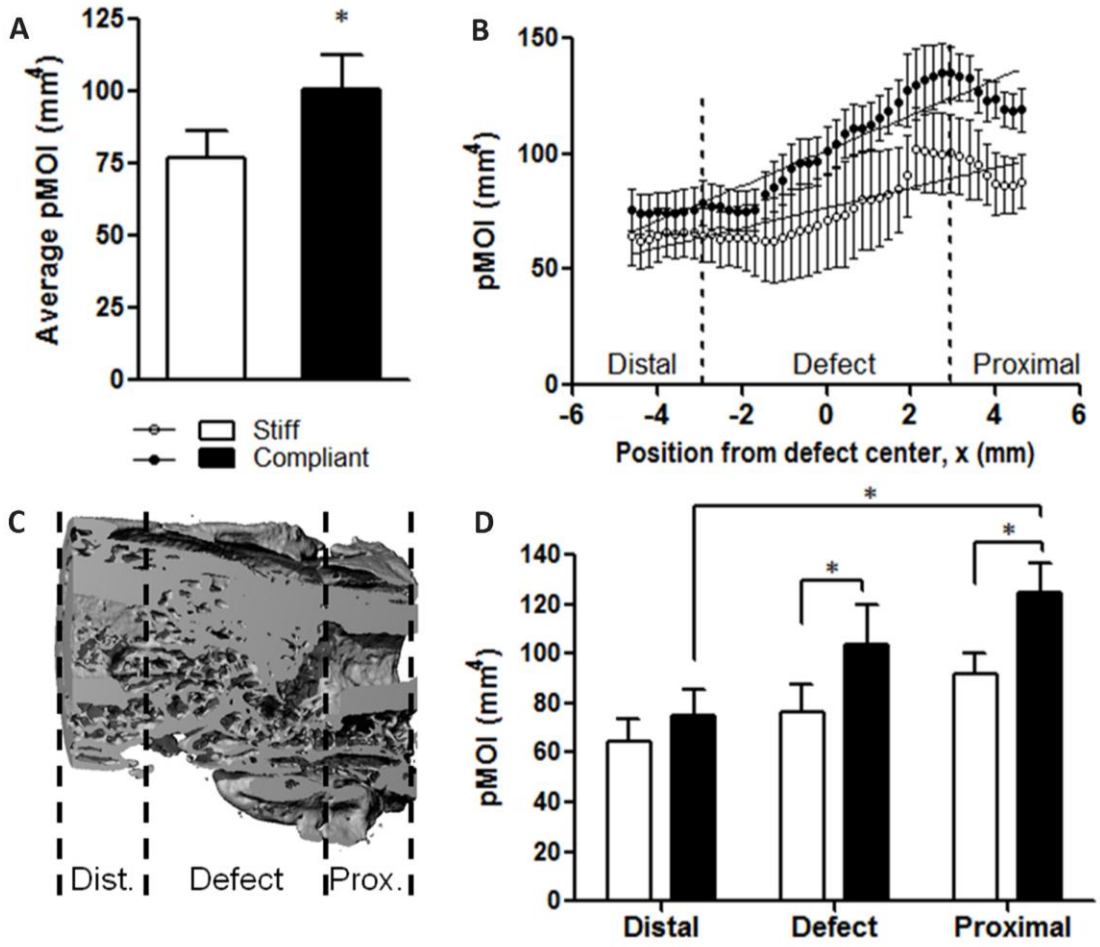

Figure 4.6. Moment of inertia analyses. (A): MicroCT revealed a significantly greater average polar moment of inertia (pMOI) in the compliant plate group at week 12. (B): Graph of local pMOI vs. distance from defect center quantitatively verified differences in distribution as a function of position. Also, the slopes of regression lines were significantly different between the two groups. (C): Illustration of regions used for binning data from B. (D): Comparison of average pMOI in each region, demonstrating no differences in distribution at the distal end where the pMOI was a minimum.

Histology

At weeks 5 and 12 post-surgery, one sample from each group was selected for histology. Picrosirius red staining, whose birefringence is specific for collagen [309], was performed to compare the local tissue organization and degree of cell-mediated remodeling between groups at weeks 5 and 12 post-surgery. When viewed under

polarized light, the collagen fibers become birefringent and distinguish organized lamellar bone from unorganized woven bone. Comparison of lamellar and woven bone areas qualitatively revealed no differences between groups after 1 week of loading, at week 5 (Figure 4.7A, B); however, by week 12, the stiff plate group had a greater proportion of lamellar bone, indicating a more remodeled architecture, while the compliant plate group appeared unchanged (Figure 4.7C, D).

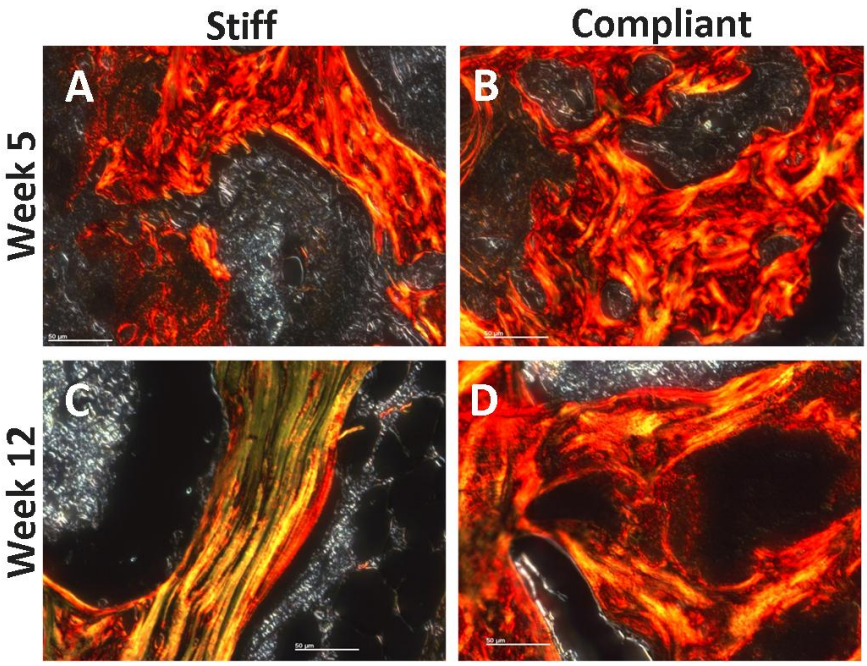

Figure 4.7. Picrosirius red-stained histology images, viewed under polarized light to highlight collagen I organization. (A): Stiff plate group at week 5. (B): Compliant plate group at week 5. (C): Stiff plate group at week 12. (D): Compliant plate group at week 12. Qualitatively, no differences were observed at week 5, one week after load initiation; however, a qualitatively greater proportion of lamellar bone was evident in the stiff plate group compared to the compliant plate group at week 12. Images are representative, selected based on average ratio of woven bone area:total bone area. Scale bars: 50μm.

Safranin-O/Fast-green revealed positive staining for cartilage in both groups and at both time points (Figure 4.8A-F). Cartilage appeared predominantly at the distal end of the defect, and very little cartilage staining was found near the proximal end (Figure

4.8A, B). In the limited number of samples evaluated, Safranin-O staining qualitatively demonstrated a larger amount of cartilage in the compliant plate samples compared to the stiff plate samples. At week 5, hypertrophic chondrocytes were evident at the edges of cartilage islands and embedded in mineralized matrix, suggesting an endochondral ossification process (Figure 4.8C, D). Comparatively, very few glycosaminoglycan (GAG)-secreting chondrocytes remained by week 12, and most remaining hypertrophic chondrocytes were fully surrounded by mineralized matrix (Figure 4.8E, F). Alginate gel also stained red but was acellular and therefore easily identifiable (Figure 4.8E, F).

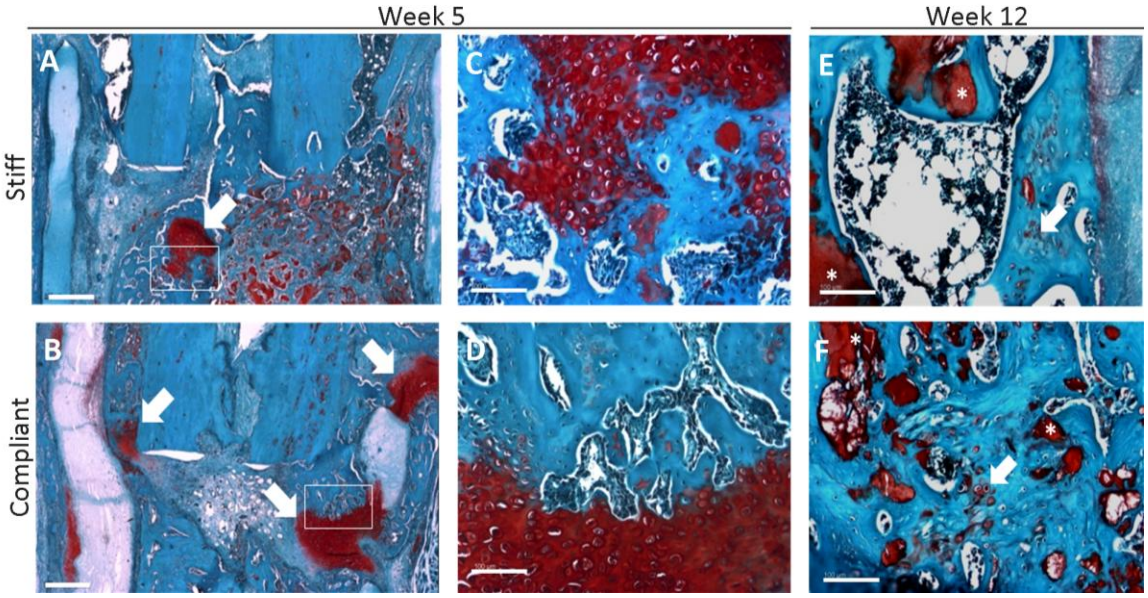

Figure 4.8. Safranin-O/Fast green-stained histology images at week 5 and 12 post-surgery. (A, B): Cartilaginous tissue at distal end of stiff and compliant plate groups, respectively, at week 5. Scale bars: 500µm. (C, D): Boxed areas from A and B, respectively, demonstrating hypertrophic chondrocytes and bone/cartilage interface. Scale bars: 100µm. (E, F): Hypertrophic chondrocytes (white arrows) embedded in mineralized matrix from compliant and stiff plate groups, respectively, at week 12. Qualitatively, a greater amount of cartilage formation was found in the compliant plate group, and in all samples, cartilage formation occurred predominantly at the distal end of the defects. Scale bars: 100µm.

Finite Element Modeling

Back-calculation of material properties from physical tests as described in methods determined the average tissue modulus for regenerate bone at week 12: E_{actual} = 628.43 ± 54.47 MPa. The in vivo defect loads, P_{defect}, were calculated to be 48% greater in the compliant plate group at week 12 (Stiff: 2.00 ± 0.18 N; Compliant: 2.95 ± 0.06 N, p=0.0072). Finite element analyses were then performed using these material properties and boundary conditions to assess the local stress/strain state under the different loading conditions at week 12 (Figure 4.9). Despite the greater load magnitudes in the compliant plate group, FEA demonstrated that the average principal strains were not different between the two groups (Figure 4.9A), which suggests an adaptive response in the compliant plate group to minimize overstrain by adding material. Accordingly, the FEA-derived apparent modulus of the compliant plate group was significantly increased over the stiff plate group (Fig 4.9B). This effect is further illustrated in the representative saggital sections with minimum principal strain mapping overlays (Figure 4.9C, D).

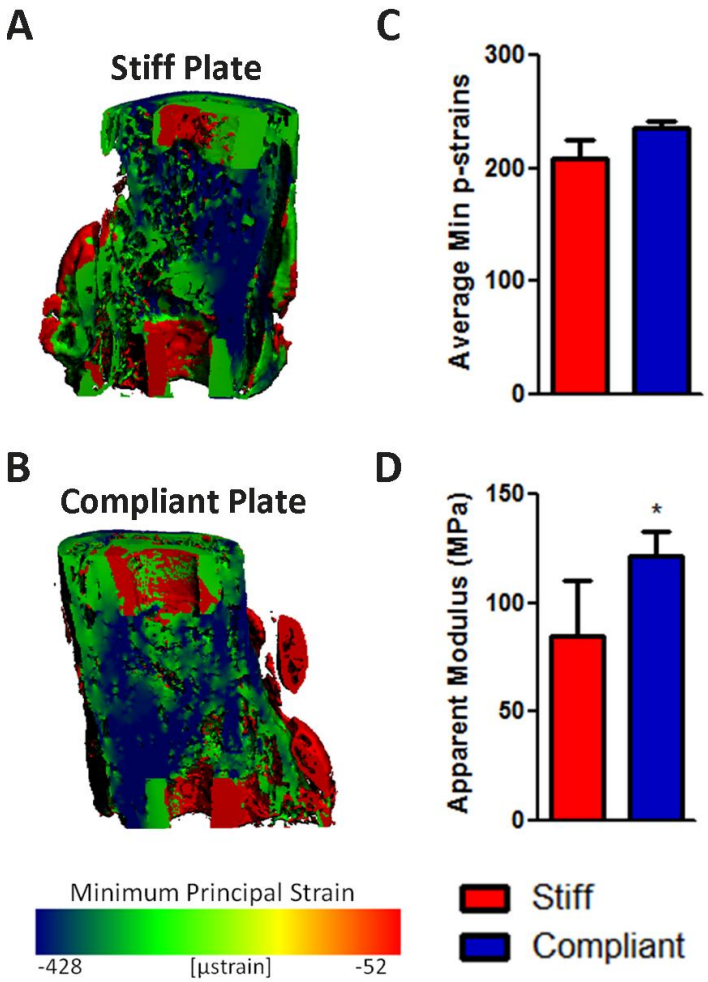

Figure 4.9. Finite element modeling at week 12: Local minimum principal strain mappings for stiff and compliant plate groups, respectively (A, B). Despite a greater amount of load transfer in the compliant plate group, the average principal strains were not different between groups (C). Accordingly, the apparent-level modulus was significantly greater in the compliant plate group (D).

At week 12, the minimum and maximum principal strains ranged from approximately -500 to 300 µstrain, respectively, for both groups, but the frequency distribution of these strains throughout the defect was significantly different between the groups (Figure 4.10). In the stiff plate group, a larger proportion of voxels carried very low strains (Figure 4.10A); whereas, in the compliant plate group, strains were more evenly distributed (Figure 4.10B). These observations were quantified by analysis of the

kurtosis of the distribution, a measure of the peakedness of a curve. The kurtosis was significantly greater in the stiff plate group, indicating a more peaked distribution, whereas the compliant group had a flatter distribution (Figure 4.10C).

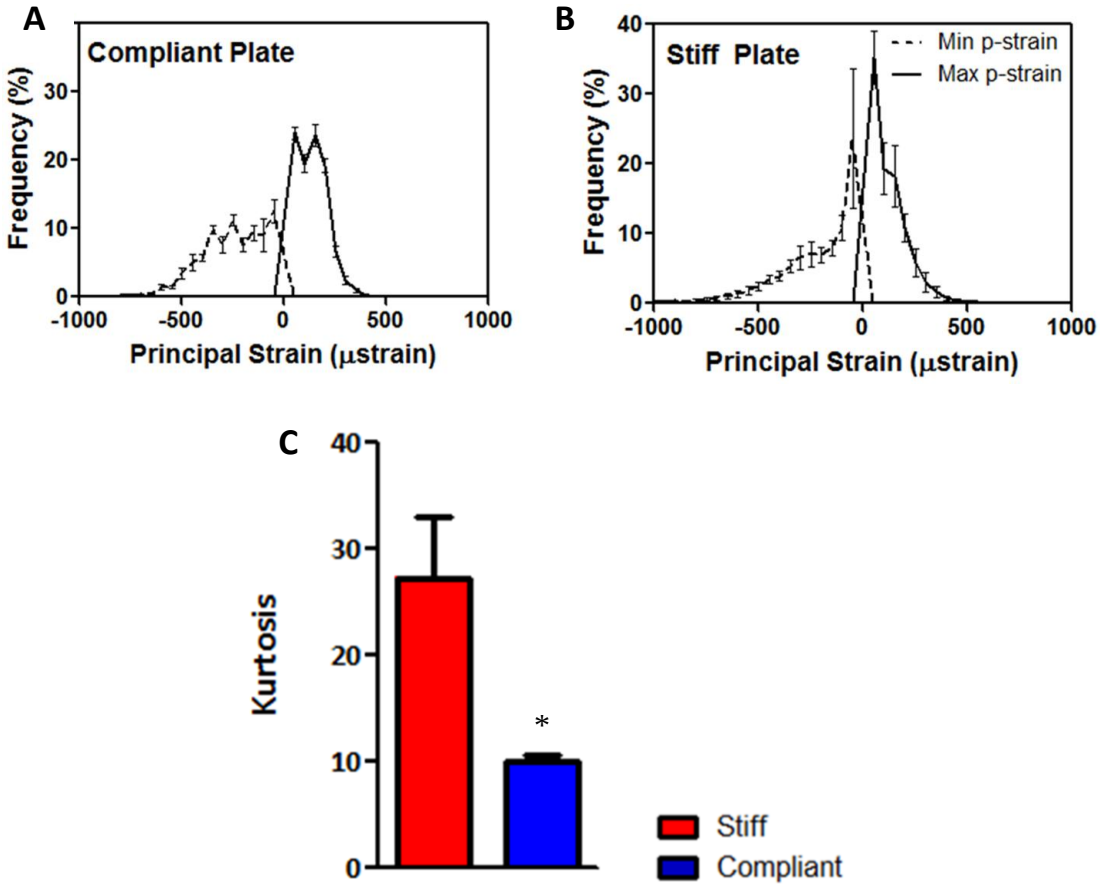

Figure 4.10. Principal strain histogram analysis. Frequency distributions of principal strains indicated that local strains were more evenly and efficiently distributed in the compliant plate group (A, B). Differences in distribution curves were quantified by kurtosis analysis (C). The kurtosis was significantly greater in the stiff plate group, indicating a more peaked distribution, whereas the compliant group had a flatter distribution.

Non-destructive Prediction of Biomechanical Properties

Finally, the ability of the non-destructive microCT and FEA to predict the elastic and failure properties of the regenerate bone defects was assessed by correlation of

physical and virtual test parameters. Bone volume alone was a poor predictor of biomechanical properties (Figure 4.11A, B). Including the cross sectional distribution through the average polar moment of inertia increased the explanatory power (Figure 4.11C, D); however, the best predictor of mechanical strength was the apparent modulus calculated by FE analysis, which predicted 78 and 59% of the variation in torsional strength and stiffness, respectively (Figure 4.11E, F).

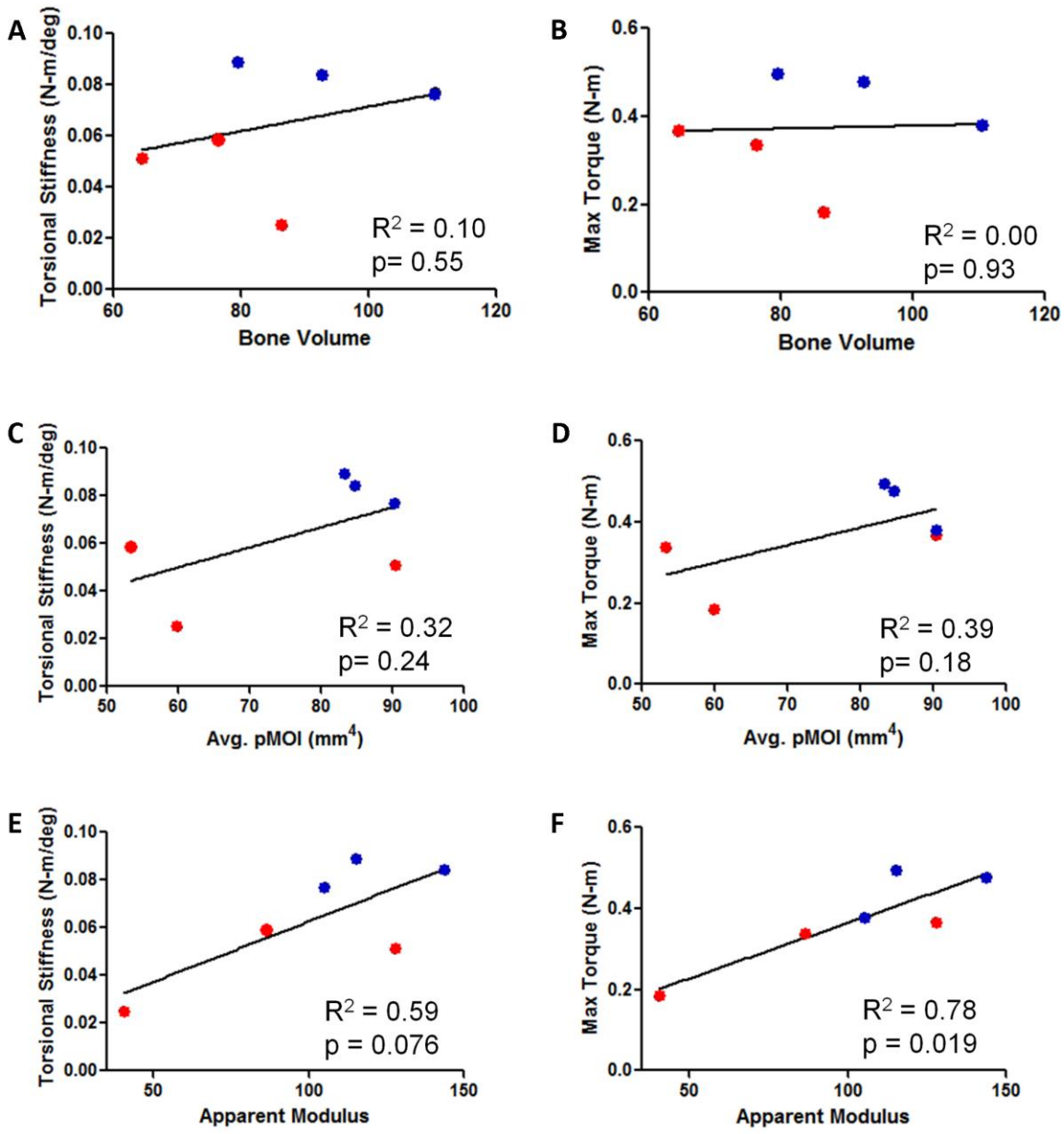

Figure 4.11. Correlations between physical tests and microCT and FEA parameters. **(**A, B): Torsional stiffness and maximum torque vs. bone volume. (C, D): Torsional stiffness and maximum torque vs. average pMOI. (E, F): Torsional stiffness and maximum torque vs. FEA-derived apparent modulus. The predictive power is increased by use of FEA compared with simple structural parameters yielded by microCT.

DISCUSSION

This study demonstrated that manipulation of fixation stiffness during the course of segmental bone defect healing significantly influences the amount, distribution, and biomechanical properties of regenerated bone within the defect. In this experiment, limbs were stabilized with either stiff plates or compliant plates designed to transfer axial loads to the ingrowing bone while resisting transfer of torsional and bending moments. Axial loading significantly increased bone formation and cross-sectional distribution, conferring a significant enhancement in elastic stiffness, but did not alter the maximum torque at failure or work to failure.

These observations may be explained by application of simple mechanics of materials theory to the distribution data. While loading significantly increased the average pMOI, it did not alter bone distribution at the distal end, where failure during biomechanical testing was observed. Assuming that the tissue modulus did not vary by position, the torsional stiffness is given by:

$$k_t = \frac{G \cdot J_{avg}}{L}, \qquad \text{(Eqn. 4.3)}$$

where G is the elastic shear modulus, J_{avg} is the average pMOI, and L is the gage length of the test. Thus, an increase in average pMOI, induced by mechanical stimulation, would cause a proportional increase in stiffness. Failure, however, occurs when the maximum shear stress reaches a critical value. The maximum shear stress in the limb is related, not to the average pMOI, but to the minimum pMOI by:

$$\tau_{\max} = \frac{T \cdot r}{J_{\min}}, \qquad \text{(Eqn. 4.4)}$$

where T is the torque, and r is the outer radius at the location of $J_{min,}$ the minimum pMOI. Since loading did not alter bone distribution at the distal end, where the pMOI was a minimum, the failure properties were not affected by loading.

For comparison, the mechanical properties of age-matched intact femurs were 0.030 ± 0.001 N-m/deg and 0.31 ± 0.02 N-m for torsional stiffness and failure torque, respectively [276]. A previous study using the same protein delivery system with 5 µg rhBMP-2 in 8 mm defects reached about 75% of intact bone properties for both stiffness and torque, though these were not statistically different from the native bone properties [314]. In this study, with a 6 mm defect, the stiffness and failure torque of the stiff plate group were similar to intact bone; however, in the compliant plate group, the torsional stiffness was significantly greater than that of the unoperated limbs.

The observed axial variation in distribution, regardless of fixation type, may be due to a variation in vascular supply, which could affect the availability of osteoprogenitor cells. Given a sufficient vascular supply, mesenchymal stem cells (MSCs) can differentiate into bone forming osteoblasts; however, in hypoxic environments, they may preferentially differentiate into chondrocytes [315]. Accordingly, in this experiment, positive staining for cartilage was evident primarily at the distal end of the defects, suggesting locally reduced perfusion. Likewise, in agreement with the strain-mediated tissue differentiation theories proposed by Carter, Perren, and others, more cartilage was found in loaded samples, at both week 5 and week 12 [148, 301]. This finding agrees with other in vivo model systems in which mechanical stimulation altered the tissue differentiation profile and prolonged the chondral phase of the endochondral ossification process [110, 140, 316].

rhBMP-2 can induce intramembranous or endochondral ossification, depending on various factors including anatomic location [97, 317]. Unlike the mechanical instability studies performed on bone fractures or non-critically sized osteotomies [109-111, 149], these segmental bone defects did not display exuberant external callus formation in either group. The compliant fixation plates, while allowing axial load transfer did not result in mechanical instability. However, we have found in a separate study that if the uniaxial constraint is removed, allowing multi-modal loading, these defects progress to nonunion as a result of instability [276]. With stable plates (either stiff or axially compliant), there appears to be more inconsistent formation of cartilage and a combination of intramembranous and endochondral bone formation, though the mechanical stimulus may increase or prolong endochondral ossification.

The interactions between rhBMP-2 and mechanical loading were not directly investigated in this study. Bmp-2 mRNA expression has been shown to increase in response to mechanical stimulation in vitro [232, 318], and the effects of rhBMP-2 delivery to non-critically sized fractures has been shown to be dependent upon mechanical conditions [319], however these interactions are not well understood, especially in large bone defects which require biologic treatment. In this model, empty and nanofiber mesh-only defects filled with fibrous tissue resulting in non-union; therefore, a group with loading but not rhBMP-2 was not included. However, unpublished preliminary data suggest that at lower doses of rhBMP-2 which do not induce bridging, an effect of loading is not apparent. Future work will address these potentially important interactions.

In addition to differences in tissue composition, there was a location-dependent response to functional loading, such that the proximal and defect regions experienced a significant increase in bone distribution as a result of loading, while the distal region was not affected. While a possible explanation is spatial inhomogeneity in the mechanical environment, there were no significant differences in principal strains between the proximal and distal ends (data not shown). Therefore, this location-dependence may have been caused by a less favorable vascular environment for progenitor differentiation at the distal end, which would provide fewer mechanosensitive cells to respond to the local mechanical stimulus.

Finite element modeling allowed back-calculation of the local material properties of tissue-engineered bone. This value (628.43 ± 54.47 MPa), is substantially lower than reported values for rat cortical bone, which are on the order of 10 GPa [313], however it is very similar to the reported tissue modulus of woven bone (approximately 600 MPa) [306]. While the boundary conditions were calculated based on femoral loads equal to the body weight, a sensitivity analysis assuming one order-of-magnitude error in boundary conditions yielded corresponding 10-fold differences in strain magnitude, but did not affect the strain distribution patterns presented. The flattening of the frequency distribution curve in the compliant plate group indicates that strains are distributed over more voxels, suggesting that these samples had adapted to more efficiently carry the applied loads. The observed alterations in tissue maturity suggest that the assumption of homogeneity of the bone tissue incurs some error, however, taking this into account, the greater amount of lamellar bone in the stiff plate group would tend to enhance these differences in strain distribution by including regions of increased tissue modulus.

This study also demonstrated that the FE method can be applied to non-destructively predict mechanical properties in segmental bone defect repair. This expands on the work of Reynolds and colleagues, who used microCT-generated structural parameters to predict biomechanical properties of allograft-treated segmental defects [320]. Though the current correlation study featured relatively small sample sizes, similar correlation coefficients to those reported by Reynolds et al. were found for structural parameters; however, FEA resulted in significantly improved prediction of mechanical properties due to inclusion of not only volume and distribution, but also geometry, connectivity, and tissue-level properties through the FE-derived apparent modulus. This approach allows researchers to evaluate mechanical properties of samples reserved for other end-point analyses, such as histology. Also, as clinical CT systems continue to improve in resolution, this approach may allow for noninvasive, longitudinal evaluation of functional regeneration in patients, where mechanical testing is clearly precluded.

One assumption made in the FE modeling was that mechanical loading did not alter the local elastic material properties. While the mean density was not affected by loading, load-mediated adaptive modeling did alter the microstructural maturity. This was assessed by comparison of collagen organization, which demonstrated that loading prolonged the presence of woven bone. This suggests potentially lower tissue-level material properties in the loaded samples compared to those with stiff plates, as it has been shown that lamellar bone has a higher tissue modulus than woven bone [306], and accentuates the observed differences in local strains and structural properties between groups. This load magnitude-dependent modulation of bone maturity has been observed

previously [306], and could be a result of increased or prolonged osteoblast activity or reduced osteoclast activity.

A limitation of the microCT-based approach is that only mineralized tissues can be evaluated. Therefore, the soft tissue inhomogeneities including cartilage and fibrous tissue were not included in the FE models or moment of inertia calculations, which modeled non-mineralized matrix as voids. However, at the time point of FE modeling, MOI analysis, and mechanical testing, week 12, the amount of cartilage in the defects was minimal and therefore not likely to dominate the behavior. Likewise, the differences in modulus between these soft tissues and bone further suggest that the mineralized matrix is likely the primary contributor to the structural properties. Similarly, the simple mechanics of materials analysis did not include the inhomogeneity of the tissue. However, this procedure was not performed to determine values, but rather to mathematically explain the experimental observations that an increase in average polar moment of inertia led to increases in stiffness, while the lack of change in minimum moment of inertia resulted in no differences in maximum torque. Therefore, despite the above simplifications, this analysis qualitatively explained these observations.

In conclusion, this study demonstrated that functional transfer of axial loads by modulation of fixation plate stiffness significantly alters BMP-mediated large bone defect repair by increasing bone formation and distribution and modulating tissue organization and differentiation. Consideration of the mechanical environment may therefore improve clinical treatment of challenging segmental bone defects as well as advance our understanding of the role of biomechanical factors in bone tissue differentiation, formation, and remodeling.

CHAPTER V: EFFECTS OF IN VIVO MECHANICAL LOADING ON VASCULAR GROWTH IN LARGE BONE DEFECT REGENERATION

ABSTRACT

Bone regeneration is a major challenge to orthopaedic surgeons, and poor vascularization is one of the primary factors limiting current treatment strategies for bone defect healing. We have previously demonstrated that in vivo mechanical loading enhances bone regeneration in a critically-sized rat femoral defect model; however, the effects of mechanical loading on neovascular growth in large bone defect repair have not yet been studied. Therefore, we evaluated the effects of early and delayed functional loading on vascular growth using axially compliant fixation plates which were electively actuated to allow ambulatory load transfer either at the time of implantation (early), or after 4 weeks of stiff fixation (delayed). Neovascular growth and bone regeneration were evaluated at week 3 following the onset of loading by contrast-enhanced microcomputed tomography and histology. Early loading significantly inhibited vascular invasion into the defect and reduced bone formation by 75% in comparison to stiff plate controls. Delayed loading, however, significantly enhanced bone formation by 20% and stimulated vascular remodeling by increasing vascular thickness and reducing the number of vessels less than 100 μm in diameter. Together, these data indicate that the early phase of bone defect healing is highly sensitive to the mechanical environment, and excessive interfragmentary motion can impair bone healing. However, under appropriate

conditions, mechanical loading can enhance bone defect repair by modulating vascular remodeling.

INTRODUCTION

Large bone defect regeneration is a major challenge in orthopaedic trauma and reconstruction, and poor vascularization is one of the primary factors limiting current treatment strategies for bone defect healing [15-16]. Structural allografts are often used to bridge the defects; however, there is a high post-surgery failure rate which is directly attributable to insufficient revascularization [15-16]. Bone is a highly vascularized tissue, and angiogenesis, the sprouting of new blood vessels, is essential to skeletal development and healing [15, 243-244]. These observations have stimulated great interest in developing treatments which induce both bone regeneration and neovascularization.

Similar to bone cells, which are highly mechanosensitive and coordinate to adaptively remodel bone matrix, endothelial cells and vascular networks respond dynamically to mechanical stimuli, including both fluid-induced shear stress and mechanical strain [3, 321-323]. However, the window of therapeutic effect has not yet been determined, and conflicting observations have been reported in vitro. For example, Mooney and colleagues demonstrated that 6% cyclic uniaxial strain increased endothelial cell tube formation and angiogenic growth factor secretion for cells cultured in two-dimensions (2D), while in 3D, 8% strain regulated the directionality of the neovascular networks, but diminished new branch formation [3-4]. Others have shown that mechanical stretch alters the orientation of 3D microvascular networks without significantly affecting endothelial sprouting [322-323]. Wilson et al. found disruption of

endothelial network formation but increased production of pro-angiogenic proteins in response to 2.5% strain [324]. These observations have led to an interest in the ability of mechanical conditions to modulate vascularized tissue regeneration.

In the context of bone healing, the effects of mechanical stimuli have been examined primarily in long bone fracture healing, in which fixation stiffness regulates the canonical healing patterns as a result of functional loading. In bone fractures, interfragmentary motion caused by non-rigid fixation stimulates endochondral ossification, while rigid fixation leads to intramembranous ossification [1, 105-106, 116]. Likewise, the timing of vascular ingrowth is also known to alter healing patterns, as early vascularization is associated with intramembranous ossification and delayed ingrowth with endochondral ossification [251]. Interfragmentary strains have been implicated as the driving force behind these tissue differentiation paradigms as a result of the homeostatic cellular response to maintain the capacity of the callus tissues to withstand the applied loads (i.e. Perren's Interfragmentary Strain Theory) [247]. However, another hypothesis is that mechanical disruption of vascular ingrowth initially drives avascular cartilaginous callus formation. Then, as the callus matures, interfragmentary motion is reduced, allowing initiation of vascular invasion and subsequent endochondral bone formation. Regardless of pathway, however, sufficient vascularization is essential for timely healing, and insufficient vascularization can lead to delayed healing or atrophic nonunion [248-249].

Specifically, several studies indicate that altering the local mechanical environment results in modified vascular ingrowth and consequent fracture healing, though results have been conflicting. Sarmiento et al. reported that moderate load transfer

enhanced vascular growth in bone fractures compared to rigid fixation [325] and Wallace et al. found increased corticomedullary blood flow in response to decreased fixation stiffness in the early stages of fracture healing but, after 6 weeks, observed a 50% decrease in periosteal callus perfusion [250]. In contrast, Lienau and colleagues demonstrated impaired vessel formation and reduced angiogenic gene expression under conditions of rotational and shear instability [149, 251]. Claes et al. also showed decreased vascular ingrowth and increased fibrocartilage formation in the presence of larger axial interfragmentary strains of 10 and 50% [117]. Together, these studies suggest a window of desired mechanical stimulus in which a moderate degree of loading is anabolic, but excessive loading may prevent vascular growth, with the timing of load application determining threshold magnitudes.

While critically-sized segmental bone defect repair may not follow the same canonical patterns found in fracture healing, vascularization may play an even more critical role given the larger size of the defect and associated nutrient diffusion limitations [16]. Mechanical stimulation may therefore be a potential point of intervention to enhance vascularized bone defect repair by influencing vascular network formation and subsequent mineralization. In Chapter IV, we reported that controlled load-bearing has the capacity to enhance bone regeneration in BMP-mediated large bone defect repair. However, the effects of mechanical loading on neovascularization of segmental defects have not yet been studied.

In this study, therefore, we examined the effects of loading on neovascular invasion and bone healing. Our overall hypothesis was that in vivo mechanical loading can modulate neovascular growth and bone formation. The timing of load application

may affect the response, however. Therefore, we evaluated the effects of both early (immediate actuation) and delayed loading (week 4 actuation) on vascular growth and bone formation. We hypothesized that early loading would disrupt nascent vessels, resulting in impaired bone regeneration, while delayed loading would stimulate vascular growth, consistent with the increased bone formation found in the previous bone regeneration experiment.

MATERIALS AND METHODS

Surgical Procedure

Bilateral, critically-sized (8 mm) bone defects were surgically created in femora of 13-week-old female SASCO Sprague-Dawley rats (Charles River, Wilmington, MA) as previously described [275-276]. Limbs were stabilized by either stiff fixation plates or compliant plates which allowed elective actuation of axial load sharing [276] (n = 10-12 per group). The stiff plates featured an axial stiffness of 214.3 ± 4.1 N/mm, while the compliant plates had a stiffness of 349.5 ± 35.1 N/mm and 8.4 ± 0.4 N/mm in the locked and actuated configurations, respectively [276]. Compliant fixation plates were actuated to allow ambulatory load transfer either at the time of initial implantation (early loading group) or at week 4 post-surgery (delayed loading group). Animals from each group received a compliant fixation plate and a contralateral stiff plate control. Animals in the delayed loading group received a secondary operation to actuate the compliant plates at week 4 post-surgery, while contralateral stiff plate controls were sham operated at the same time.

All defects were treated with recombinant human bone morphogenetic protein-2 (rhBMP-2), delivered in a hybrid nanofiber mesh/alginate-based delivery system [14]. Briefly, perforated nanofiber mesh tubes were created as described previously and were placed over the native bone ends, surrounding the defect [14]. 150 µl of alginate hydrogel containing the appropriate dose of rhBMP-2 was then injected into the defect space [14]. Defects in the early loading group and their contralateral controls received either 0.5 or 2.5 µg rhBMP-2. Defects in the delayed loading group and their stiff plate controls received 5.0 µg rhBMP-2, resulting in the 6 groups illustrated in Table 1. The doses were chosen based on the dose-response study described in Chapter III. In the early loading study, two doses were chosen: one which induces bone formation, but fails to induce consistent bridging of the defects (0.5 µg), and one which induces robust bone formation and consistent defect bridging by week 12, without over-saturating the response (2.5 µg). These doses were chosen to allow for either a positive or negative effect of loading on vascular growth. For the delayed loading study, we chose a dose (5.0 µg) which induced consistent bridging of the defects at week 4, the time point of compliant plate actuation. This dose also matched the previous mechanical loading study described in Chapter IV, allowing direct comparison. The 2.5 microgram dose was not used as it fails to induce consistent bridging of the defects by week 4 (bridging rate: 60%) (see Chapter III). The absence of bridging would drastically influence the amount of interfragmentary motion compared with bridged defects.

Table 5.1. Sample sizes for groups and analyses performed.

Experiment	Fixation Plate	BMP Dose	Time of Load Actuation	Sample Sizes for Analyses performed						
				Faxitron			MicroCT		Histology	
				Week 2	Week 4	Week 7	Week 3	Week 7	Week 3	Week 7
Early	Stiff	0.5	-	10	-	-	9	-	1	-
Early	Compliant	0.5	Day 0	9	-	-	8	-	1	-
Early	Stiff	2.5	-	9	-	-	8	-	1	-
Early	Compliant	2.5	Day 0	10	-	-	9	-	1	-
Delayed	Stiff	5.0	Sham Day 28	12	12	12	-	11	-	1
Delayed	Compliant	5.0	Day 28	11	11	11	-	10	-	1

Post-surgery, animals were given subcutaneous injections of buprenorphine every 8 hours, 0.04 mg/kg for the first 48 h and 0.013 mg/kg for the following 24 h. All procedures were approved by the Georgia Institute of Technology Institutional Animal Care and Use Committee (IACUC, protocol # A08032).

Alginate & Growth Factor Preparation

Recombinant human BMP-2 (R&D Systems, Minneapolis, MN) was reconstituted in 0.1% rat serum albumin in 4 mM HCl, according to manufacturer instructions. rhBMP-2 was then mixed with RGD (Arg-Gly-Asp) peptide-functionalized alginate [224, 277] to a final concentration of 2% alginate, which was crosslinked by mixing rapidly with 0.84% (m/v) $CaSO_4$. Each defect received 150 µl of the pre-gelled alginate with 0.5, 2.5, or 5.0 µg rhBMP-2, depending on group (Table 1).

Faxitron

Digital radiographs (Faxitron MX-20 Digital; Faxitron X-ray Corp., Wheeling, IL) were performed at an exposure time of 15 s and a voltage of 25 kV. Animals from the early loading groups (n =10 per group), which were euthanized at week 3, received X-ray imaging at week 2 post-surgery to evaluate bone formation, while animals from the delayed loading groups (n = 12 per group) were imaged at weeks 2, 4, and 7 post-surgery.

MicroCT Angiography

8-11 samples from each group (Table 1) were reserved for microcomputed tomography (microCT) angiography. Animals in the early loading groups were euthanized by CO_2 asphyxiation at week 3 post-surgery, while those from the delayed loading groups were euthanized at week 7 post-surgery (week 3 after compliant plate actuation). Radiopaque contrast agent-enhanced microCT angiography was performed using a protocol modified from Duvall et al. [326]. Briefly, a 2-inch 18-gauge catheter (SURFLO® Teflon I.V. Catheter, Terumo Medical, Somerset, NJ) was inserted into the left ventricle of the heart and advanced into the ascending aorta. The inferior vena cava was then severed, and 0.9% saline containing 0.4% (w/v) papaverin hydrochloride (Sigma-Aldrich, St. Louis, MO) was perfused through the vasculature using a peristaltic pump until complete clearance. The vasculature was fixed in an open configuration by perfusion with 10% neutral buffered formalin (NBF), which was then cleared with saline. Finally, 25 ml of polymerizable, lead chromate-based, radiopaque contrast agent (Microfil MV-122, Flow Tech; Carver, MA) was then injected using a 30 ml syringe.

The contrast agent was prepared according to manufacturer instructions, except the agent was diluted to a final concentration of 66% MV-122 to allow simultaneous segmentation of both newly-formed bone and vascular contrast agent. Samples were stored at 4°C for 24 hr to allow polymerization of the contrast agent. Hindlimbs were then excised and stored in 10% NBF for 1 week until preliminary microCT analysis.

MicroCT Analysis

MicroCT scans (VivaCT 40, Scanco Medical, Basserdorf, Switzerland) were performed at medium resolution with a 21.0 μm voxel size at a voltage of 55 kVp and a

current of 109 μA. Newly formed bone and contrast agent-filled vessels were segmented by application of a global threshold corresponding to 386 mg hydroxyapatite/cm^3, and a low-pass Gaussian filter (sigma = 1.2, support = 1) was used to suppress noise. Following initial microCT scanning to evaluate both new bone and perfused vessels, samples were transferred to a formic acid-based decalcifying agent (Cal-ExII, Fisher Scientific, Waltham, MA or Immunocal, Decal Chemical Co., Tallman, NY) for 2-3 weeks. Decalcified samples were then re-scanned using the same settings and in the same position as before to quantify vascular structures alone.

Two cylindrical volumes of interest (VOI) were contoured for analysis: a defect VOI (5 mm diameter x 6.3 mm length) and a total VOI (7 mm diameter x 6.3 mm length). The defect VOI encompassed only the nanofiber mesh and defect region, while the total VOI included the defect and surrounding soft tissues. The position of the VOIs in the pre- and post-decalcification scans was confirmed by position relative to the fixation plate, which did not change by decalcification. For pre-decalcification analysis, the volume of all attenuating tissues, including bone and contrast agent-filled vasculature was computed. After decalcification, the vascular volume, connectivity, thickness, thickness frequency distribution, number, spacing, and degree of anisotropy were analyzed as described previously [326]. The bone volume in the defect was then computed by subtraction of the vascular volume from the bone-plus-vessel volume in the total VOI. The vascular morphology was compared between the proximal and distal ends of the defects by separately analyzing each half of the defect VOI (5 mm diameter x 3.15 mm length) in the stiff plate groups.

Histology

One representative sample per group was chosen for histology based on qualitative Faxitron evaluation of bone growth. Samples were fixed in 10% NBF for 48 hours at 4ºC and then decalcified over 2 weeks under mild agitation on a rocker plate. Following paraffin processing, 5 μm-thick mid-saggital sections were cut and stained with Haematoxylin and Eosin (H&E) and Safranin-O/Fast-green [278].

Statistical Analyses

All data are presented as mean ± standard error of the mean (SEM). Differences between groups, accounting for animal variability, were assessed by analysis of variance (ANOVA) with pairwise comparisons made by Tukey's post hoc analysis. A p-value < 0.05 was considered significant. Minitab® 15 (Minitab Inc., State College, PA) was used to perform the statistical analysis.

RESULTS

The creation of a bone defect results in a rapid and extensive angiogenic response in the surrounding tissues, with collateral vessel formation and growth of blood vessels toward the site of injury (Figure 5.1). This study evaluated the ability of early and delayed mechanical loading to modulate the growth and remodeling of these vessels.

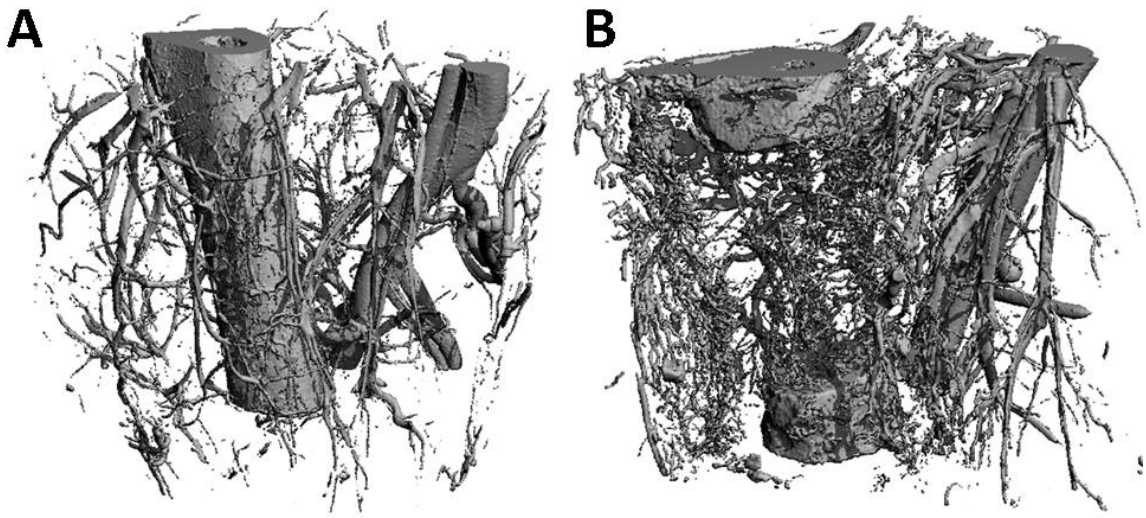

Figure 5.1. Vascular response to bone injury: angiogenesis and collateral vessel formation. (A): MicroCT image of age-matched unoperated femur with surrounding vasculature. (B): Bone and vascular structures 3 weeks following creation of an 8 mm bone defect.

Early Loading: Vascular Growth

Vascular structures in the early loading groups at week 3 post-surgery were quantitatively analyzed within the defect VOI and the total VOI to include both the defect and the surrounding soft tissues (Figure 5.2A). There were no differences in the vascular volume (Figure 5.2B) or connectivity (Figure 5.2D) between groups for the total VOI; however, within the defect VOI, in the presence of early loading, vascular volume (Figure 5.2C) and connectivity (Figure 5.2E) were significantly lower by 66% and 91%, respectively, for the 2.5 µg rhBMP-2 dose. Similar trends were found for the 0.5 µg dose, though these differences did not reach statistical significance ($p = 0.56$ and 0.16 for vascular volume and connectivity, respectively). Other morphometric parameters including vascular thickness, separation, number and degree of anisotropy were not significantly altered by loading at either dose for both the total VOI and defect VOI (data not shown).

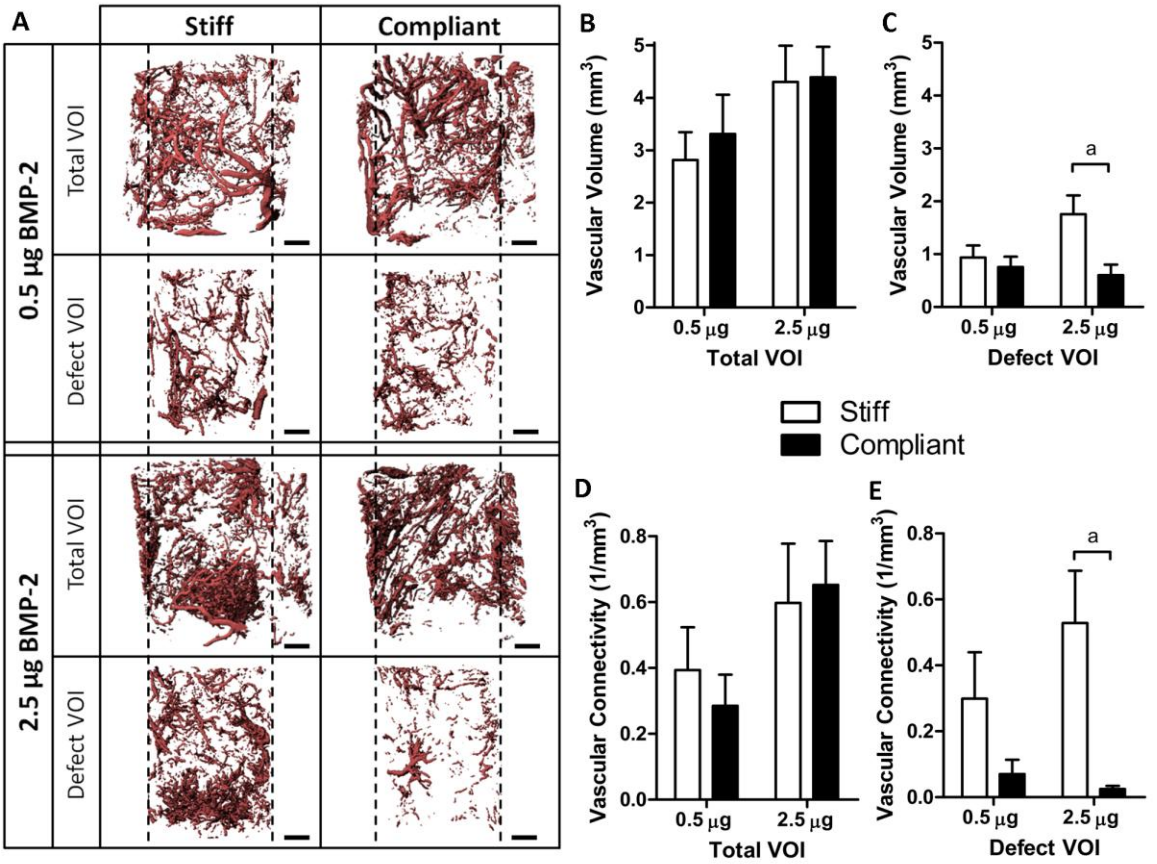

Figure 5.2. MicroCT angiography of early loading groups. (A): Representative 3D reconstructions of vascular structures in the total VOI (7mm Ø) and defect VOI (5 mm Ø) for each dose and fixation plate type. Scale bars: 1mm. (B, C): Vascular volume in total VOI and defect VOI, respectively. (D, E): Vascular connectivity in the total VOI and defect VOI, respectively. a: $p < 0.05$.

rhBMP-2 dose was a significant predictor in the ANOVA for both vascular volume and connectivity in Figure 5.2, and within the total VOI, there were no differences between the stiff and compliant plate groups. Therefore, to assess the BMP-mediated vascular response to injury, the stiff and compliant plate groups were pooled based on rhBMP-2 dose and compared to age-matched unoperated control limbs (n = 12; Figure 5.3). The increased dose of rhBMP-2 significantly enhanced vascular network formation. Also, the newly formed vascular networks differed significantly from native architecture. The BMP-mediated angiogenic response to injury resulted in increased

vascular volume, connectivity, and thickness compared to unoperated controls (Figure 5.3B-D); however, while native vessels exhibited transverse isotropy with preferential alignment along the longitudinal axis, the newly formed vascular networks were significantly more isotropic (Figure 5.3E).

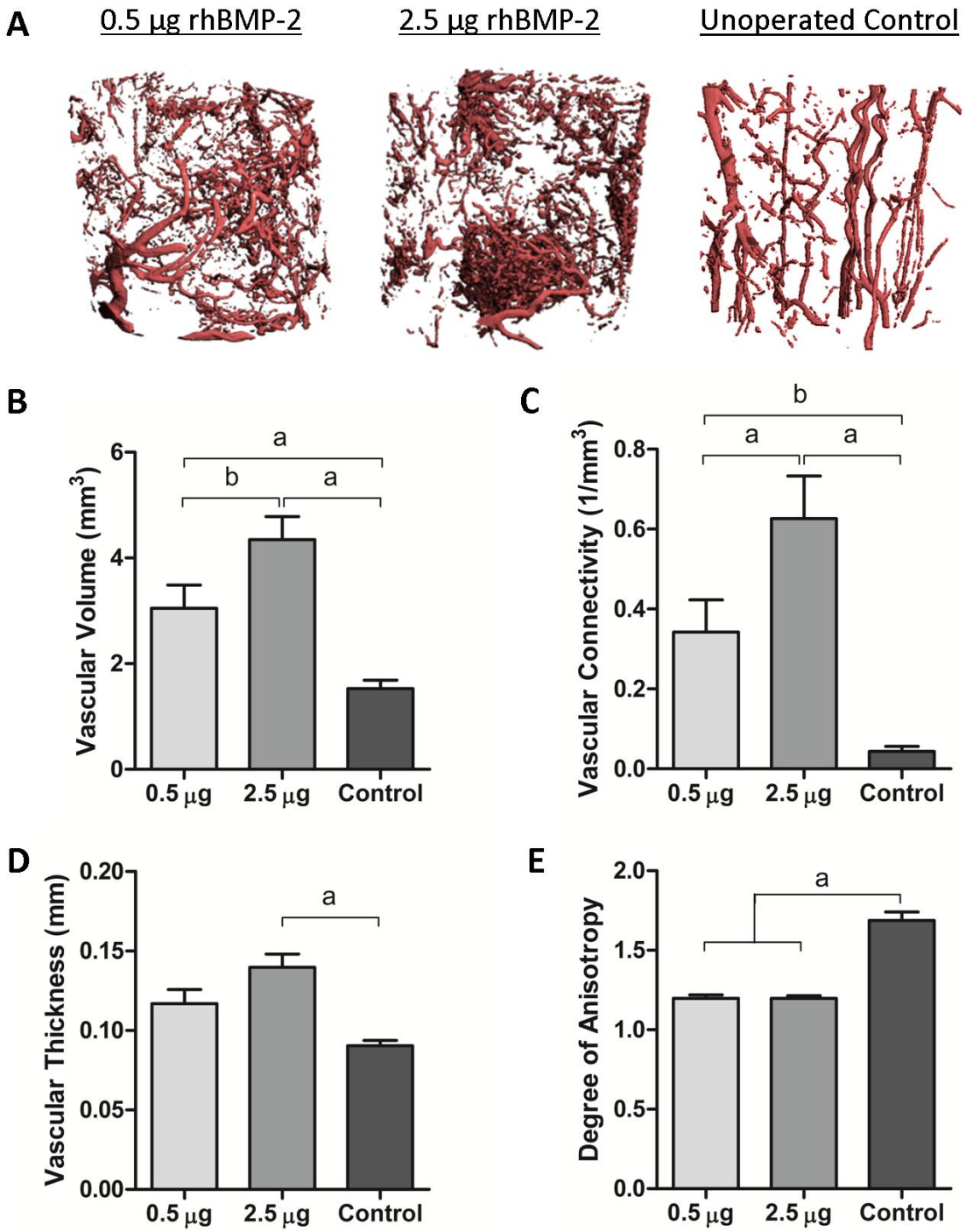

Figure 5.3. BMP-mediated vascular response to bone injury. (A): Representative total VOI images of pooled stiff & compliant plate groups at each dose and age-matched unoperated controls. (B): Vascular volume. (C): Vascular connectivity. (D): Vascular Thickness. (E): Degree of anisotropy. a: $p < 0.05$; b: $p < 0.053$.

The spatial distribution of blood vessels in the stiff plate groups was analyzed by comparing proximal and distal volumes of interest within the defect VOI (Figure 5.4A). The vessel volume, connectivity, and thickness were significantly greater at the proximal end of the defects than at the distal end (Figure 5.4B-D, respectively).

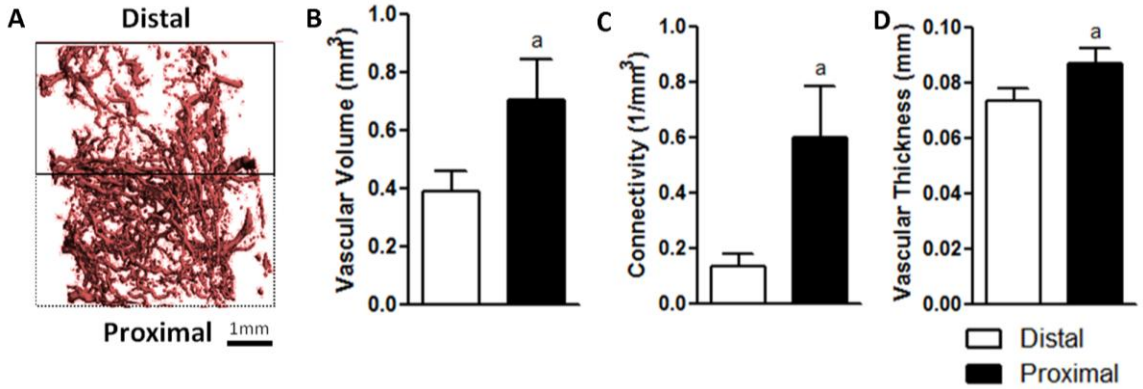

Figure 5.4. Spatial inhomogeneity of vessel distribution in the defect VOI of the stiff plate group. (A): Representative perfused image showing proximal and distal regions of the defect. (B-D): Vascular volume (B), vascular connectivity (C), and vascular thickness (D) in the distal and proximal regions. a: $p < 0.05$ vs. distal region.

Early Loading: Bone Formation

Bone formation within the defect responded to early loading in a similar manner to vascular growth (Figure 5.5). Qualitative evaluation of bone formation at week 2 post-surgery was performed by digital radiography, illustrating reduced bone formation in the compliant plate group at the 2.5 µg dose (Figure 5.5A). MicroCT reconstructions of undecalcified perfused samples allowed simultaneous visualization of bone formation and vasculature at week 3 and confirmed the radiographic observations (Figure 5.5B). Following subtraction of the vascular volume in the defect, microCT quantification revealed a significant 75% decrease in bone volume in the compliant plate group compared to the stiff plate group at the 2.5 µg rhBMP-2 dose (Figure 5.5C). Differences in bone volume at the 0.5 µg dose were not significant ($p = 0.09$).

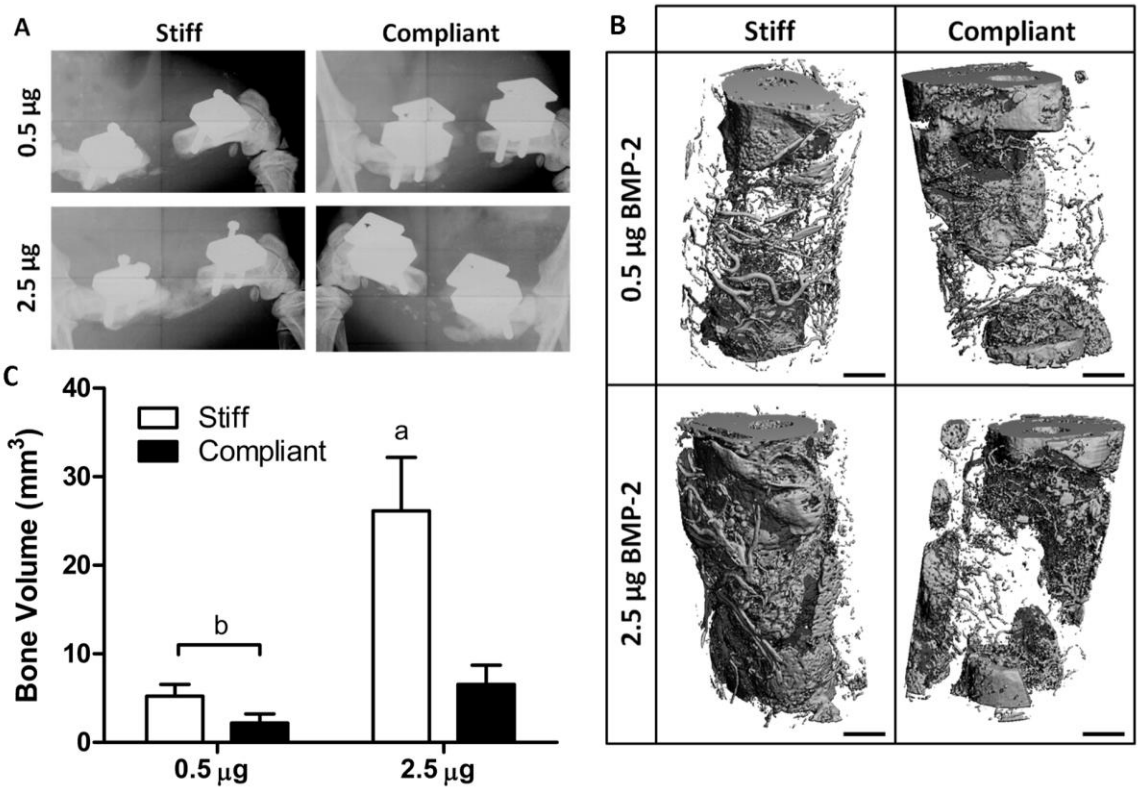

Figure 5.5. Digital X-ray and microCT evaluation of bone formation in early loading groups. (A): Radiographs of limbs at week 2 post-surgery. (B): MicroCT reconstructions of undecalcified, perfused samples at week 3 post-surgery showing both bone formation and vascular growth. Scale bars: 1mm. (C): Quantification of bone volume alone. a: $p < 0.05$ vs. all other groups; b: $p = 0.09$.

Early Loading: Histology

The high eosinophilicity of erythrocytes allowed identification of blood vessels in H&E stained sections (Figure 5.6). Vessel size and area density qualitatively correlated with microCT angiography (Figure 5.7A). In representative samples analyzed for histology, the stiff plate groups demonstrated qualitatively more and larger blood vessels than the compliant plate groups.

Safranin-O staining demonstrated that early loading altered tissue-biomaterial interactions (Figure 5.7B). In the stiff plate groups, formation of connective and mineralized tissues were well-integrated with alginate islands; however, in the loaded groups, the predominantly soft tissues that populated the defect failed to adhere to the alginate gel, resulting in void formation around the biomaterial.

The presence of cartilage and endochondral bone formation was also evident in all four groups; however, the metabolic activity of the chondrocytes appeared to be altered by the mechanical environment (Figure 5.7C). Chondrocytes were present in both stiff and compliant plate groups, but the dark red staining of GAGs was more evident in the compliant plate groups. Likewise, the amount of cartilage formation was also qualitatively greater in the compliant plate groups.

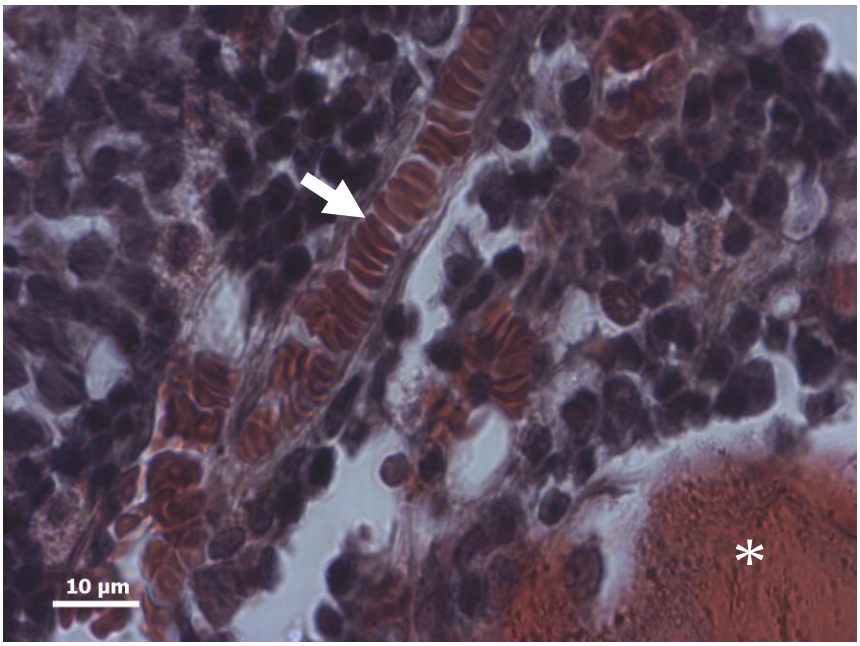

Figure 5.6. 63x magnification image of H&E-stained section showing erythrocytes (white arrow) inside a capillary. * indicates bone formation.

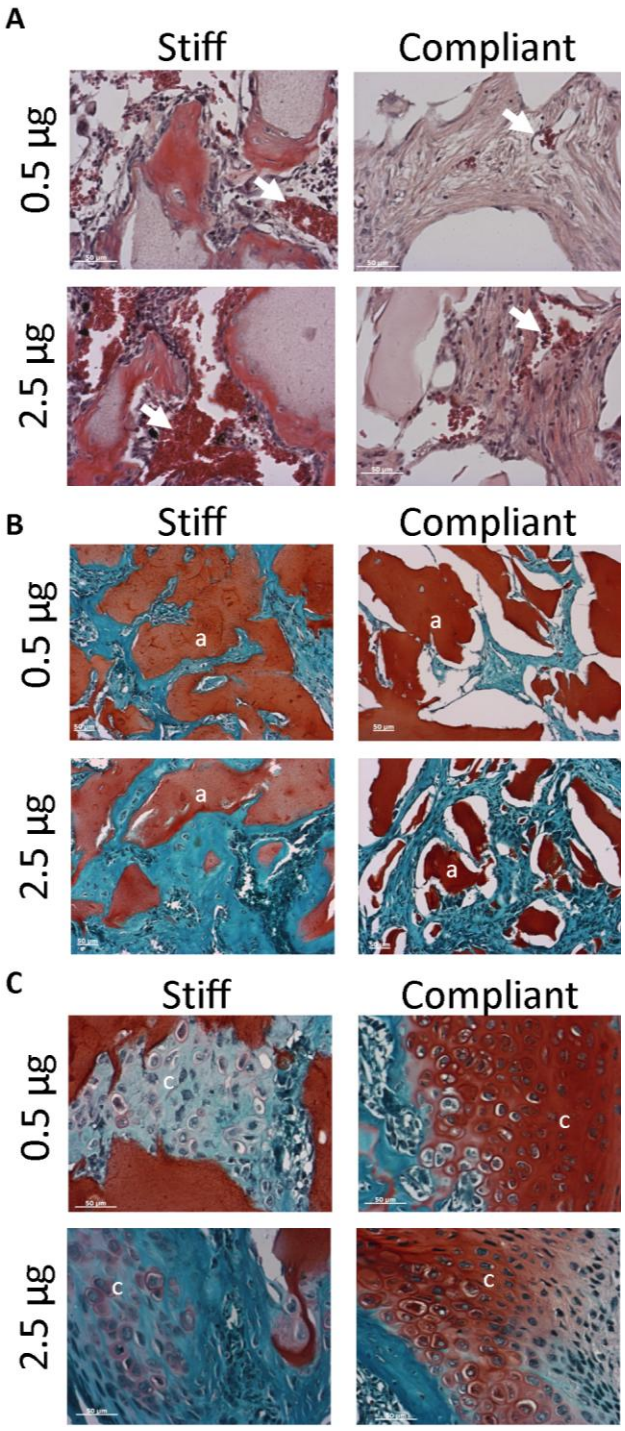

Figure 5.7. Week 3 histological staining of saggital sections of early loading groups. (A): Haematoxylin and Eosin-stained sections allowed identification of blood vessels by dark staining of erythrocytes (white arrows). Images at 20x. (B): Safranin-O/fast green-stained sections illustrating disruption of alginate (a) integration with surrounding tissues (green). Images at 10x. (C): Safranin-O/fast green-stained sections illustrating cartilage (c) and endochondral bone formation. Images at 20x. All scale bars: 50 µm.

Delayed Loading: Vascular Growth

Vascular structures in the delayed loading groups at week7 were quantitatively analyzed both within the defect and total VOIs (Figure 5.8). There were no differences in vascular volume between the stiff and compliant plate groups for either total or defect VOI (Figure 5.8B); however, vascular connectivity (Figure 5.8C) and vascular number (Figure 5.8D) were significantly lower in the compliant plate group for both total and defect VOIs. While differences in vascular thickness did not reach significance in the defect VOI ($p = 0.08$), the compliant plate group had a significantly greater vascular thickness in the total VOI (Figure 5.8E). In the defect VOI, the frequency distribution indicated a significantly lower number of small vessel bins (40-100μm in diameter; Figure 5.8F) and an extension of large diameter bins (315 – 441 μm in diameter; Figure 5.8F, inset) in the compliant plate group.

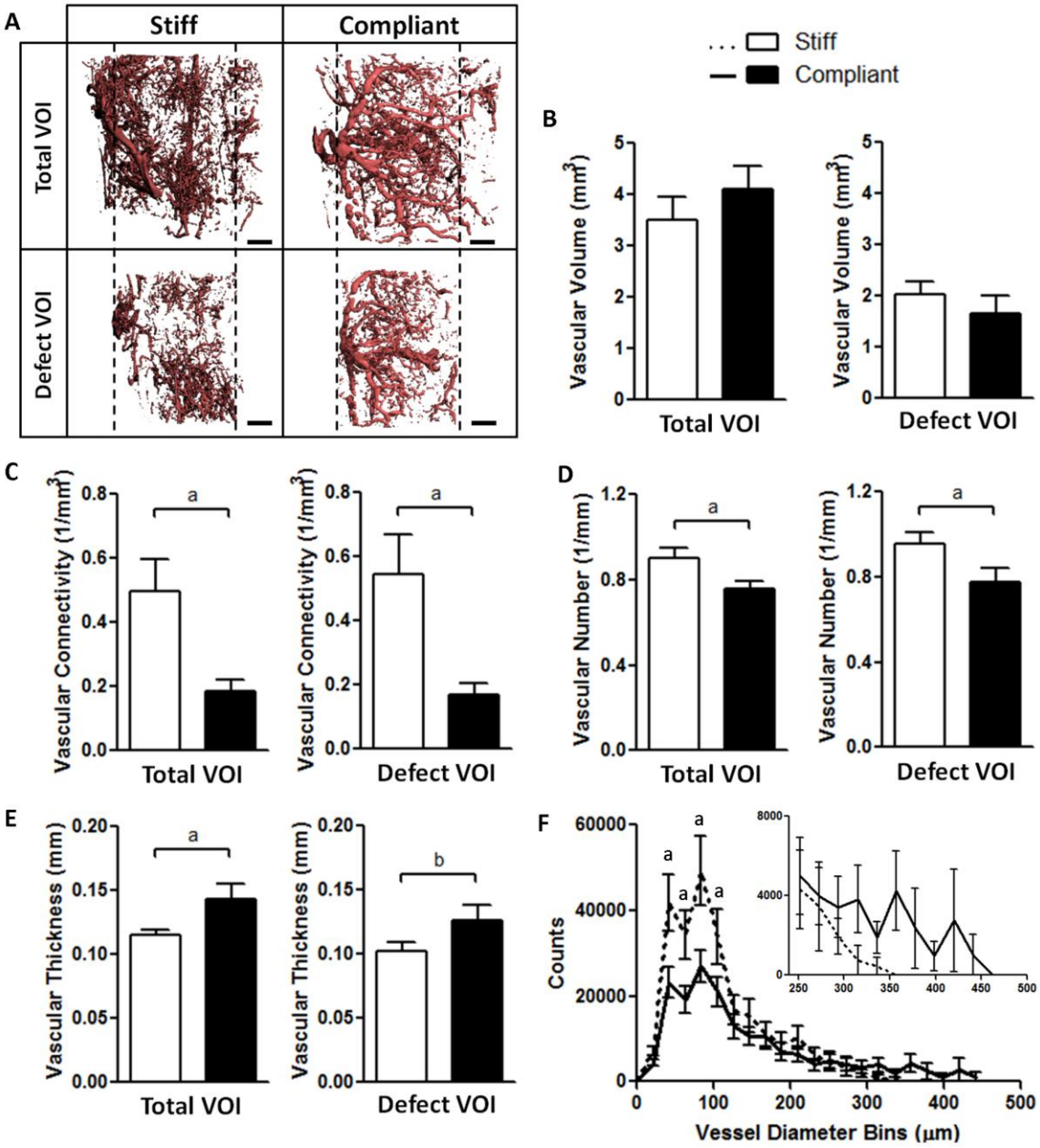

Figure 5.8. MicroCT angiography of delayed loading groups. (A): Representative 3D reconstructions of vascular structures in the total VOI (7mm Ø) and defect VOI (5 mm Ø) for both fixation plate types. Scale bars: 1mm. (B-E): Vascular morphology parameters in the total and defect VOIs: vascular volume (B), vascular connectivity (C), vascular number (D), and vascular thickness (E). (F): Vascular thickness histogram indicating blood vessel size distribution. Inset: magnification of 252 - 462 μm bins. a: $p < 0.05$; b: $p = 0.08$.

Delayed Loading: Bone Formation

Unlike early loading, delayed mechanical loading enhanced bone formation (Figure 5.9). Digital radiography revealed that all defects had bridged with bone prior to plate actuation at week 4, and at this time the stiff and compliant plate groups featured qualitatively similar bone formation. At week 7, however, after 3 weeks of loading, there was qualitatively more bone formation in the compliant plate group (Figure 5.9A). Post-mortem microCT analysis allowed reconstruction of the combined bone and vascular structures (Figure 5.9B) and, following subtraction of vascular volumes, revealed a significant 20% greater bone volume in the compliant plate group at week 7 (Figure 5.9C).

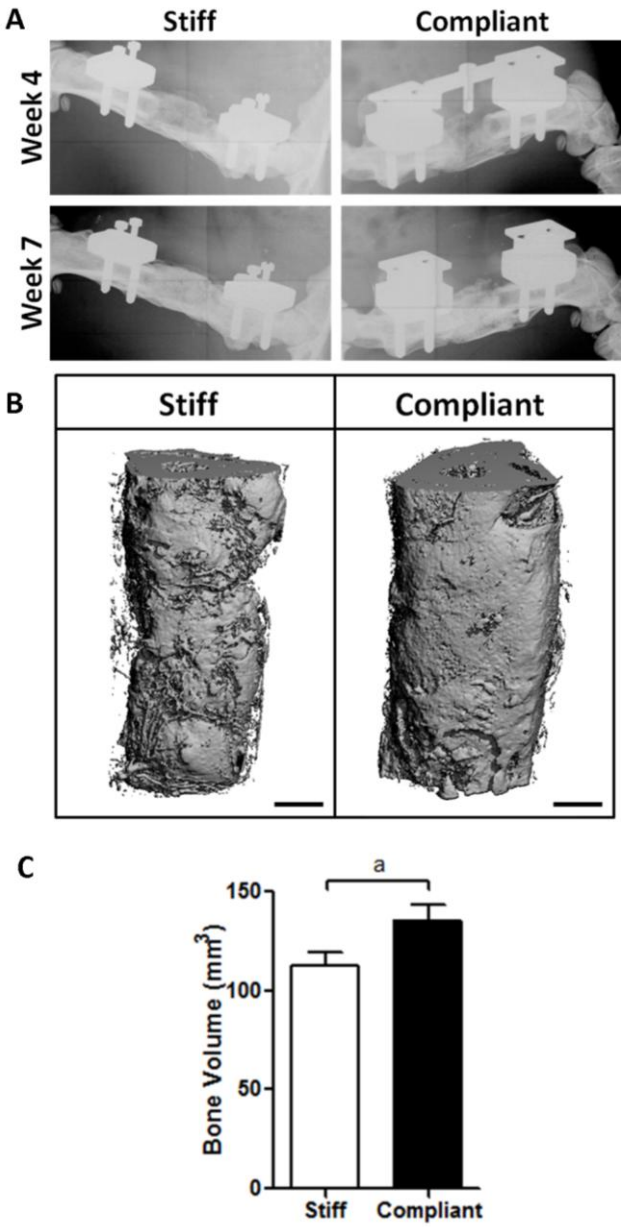

Figure 5.9. Digital X-ray and microCT evaluation of bone formation in delayed loading groups. (A): Radiographs of limbs at weeks 4 and 7 post-surgery. (B): MicroCT reconstructions of undecalcified, perfused samples at week 7 post-surgery showing both bone formation and vascular growth. Scale bars: 1 mm. (C): Quantification of bone volume alone. a: $p < 0.05$.

Delayed Loading: Histology

Histological staining at week 7 revealed substantial osteocyte-populated woven bone formation and strong integration of new bone formation with regions of alginate gel

(Figure 5.10A, B). Individual hypertrophic chondrocytes and small remnants of endochondral bone formation were evident in both groups (Figure 5.10C).

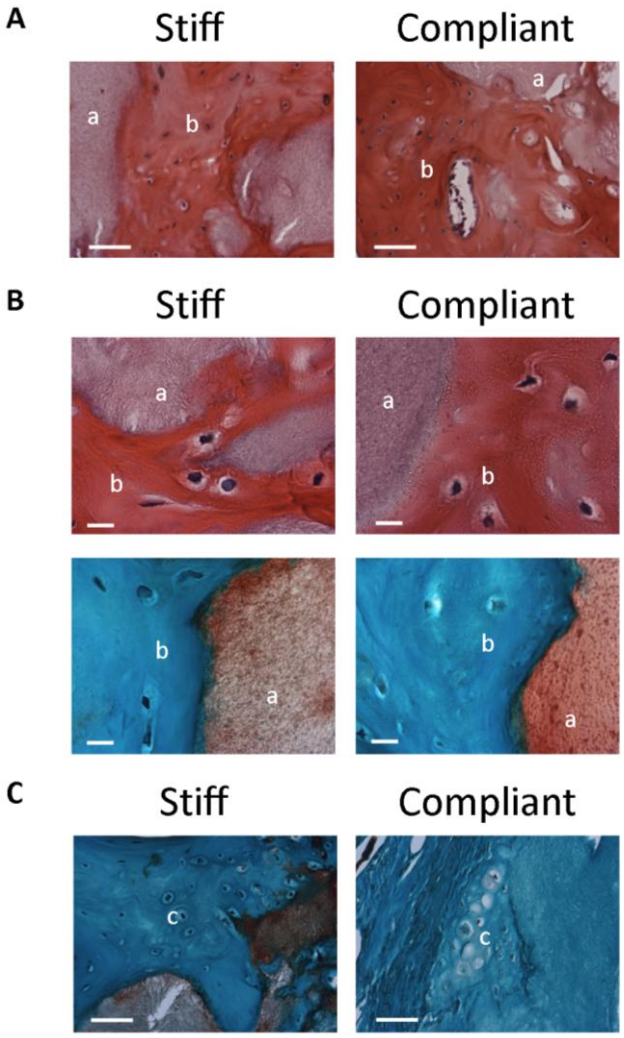

Figure 5.10. Week 7 histological staining of saggital sections of delayed loading groups. (A): H&E-stained sections illustrate bone formation (b) and regions of alginate (a). Images at 20x; scale bars: 50 µm. (B): H&E (top) and Safranin-O/fast green (bottom)-stained sections illustrating bone & alginate integration. Images at 63x; scale bars: 10 µm. (C): Safranin-O/fast green-stained sections illustrating remnants of cartilage (c) and endochondral bone formation. Images at 20x; scale bars: 50 µm.

DISCUSSION

This study investigated the effects of in vivo mechanical loading on neovascularization and bone formation in critically-sized bone defect regeneration.

Previously published reports indicate that mechanical conditions in the initial phase of bone fracture healing direct and determine the repair process [109]. We have also shown in Chapter IV that in large bone defects, delayed loading enhances bone regeneration. In this study, we evaluated the effects of both early and delayed mechanical loading on vascular growth and bone regeneration.

Early Loading

In the presence of early loading, the vascular supply in the defect was drastically reduced compared to stiff plate controls, but the overall angiogenic response to injury was not altered: the vessel volume and connectivity in the total VOI were not affected, suggesting that loading had a localized effect that inhibited ingrowth of vessels into the defect. These inhibitory effects were likely due to excessive interfragmentary motion associated with loading prior to defect stabilization by bone formation. In native bone tissue, matrix strains typically reach 0.3% [327]; however, under the loading conditions determined for this model (see Chapter IV), early loading resulted in initial axial interfragmentary strains of 5-10%, assuming negligible contribution of the mesh/alginate construct to defect stability. It was these relatively large initial strains that likely inhibited blood vessel ingrowth and bone formation in the compliant plate groups. In addition to disrupting vascular invasion, and inhibiting bone formation, early deformations within the defect may have promoted tissue differentiation toward more fibrotic and cartilaginous tissue types, which are inherently less vascularized. This second explanation has been proposed by Perren and Carter and colleagues to explain the effects of loading on bone fracture callus differentiation [146, 247]. In this model, mechanical loading

stimulates tissue formation and differentiation and vessels form and remodel to support the new tissues.

Qualitative differences in cartilage metabolic activity were observed as a result of early loading. Though cartilage was present in all groups at week 3 post-surgery, loading appeared to increase or prolong GAG production, as indicated by the intensity of Safranin-O staining. This is consistent with our prior observations in Chapter IV and previous reports in the literature that mechanical loading prolongs the chondral phase of endochondral ossification in defect healing [110]. In Chapter IV, we also observed spatial variations in cartilage formation and response to loading between proximal and distal ends of the defects. We hypothesized that these differences were to due to proximal-distal inhomogeneity of the vascular distribution, with reduced vascular supply at the distal end of the defects. Our current study confirmed this hypothesis, showing a significantly lower vascular volume, connectivity and thickness at the distal end of the defects compared to the proximal end. The reason for this spatial variation in vascular invasion may be attributed to the greater surrounding soft tissue coverage at the proximal end.

In this study, two different doses of rhBMP-2 were evaluated: a non-bridging dose (0.5 μg) and a dose which induces consistent defect bridging by week 12 (2.5 μg) (see Chapter III). The lower dose was insufficient to induce robust bone formation over the time course studied, and did not yield significant differences as a result of loading. However, mechanical loading drastically effected both vascular growth and bone formation at 2.5 μg. Independent of loading conditions, vascular growth responded in a dose-dependent manner to rhBMP-2 by week 3. The mechanisms by which BMP-2 may induce vascular growth remain unclear, but reports of direct angiogenic effects on

endothelial cells [328-329] and paracrine upregulation of VEGF expression in osteoblasts [330] have been reported. Overall, the vascular response to injury resulted in networks with greater volume, connectivity and isotropy than native un-injured tissue.

Delayed Loading

Delayed mechanical loading significantly enhanced bone formation, consistent with our previous findings in Chapter IV. Unlike early loading, it also allowed growth of blood vessels into the defect, as evidenced by the equivalent vascular volume in both the stiff and compliant plate groups. Delayed loading reduced vascular number and connectivity and increased vessel thickness, with a reduction in the number of small vessels (40 - 100 μm in diameter) and an expansion of large vessels (315 – 441 μm in diameter) in the compliant plate group relative to stiff plate controls. This suggests loading may have induced vascular remodeling to maintain defect perfusion and vascular volume by increasing vessel size and pruning small vessels that were no longer necessary, though vascular rarefaction was not directly measured. Together, these data suggest that delayed mechanical loading may have stimulated vascular remodeling through arteriogenesis, the growth and dilation of existing arterioles by proliferation of endothelial and smooth muscle cells [331]. This is contrary to our hypothesis that delayed mechanical loading would stimulate angiogenesis and growth of new vessels; however, these results are consistent with previous observations of vascular remodeling in rodent models of hindlimb ischemia, which have shown that while angiogenesis is governed primarily by tissue ischemia, arteriogenesis is likely regulated by biomechanical factors including luminal shear and vessel strain [242, 326, 332]. Similarly, Cao et al. demonstrated that the transition between maintenance and regression of new vessels is

dependent on exposure to growth factors at the time of vessel birth, and these same factors, PDGF, FGF, VEGF, are regulated by mechanical conditions [4, 333-336]. Thus, delayed mechanical loading may have accelerated the maturation and remodeling of new vessels, enhancing bone formation and limb regeneration.

The results of this study indicate that neovascular network formation and growth may be regulated by mechanical conditions in vivo, and extravascular matrix deformations may alter vessel formation and remodeling to regulate engineered tissue regeneration. These data also suggest that the timing and magnitude of loading are important variables that warrant further research to determine a window of therapeutic effect. Recently, Kilarski et al. demonstrated that endogenous fibroblasts and myofibroblasts recruited during wound healing exert tensile stresses that regulate nonangiogenic expansion of blood vessels into fibrinogen/collagen scaffolds implanted onto chick chorioallantoic membranes [337]. In that study, however, mechanical conditions were neither measured nor directly controlled. The present study demonstrates for the first time that in vivo biomechanical stimulation may further enhance vascularization of engineered tissues.

These experiments cannot uncouple the effects of mechanical forces on vascular growth and tissue formation and differentiation. Osteogenesis and angiogenesis are linked on a molecular level, and it is not possible to induce bone formation without vascular ingrowth [15]. In growth plate development, for example, expression of angiogenic factors precedes vessel formation, chondrocyte hypertrophy, and ultimately bone formation [5]. Regulation of the genes and signaling molecules important for the genesis of cartilage, bone, and vasculature, such as Indian Hedgehog (Ihh), Runx2, and

VEGF, respectively, are shared such that knock-out animals lacking any of these three genes experience defects in each of the three tissues, suggesting a fundamental link between tissue formation and vascular growth [5].

Delayed loading may have induced remodeling simply by disrupting small vessel formation, which in turn reduced connectivity and vascular number, without disrupting the larger vessels that had developed prior to the onset of loading, allowing sufficient vascular supply for bone formation. However, the observed enhancements in bone formation suggest an increased vascular demand, requiring an improved functional network. Reports in the literature that mechanical loading primarily alters vascular remodeling over angiogenesis in various bioreactor systems corroborate this hypothesis [3, 322-323, 338]. Likewise, beneficial effects of loading on vascular growth have been observed in the bone fracture healing literature [29-30]. Further research is required to determine whether matrix deformations directly enhanced vascular network remodeling and arteriogenesis or merely disrupted new vessel formation. Such studies may have implications for the engineering of vascularized tissues both in the context of bone repair and in general.

Histological analysis revealed close integration of the alginate and newly formed bone, and consistent with previous observations, the mechanical environment may have regulated the progression of endochondral bone formation and cartilage hypertrophy [110]. These observations suggest that the mechanical environment is an important regulator of tissue formation and differentiation in large bone defect repair.

There are several limitations of the methodology employed in these experiments. The microCT angiography technique is an end-point measure, which requires

decalcification of the bone, precluding longitudinal evaluations and biomechanical testing of the limbs for functional assessment. Thus, the time points for analysis must be chosen carefully, and the effects of treatment on restoration of biomechanical function must be performed separately (see Chapter IV). In this study, vascular structures were analyzed 3 weeks after load initiation. This was chosen to provide sufficient time for vascular growth and remodeling in response to loading while perhaps capturing transient effects as well. Another potential limitation of this method is that the bone volume was not computed directly; however, care was taken register placement of the contours relative to the fixation plates to maintain a constant volume of interest for each scan. Finally, as discussed in detail by Duvall et al., the scan resolution chosen may affect the size of vessels capable of being detected and segmented [326]. Although there are great advantages for quantitative three-dimensional analysis off vascular structures using microCT, the formation and distribution of small capillaries on the order of 10 μm in diameter could not be evaluated using this methodology.

Conclusions

These studies evaluated the effects of early and delayed mechanical loading on neovascular growth and remodeling and bone formation in large bone defects. Under early mechanical loading, vascular growth was reduced and bone formation mitigated in comparison to stiff plate controls. However, in the presence of loading delayed until after defect bridging, the loaded group featured vascular network remodeling and enhanced bone regeneration compared to controls. Together, these data demonstrate the mechanosensitivity of vascularized tissue regeneration vivo and highlight the potential for mechanical stimulation to modulate post-natal vascular growth and remodeling.

CHAPTER VI: SUMMARY AND FUTURE DIRECTIONS

OVERALL SUMMARY

While large bone defects remain a critical challenge in orthopaedic surgery, tissue engineering has emerged as a promising treatment strategy. One approach to tissue engineering, termed endogenous repair, aims to stimulate the body's natural regenerative potential to restore tissue structure and function. The studies described in this thesis manipulated both the biochemical and biomechanical environments to initiate and sustain these regenerative cascades. One of the most successful applications of tissue engineering to date is the delivery of osteoinductive growth factors, such as members of the bone morphogenetic protein family [165]. The clinical delivery method for these proteins, however, is inefficient as large doses are required, contributing to prohibitively high costs and potential complications due to protein diffusion [182]. Chapter III therefore characterized and evaluated a biomaterial delivery system that provides a sustained growth factor release profile to enhance performance and reduce the necessary effective dose. The influence of the biomechanical environment was then quantitatively evaluated using this model.

As a dynamically adaptive, load bearing tissue, bone is highly responsive to its mechanical environment. As has been demonstrated in bone fracture healing, modulation of biomechanical conditions may enhance bone healing and neovascular growth [250, 325]. These experimental observations have led to drastic changes in the clinical approach to fracture fixation [107]; however, the potential for functional loading to enhance the regeneration of large bone defects had not been evaluated. The governing hypothesis of this work was that in vivo mechanical loading can enhance bone

regeneration and vascular growth in large bone defects treated with sustained delivery of rhBMP-2.

This hypothesis was tested using a rat segmental bone defect model using a variety of experimental and computational techniques. Bone formation was evaluated longitudinally using digital radiography and microcomputed tomography, while functional restoration was quantified by torsional biomechanical testing and microCT image-based finite element modeling. Tissue morphology and composition were assessed by histological stains including Haematoxylin and Eosin, Safranin-O, and Picrosirius red. Finally, vascular growth was observed by histology and quantified by microCT angiography.

RHBMP-2 DELIVERY

Local rhBMP-2 delivery has proven a successful treatment strategy for spinal fusions and compound tibial fractures in the clinic, and has been demonstrated to stimulate functional repair of large bone defects in numerous animal models. However, minimizing the clinically reported side effects and high costs associated with current growth factor delivery systems remains challenging. Implementation of biomaterial delivery strategies that reduce the necessary effective dose would ameliorate these limitations and improve the clinical treatment of large bone defects.

The study described in chapter III characterized and evaluated a hydrogel-based protein delivery system recently established in our laboratory. These experiments quantified the rhBMP-2 dose-response relationships and temporal release properties of this delivery system in comparison to the clinically used collagen sponge and demonstrated that the mesh/alginate delivery system improved bone formation over

current rhBMP-2 delivery methods. This highlights the importance of quantification of release kinetics and scaffold degradation properties for evaluating novel recombinant protein carriers.

The largest dose evaluated in this study, 5 μg, has been shown in the mesh/alginate system to yield mechanical properties which exceed or are not significantly different from intact age-matched bone properties. In fact, we performed a pilot study in which the fixation plate was removed at week 22 post-surgery, and the animal continued to ambulate normally for another 8 weeks without incident. These observations demonstrate the functional efficacy of this protein/delivery system combination.

One potential limitation of the alginate-based delivery system is that while the degree of alginate fragmentation increased with increasing protein dose, the gel did not completely degrade over the time course of the study. Indeed, in the plate-removal pilot study, in which histological analysis was delayed until week 30 post-surgery, residual alginate remained in the defect, despite uniform remodeling of the new bone to a lamellar microstructure (Figure 6.1). Some amount of marrow reconstitution was evident; however, substantial amounts of alginate gel were also present and encompassed by trabecular-like lamellar bone.

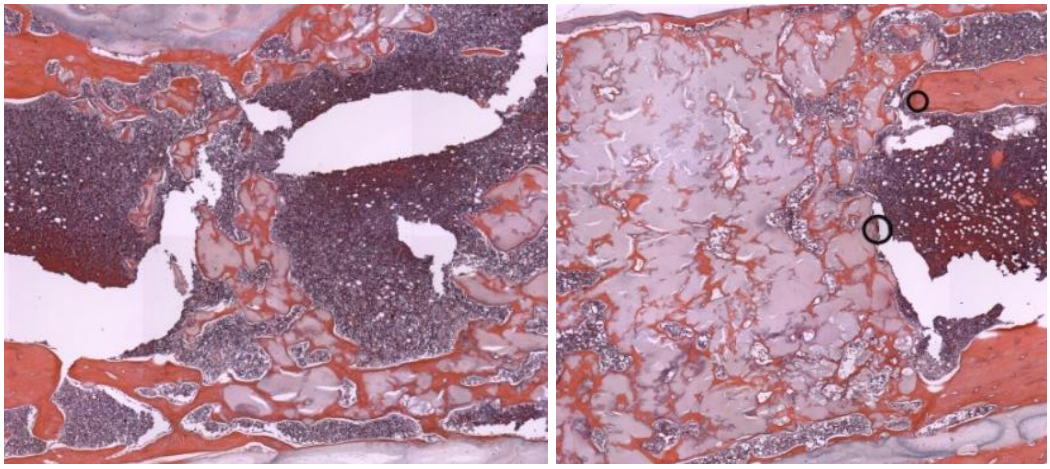

Figure 6.1. H&E stained section of segmental defect at week 30 post-surgery. The fixation plate was removed at week 24, allowing 8 weeks of normal ambulation on the regenerated bone. Some amount of marrow reconstitution was evident (dark region at left center of defect); however, alginate gel (pink) was also present and encompassed by trabecular-like lamellar bone (red). Images at 4x.

Despite 8 weeks of full weight-bearing after the completion of bone formation, the bone did not remodel to a native cortical architecture. Similarly, allowing load transfer during the stage of active bone formation but after defect bridging as demonstrated in Chapter IV also failed to restore cortical bone architecture. One explanation is that the residual alginate hydrogel may have interfered with the remodeling process, preventing cortical bone restoration. This is corroborated by comparison of the current study with a previous study in which the volume of alginate delivered to the defect was 150 µl. In the current dose-response study, the volume of alginate was 200 µl with the goal of limiting the error in the dose delivered due to over- or under-injecting. This however, resulted in a higher volume of residual alginate at week 12 and a significantly lower maximum torque at failure in the 200 µl defects. It is therefore hypothesized that residual alginate may interfere with mechanical integration, suggesting that minimizing residual alginate volume and increasing the degradation kinetics may further enhance functional restoration.

Future work will therefore aim to develop improved hydrogel delivery systems that feature sustained delivery, but will degrade rapidly following protein release to facilitate reconstitution of native cortical bone architecture. One attractive alternative to alginate is the polyethylene glycol (PEG) hydrogel. PEG hydrogels provide extensive tailorability of degradation kinetics by incorporation of cleavable peptides, as well as allowing covalent biofunctionalization with adhesive motifs and therapeutic proteins [222]. Such an approach may allow tight control of growth factor presentation and release as well as degradation kinetics to facilitate integration and remodeling. Future studies will compare the release and degradation properties and bone regeneration capacity of other hydrogel-based delivery systems with the alginate gel described here.

An alternative explanation for the failure to remodel to native cortical architecture is that rat bone does not feature secondary remodeling (i.e. osteonal, BMU-based cutting cones) as in large animals and humans. As a result, extensive reconstruction of architectural features over the time course of these studies may not be feasible in the rat model. Therefore, currently ongoing ovine studies will assess the nanofiber mesh/alginate delivery of rhBMP-2 in a critically-sized 3 cm tibial defect in the sheep (Figure 6.2). These studies, conducted in collaboration with Dr. Dietmar Hutmacher at the Queensland University of Technology in Brisbane, Australia will investigate the efficacy of the mesh/alginate delivery system in a similar sized defect to those found in humans, and will explore the influence of osteonal remodeling on gel degradation and cortical reconstruction.

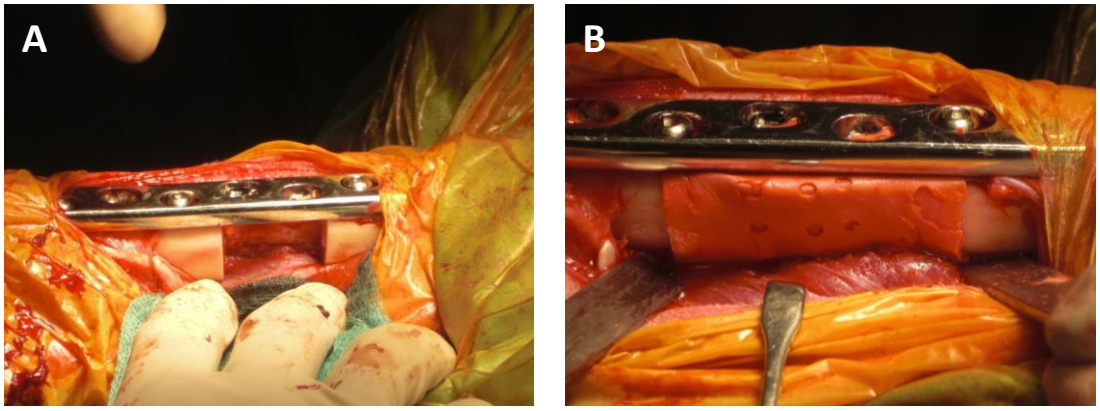

Figure 6.2. Ongoing sheep bone defect study: critically-sized 3 cm defect in the sheep tibia (A), with electrospun nanofiber mesh placed around the defect (B).

In Chapter V, the effect of rhBMP-2 on vascular growth was indirectly evaluated, demonstrating increased vascular network formation with an increased dose of rhBMP-2. Future experiments will study vascular network formation in empty and scaffold-only defects to evaluate the role of rhBMP-2 and bone formation on vascular growth. Large differences in vascular morphology, distribution, and orientation were also seen at week 3 post-surgery between treated defects and unoperated age-matched controls. Future studies will evaluate later time points to assess the extent and time course of vascular remodeling in large bone defects treated with sustained delivery of rhBMP-2.

EFFECTS OF MECHANICAL LOADING

Chapters IV and V evaluated the effects of in vivo mechanical loading on bone formation and neovascular growth. The study described in chapter IV first demonstrated that functional transfer of axial loads by modulation of fixation plate stiffness significantly alters BMP-mediated large bone defect repair by increasing bone formation and distribution and modulating tissue organization and differentiation. The study described in Chapter V then demonstrated that the timing of load application significantly affects the healing response, with early loading disrupting vascular growth and inhibiting

bone formation and delayed loading enhancing bone formation and vascular network remodeling. Together, these data indicate that consideration and modulation of the mechanical environment may improve clinical treatment of challenging segmental bone defects as well as advance our understanding of the role of biomechanical factors in bone tissue differentiation, formation, and remodeling.

The results described here have several similarities with the response of bone fractures to mechanical loading, though key differences are also evident. As in fracture healing, mechanical loading altered the tissue differentiation profile and increased and prolonged the chondral phase of endochondral ossification [97, 102, 110, 140]. Also, like fracture healing, the early phase of healing was highly sensitive to mechanical conditions, and excessive motion resulted in development of nonunion [103, 110, 139, 149, 250]. However, large bone defect healing differs from canonical fracture healing, in that the defects are critically-sized and will not heal without intervention. Besides providing a more challenging model to evaluate the efficacy of various treatment strategies, this may change the response to mechanical conditions. In fracture healing, early loading has been shown to stimulate both vascular growth [250] and bone formation [107], however the small size of the gap may prevent the large deformations seen in the present early loading study. In large bone defect healing, without sufficient biological stimulus to induce bone formation, the tissue may be particularly sensitive to the magnitude of interfragmentary strains. The potential for low or moderate deformations to enhance the early stages of defect healing have not been evaluated. Future studies will assess the effects of early loading using a modified compliant fixation plate which features an increased axial stiffness to decrease interfragmentary strains. This can be accomplished easily by

increasing the stiffness of the elastomer segments or by changing the plate geometry. A possible limitation of the clinical applicability of this work is that with internal fixation, plate actuation requires a secondary surgical intervention. These limitations may be addressed by use of external fixators such as the Ilizarov ring system, which remains a popular fixation device for such defects, or use of internal fixation plates with time-variable stiffness by incorporation of degradable segments.

However, preliminary studies (data not shown) suggested that without sufficient rhBMP-2 to cause defect bridging, mechanical loading failed to enhance repair, likely as a result of large deformations as observed in the early loading study. Future experiments will therefore directly evaluate delayed loading with a low dose of BMP to determine whether defect bridging prior to load application is required for an anabolic effect or whether loading can overcome an insufficient biological stimulus.

Ongoing studies are investigating the cellular and molecular mechanisms of BMP-mediated bone regeneration and mechanical loading through immunohistochemistry. Histological analysis has highlighted the dense presence of osteocytes in newly formed bone matrix, and these cells may be responsible for coordination of mechano-adaptive processes [40]. Immunostaining will be therefore conducted to localize markers of bone modeling and remodeling, including osteoblastic differentiation (osteocalcin, osteopontin), matrix production (pro-collagen I), and osteoclast activity (tartrate-resistant acid phosphatase - TRAP), as well as blood vessel formation and remodeling (CD31/PECAM-1, Ang-2), and inflammation (CD14, CD68, IL10). These studies will allow investigation of the interactions between the time course

of angiogenesis, inflammation and early osteoblast activity to better understand the stages of bone defect repair and the proper timing of protein delivery and load actuation.

Also, in collaboration with Dr. Georg Duda and Dr. Peter Fratzl at the Julius Wolff Institute in Berlin, Germany, we are currently investigating the local effects of vascularization on mineralization and nanostructure by quantifying the orientation and size of mineral crystals near to and far away from blood vessels, both in the mature intact bone of the proximal and distal femur and in the newly-formed bone in the bone defect, under both stiff and compliant fixation. These studies will employ the small-angle X-ray scattering technique developed by our collaborators [339-340].

Future studies will also examine the effects of mechanical loading on limbs treated with collagen sponge delivery of rhBMP-2. Because this scaffold degrades rapidly, the effect of loading on gross bone remodeling may be enhanced, and may allow load-mediated restoration of a cortical architecture, which is not observed in the stiff plate samples with collagen sponge and rhBMP-2. Other studies will examine the interactions of bone formation and vascular growth with surrounding musculature. In the present studies, the orientation of blood vessels migrating into the defects suggested that much of the vascular supply originated in the surrounding musculature. This may provide insight for the development of therapies that stimulate the surrounding soft tissues to enhance bone regeneration.

A primary limitation of the methodology chosen for application of mechanical loading to the regenerating limbs is that the mechanical environment was not explicitly controlled. Loads were not externally applied to the femur; rather, loading was passively applied by the impact and muscle contraction forces associated with normal cage

ambulation. In these studies, all animals received bilateral defects, with the contralateral limb receiving a stiff fixation plate. There is a possibility that the differences in stiffness between the plates could cause the animal to preferentially place more weight on one limb than the other, resulting in differential healing than would be found in unilateral defects. This effect has been observed previously in sheep models of fracture healing (personal communication with Dr. Georg Duda; data unpublished). However, we have previously shown that in this model, creation of a bone defect and implantation of a fixation plate results in no significant decrease in limb usage or gait parameters, as determined by catwalk analysis [341]. Future studies will therefore evaluate unilateral defects and assess gait function to evaluate the differences in load bearing between the two groups.

Also, in these studies, we assumed that the femoral loads equaled the body weight. A recent modeling study, which evaluated both impact and muscle contraction loading, reported that femoral loads in rat bone reach 6-times the body weight during normal gait [342]. This would suggest higher magnitude boundary conditions than those reported here. However, we have recently demonstrated that the presence of an internal fixation plate reduces the maximal force capable by the biceps femoris muscle by 68% [343]. Together these suggest that the boundary conditions used are similar to those found in vivo. While some uncertainty is incurred, a sensitivity analysis determined that an order-of-magnitude variation in femoral load did not alter the comparisons of local strain distributions or relative strain magnitudes between the stiff and compliant plates.

Future studies will employ several approaches to addressing these limitations using (1) the current loading model, (2) a modified rat model, and (3) a large animal

model. First, using the current ambulatory loading model, we aim to indirectly modulate the magnitude and frequency of loading by exposing the animals to controlled regimens of physical exercise. This will be conducted using two approaches: trained wheel running and forced swimming in a current pool as conducted previously in our lab by Duvall et al. [326]. The use of both the running and swimming regimes will allow comparison of combined impact and muscle contraction loading with muscle loading only.

Second, to accurately control the applied loading, we will employ an external fixation device, rather than internal fixation, to which controlled loads will be applied by an external mechanical loading system. This approach has been explored previously for fracture healing studies [102], and will investigate the various effects of timing, magnitude, frequency, and loading mode (i.e. compression, tension, bending, etc.). To further isolate the applied loads, tail suspension can be implemented to remove all non-specified loads and fully describe the mechanical history.

Finally, due to size constraints in the rat model, it is difficult to measure mechanical conditions; however, in the forthcoming sheep studies, direct measurement of interfragmentary strains will be conducted using transcutaneous markers as performed elegantly by Duda and colleagues [105, 109]. This will allow use of the more clinically-relevant patient-induced loading, but will provide real time measurement of mechanical boundary conditions. Together, these further experiments will provide insight into the therapeutic window of local stress/strain magnitudes, frequencies, and modes, with the goal to improve bone defect fixation strategies and physical therapy recommendations for clinical treatment of large bone defects.

Independent of bone formation and bone defects, the effects of matrix deformations on neovascular growth and angiogenesis remain an interesting question, with application in tissue engineering and cancer growth and metastasis. The effects of mechanical conditions on vascular network growth and remodeling are complex and varied. Several in vitro systems have attempted to assess the effects of matrix deformations on endothelial cells in 3D culture [322-323, 338], but a model system for applying known mechanical deformations to vascular networks in vivo has not yet been developed, to our knowledge. Such a tool could greatly enhance our understanding of the mechanoregulatory mechanisms that govern post-natal angiogenesis and network remodeling.

Future work will therefore develop and characterize a subcutaneous loading chamber angiogenesis model (Figure 6.3) to isolate the neovascular response to controlled mechanical deformation in the absence of concurrent bone growth. Several models are commonly used to study post-natal angiogenesis [344-347]. One of the most frequent is the subcutaneous Matrigel® assay [348-352]. Matrigel is a mixture of extracellular and basement membrane proteins extracted from the mouse Engelbreth-Holm-Swarm sarcoma and has been shown to simulate endothelial cell differentiation and tube formation [346, 353]. We have chosen to modify the Matrigel chamber assay described by Ley and colleagues to provide elective actuation of matrix deformation [352].

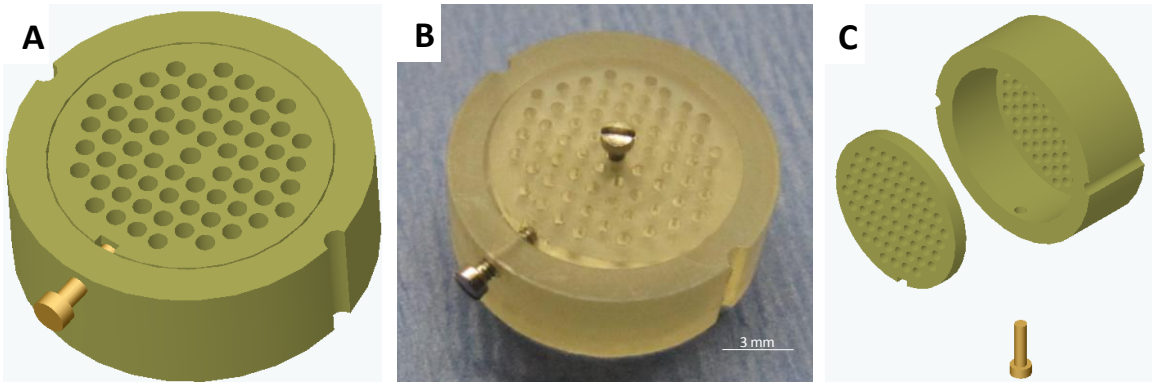

Figure 6.3. Custom-made angiogenesis loading chamber. The base and top platen are constructed of radiolucent polysulfone, and have 0.5mm diameter holes for vessel ingrowth. A movable crosshead can be screwed into the top platen via the center hole to actuate loading and the base stabilized by clamping onto the side channels. The overall dimensions are 14mm Ø x 5mm height. The internal volume is approximately 250µl. (A): CAD assembly. (B): Photograph of prototype with set screw and top screw indicating loading arm attachment location. (C): Exploded view showing chamber interior and porosity.

Experiments will evaluate the effects of different modes and magnitudes of loading on new blood vessel networks. Initially, pilot studies will be conducted to determine a proper formulation for an angiogenesis-supporting matrix, and to determine the necessary doses of angiogenic growth factors such as FGF and VEGF to stimulate blood vessel network formation. After determination of a dose of angiogenic growth factors that will result in robust angiogenesis and confirmation that these vessels can be quantified by microCT angiography, that dose will be selected to create constructs that will be exposed to tensile and compressive deformations. We hypothesize that there will be a biphasic load-response profile in which moderate stretching of a subcutaneous vascular network will enhance vascular remodeling to modulate vessel size, number, and distribution, but larger regimens of mechanical stimulation will subsequently hinder vascular growth.

CONCLUSIONS

In conclusion, these data describe the rhBMP-2 dose-response relationships and temporal release properties of a hybrid alginate-based protein delivery system in comparison to the clinically-used collagen sponge and demonstrate that this system improves bone formation over current delivery methods. This work highlights the importance of quantification of release kinetics and scaffold degradation properties for evaluating novel recombinant protein carriers. These data also demonstrate that, while sensitive to timing, in vivo mechanical loading can enhance large bone defect regeneration and modulate vascular growth and remodeling. Together, these observations suggest that controlled modulation of the biochemical and biomechanical environments may improve clinical treatment of challenging bone defects.

APPENDIX A: EARLY MODEL DEVELOPMENT*

Introduction

This appendix describes the development of the uniaxially compliant fixation plates used in this thesis as well as previous designs which, despite showing promise for developing models of hypertrophic nonunion, were not suitable for mechanical stimulation of bone formation. These studies featured delivery of rhBMP-2 using structural poly-lactic acid scaffolds in combination with alginate hydrogel.

Methods

Compliant Fixation Plate Development:

To achieve load transfer from the plate to the construct, the standard plates described previously [275] were first modified by incorporating a full-thickness segment of silicone elastomer (RTV Silicone Adhesive, Factor II, Inc., Lakeside, AZ) (Figures A.1(a) and A.1(b)). This design was multiaxially compliant, possessing a low stiffness in response to multiple loading modes – axial, bending, torsion and shear. A second design allowed only axial deformation of the defect under ambulatory loads by constraining the stainless steel plates which were fixed to the bone to slide with respect to the polysulfone plate bridging the defect (Figures A.1(c) and A.1(d)). A finite axial stiffness was effected by incorporating the silicone elastomer between the steel and polysulfone plates. A

* This section is modified from Boerckel et al. "In vivo Model for Evaluating the Effects of Mechanical Loading on Tissue-Engineered Bone Repair." Journal of Biomechanical Engineering 2009 (reference 274).

removable stainless steel clip served as a locking system that allowed elective actuation of load-sharing.

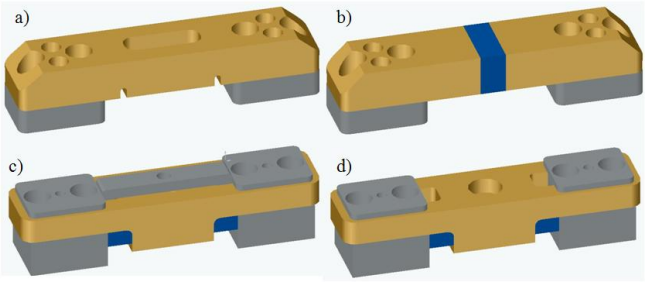

Figure A.1. Fixation Plate designs. (a) Standard plate, (b) multiaxially compliant plate, (c) unactuated uniaxially compliant plate, (d) actuated uniaxially compliant plate. Removal of the rigid clip actuates the uniaxial plate, allowing load transduction through the elastomer (in blue).

In the first study, femurs were stabilized by the standard fixation (std.) plate described previously. In experimental limbs, the standard plates were replaced in a second surgery at 8 weeks post-surgery with the multiaxially compliant (multi.) plates.

In the second study, experimental limbs were stabilized by the axially compliant (axial) plates. At the time of implantation, the axial plates were constrained to prevent motion and were actuated at week 4 post-implantation by surgical removal of the clip.

Fixation Plate Mechanical Characterization

Characterization of axial, flexural, and torsional plate stiffness was performed by affixing the plates to age-matched excised femurs and potting the epiphyses in Wood's metal (Alfa Aesar, Ward Hill, MA). Axial tests were conducted with and without a hydrated scaffold placed in the defect, and were performed under displacement control at a rate of 0.01 mm/sec to a displacement of 1 mm. Torsional tests were conducted under angular displacement control to a rotation of +/- 5 degrees at a rate of 0.1 deg/sec. Finally, three-point bending tests were conducted for the standard and axially-compliant plates under displacement control to a maximum deflection of 0.5 mm at a rate of 0.02

mm/sec. The multiaxially compliant plates were tested in four-point bending to a maximum displacement of 1mm at a rate of 0.05 mm/sec. Standard beam bending theory was used to calculate the average flexural stiffness of each plate from the recorded loads and deflections.

Scaffold Production:

Poly(L-lactide-*co*-D,L-lactide 70:30)/tri-calcium phosphate (PLDL-TCP) scaffolds were produced with longitudinally-oriented porous microarchitecture as previously described [354]. Briefly, 100 micron diameter removable fibers coated with medical grade PLDL combined with 10% TCP, by weight, and the porogen azodicarbonamide were used to create longitudinal pores, followed by decomposition of the porogen at 260 ^{o}C resulting in a random microporosity. The scaffolds were cut to size (4mm diameter x 8mm length with 1.5mm diameter core) and sterilized by gamma irradiation (2.5 Mrad).

Growth Factor Loading

Each scaffold was coated with 25µg/mL rat plasma fibronectin (F0635; Sigma-Adlrich, St. Louis, MO) to improve cellular adhesion, and then loaded with bone morphogenetic protein 2 (BMP-2) (355-BM/CF, R&D Systems, Minneapolis, MN) using a previously described protocol [275]. Briefly, the protein was reconstituted in 2% RGD-functionalized alginate, which was pipetted into the scaffold and crosslinked by bathing in $CaCl_2$. Each scaffold received a volume of 50 µL of RGD-alginate containing 2 µg BMP-2.

Animal model & analysis techniques

Rat segmental defects were created and evaluated by Faxitron, microCT, and mechanical testing as described previously (see Chapter III, IV, and V).

Finite Element Modeling

MicroCT image-based finite element models of the defect and ingrown tissues at four weeks post-surgery were created to predict tissue-level stress and strain distributions resulting from estimated ambulatory loads. One animal was sacrificed at four weeks post-surgery and a femur was excised, mechanically tested in axial compression, and scanned at medium resolution with an isometric voxel size of 21μm. Images thresholded for both bone and soft tissues/scaffold material were concatenated and then voxels were converted directly to finite elements. By assigning the newly-formed bone a local modulus of E_{bone} = 2 GPa and comparing the effective axial stiffness of the model to the measured value determined by mechanical testing of that same femur, the soft tissue and scaffold modulus, E_{st}, could be estimated.

Results

Fixation Plate Characterization

Table A.1. Fixation plate mechanical characterization. All values given as mean ± std. deviation.

	Standard Plate	Multiaxial Plate	Uniaxial Plate	
			Actuated	Unactuated
Axial Stiffness (k) without scaffold [N/mm]	214.3 ± 4.1	9.58 ± 2.95	8.4 ± 0.4	349.5 ± 35.1
Axial Stiffness (k) with scaffold [N/mm]	256.3 ± 32.8	93.6 ± 18.8	87.0 ± 28.3	404.9 ± 60.3
Torsional Stiffness (GJ/L) [kN-m/deg]	14.8 ± 1.61	0.802 ± 0.133	6.95 ± 0.18	9.14 ± 2.94
Flexural Rigidity (EI) concave [N-mm^2]	29236.3 ± 260.8	146.3 ± 50.4	25688.3 ± 657.4	26938.7 ± 629.5
Flexural Rigidity (EI) convex [N-mm^2]	30472.0 ± 736.8	132.0 ± 29.0	28015.0 ± 2076.1	42392.0 ± 8350.1

Mechanical characterization of the plates revealed that the axial compressive stiffness of the standard plates was 214.3 ± 4.1 N/mm (mean ± std. dev.) (Table 1). With a hydrated scaffold placed in the defect to approximate the day-zero mechanical environment, the effective stiffness increased by 19%. The axial stiffnesses of the multiaxial and actuated uniaxial plates were 3.9% and 4.5% of the standard plate stiffness, respectively. Actuation of the uniaxial plates by removal of the rigid clip reduced the axial stiffness by 97.6%. In comparison with the standard plate, the unactuated uniaxial plate was 58% and 63% stiffer with and without the scaffold, respectively. This indicates a higher degree of stress shielding in the experimental limbs prior to actuation. With the scaffold in place, the effective axial stiffness of the multiaxial and actuated uniaxial plates was increased 9.8- and 10.4-fold, respectively, demonstrating increased axial load transduction to the construct in the compliant plates.

Though comparable to the actuated uniaxial plates in axial compression, the multiaxial plates were an order of magnitude less stiff than either the standard or uniaxial plates in torsion. The torsional stiffness of the multiaxial plates was 95% less than that of

the standard plate, while the actuated and unactuated uniaxial plates were 53% and 39% less stiff in torsion, respectively, compared to the standard plates.

While the standard and uniaxial plates had comparable stiffness in response to bending loads, the multiaxial plates were 99.5% less stiff than either the standard or uniaxial plates in bending.

As expected, therefore, mechanical testing revealed that in axial compression, the multiaxial plates and actuated uniaxial plates responded similarly and were significantly less stiff than either the standard plates or the unactuated uniaxial plates. In torsion and bending, the multiaxial plates were substantially less stiff than both the standard and uniaxial plates.

Pilot Study 1: Multiaxial Plate

Following implantation of the multiaxially compliant plates at 8 weeks post-surgery (n=2), the shear and bending loads exerted during ambulation caused large deformations of the defect upon impact and the limbs re-straightened during the swing phase of the gait (Figure A.2), resulting in complete nonunion by week 12 (Figure A.3). This indicated that the multiaxially compliant plates were insufficiently stiff to prevent instability of the defect after 8 weeks of stable healing and precluded post-mortem CT scanning and biomechanical testing.

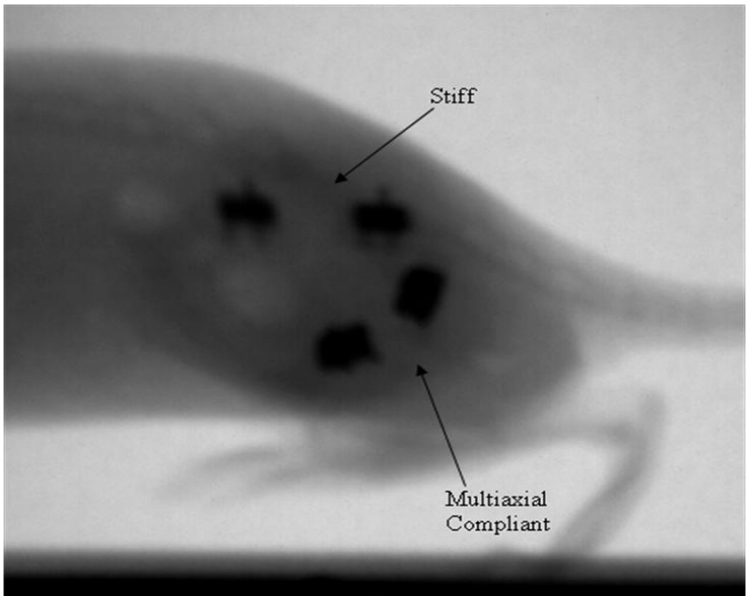

Figure A.2. In vivo X-ray videography of rat ambulation with multiaxial plates. The low bending stiffness of the multiaxial plates resulted in large deformation of the limbs during impact, which straightened during the swing phase.

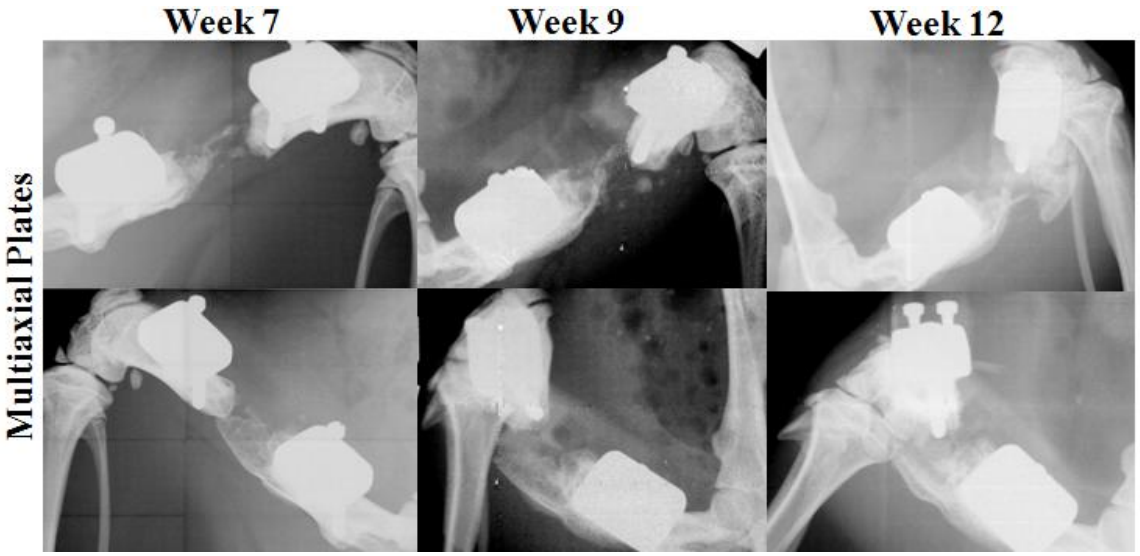

Figure A.3. Faxitron images of multiaxial plates. Replacement of standard plates with multiaxial plates at 8 weeks post-surgery resulted in failure under shear and bending loads, which precluded post-mortem microCT scanning and biomechanical testing.

Pilot study 2: Uniaxial Plate

As a result of these observations, the compliant plates were redesigned to allow only uniaxial deformations. The rationale was that shear deformations may be responsible for inducing failure, particularly at the scaffold-bone interface. The BMP-2 delivered within PLDL/TCP scaffolds induced formation of low density bone by 4 weeks within the defect region. Longitudinal Faxitron scans demonstrated that after actuation of the plate at week 4 post-surgery, the uniaxial plate maintained stability of the defect, and both the loaded sample and the contralateral standard control achieved bridging at 12 weeks (Figure A.4).

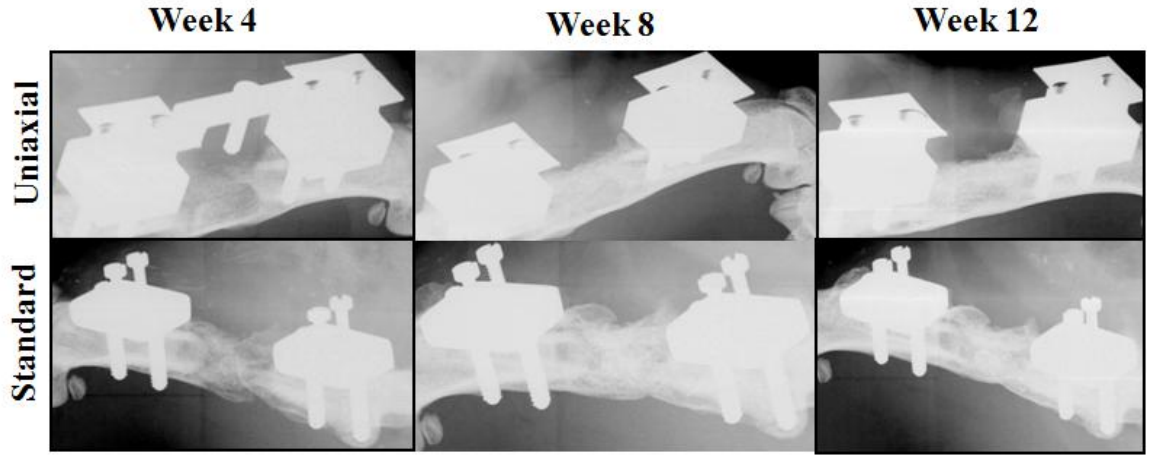

Figure A.4. Faxitron images of uniaxially compliant plate, actuated at week 4 post-surgery, and contralateral standard plate. The uniaxially compliant plate successfully maintained stability of the defect over the 12 week implantation period. Both samples achieved qualitative union.

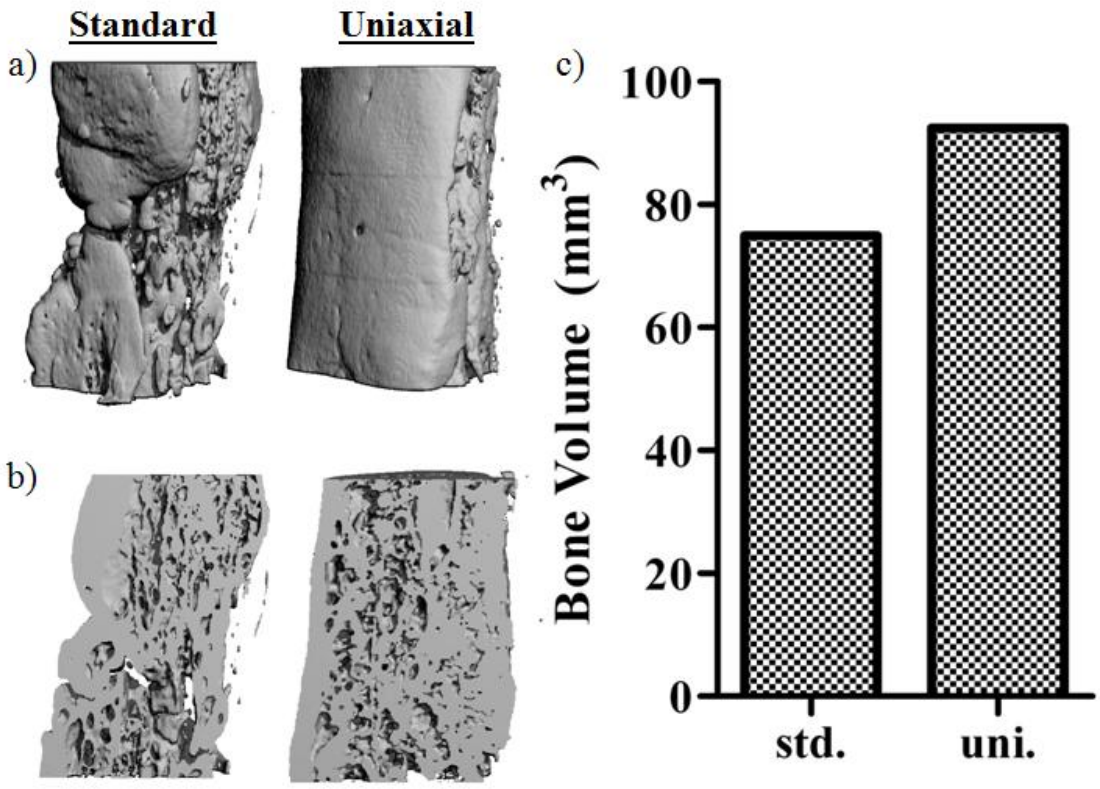

Figure A.5. Post-mortem microCT. (a) Images of center 7mm used for evaluation, (b) sectioned images to demonstrate internal architecture and connectivity, and (c) bone volume quantification over a constant VOI. Bone volumes were comparable for the two samples. Cut images demonstrate a more uniformly connected morphology in the uniaxial sample.

Quantitative microCT analysis revealed that bone volume (BV) within the central volume of interest was 18.9% greater in the loaded sample (Figure A.5). Consistent with this increase in BV, post-mortem biomechanical testing indicated that the torsional strength and stiffness of the loaded construct were substantially greater than those of the contralateral standard control. The torsional stiffness and maximum torque were 25.6- and 3.9-fold greater in the stimulated limb compared to the control (Figure A.6). These properties were greater than those of age-matched intact femurs whose torsional stiffness and max torque were 0.030±0.001 N-m/deg and 0.31±0.02 N-m, respectively, indicating full functional regeneration of that limb. These values were also greater than those

previously achieved using the same model with standard fixation and this growth factor dose [275], suggesting a positive effect of loading on defect healing.

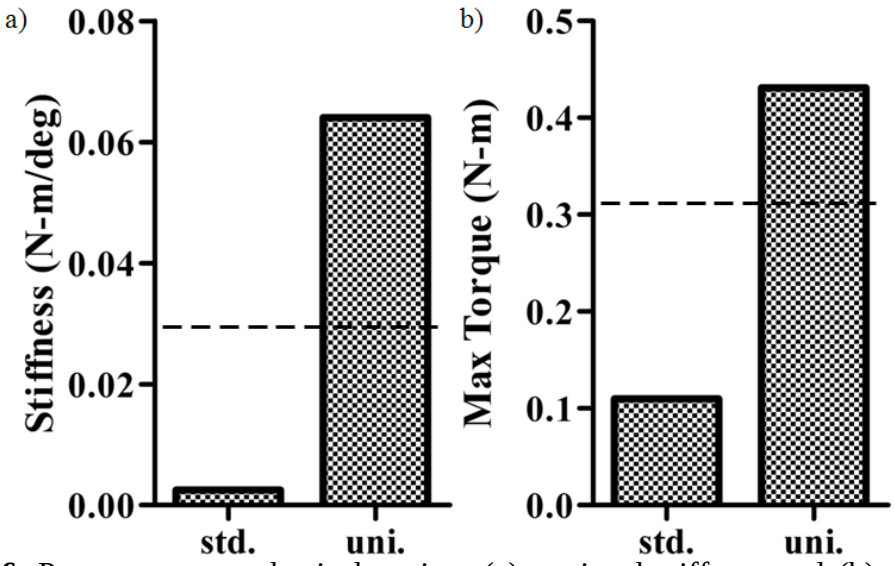

Figure A.6. Post-mortem mechanical testing: (a) torsional stiffness and (b) maximum torque. Dotted lines represent average properties of age-matched intact femurs. The mechanical properties of the uniaxially loaded sample were 2460% and 293% greater than the sample fixated with the standard plate for stiffness and maximum torque, respectively.

Finite Element Modeling

Image-based finite element modeling of a femur, excised, scanned and tested at 4 weeks post-surgery indicated an effective stiffness of 7.05 N/mm. Back calculation of local tissue modulus by comparison of measured to computed effective stiffness indicated an average soft tissue/scaffold modulus of 0.7MPa. Under estimated physiologic loads, the average axial strain in the newly-formed bone was -0.09 μstrain and -3.8E4 μstrain in soft tissues/scaffold. FE simulation revealed low principle compressive strains in the in-growing bone and high strain gradients in the soft tissue adjacent to newly formed bone (Figure A.7). Spatial gradients of strain have previously been postulated to drive local adaptation of bone microstructure during repair [355].

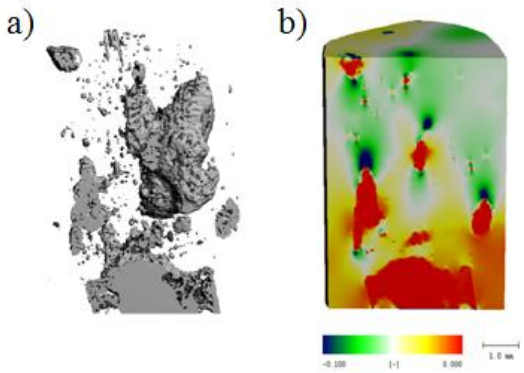

Figure A.7. Finite element modeling: (a) microCT image of bone growth at week 4, sectioned and (b) minimum principle strain distributions at week 4 under estimated boundary conditions at same section. FE modeling revealed high strain gradients in the soft tissue adjacent to newly formed bone within the implanted construct.

Discussion

The effects of mechanical loading on large bone defect regeneration have not yet been evaluated. To that end, a challenging rat segmental defect model has been modified to allow transduction of ambulatory loads to the ingrowing bone within the tissue-engineered construct. Multiaxially compliant fixation plates with low stiffness in response to shear and bending loads failed to maintain defect stability and promote functional repair. The sample fixated with the uniaxially compliant plate allowed axial deformation of the scaffold under physiologic loads, while restricting bending and shear deformations to maintain stability of the defect. Preliminary results using this new in vivo model suggested positive effects of load-bearing on functional defect repair. Loading may influence the functional integration of a tissue-engineered construct by altering the amount, organization, or mineralization of newly formed bone. Upcoming studies will repeat this work with larger sample sizes to test this hypothesis.

APPENDIX B: PROTOCOLS

B.1. ALGINATE PREPARATION & BMP RECONSTITUTION

Materials:

- rhBMP-2 (R&D Systems)
- Sterile filtered 4 mM HCl
- 0.1% Rat Serum Albumin (RSA)
- $CaSO_4$ (Calcium sulfate – 325, mesh)
- RGD-Alginate
- Alpha-MEM
- Sterile 50 ml conical tubes
- Sterile syringe filters
- 10 ml syringe
- Sterile 1ml syringes
- Leuer-lock connectors
- Leuer lock caps
- Sterile drape
- Sterile gloves
- Assistant

Solution Preparations:

- 4mm HCl
    - Can make this up prior.
    - Sterile filter & keep hood-sterile
- 0.21 g/ml $CaSO_4$
    - 5.25 g $CaSO_4$
    - 25 ml DI H_20
    - Autoclave on liquid cycle (shortest time ~15 min), with cap loose. Take out of autoclave asap to prevent evaporation.
    - Can autoclave this day before.
- 0.1% RSA
    - Add 1 mg RSA per ml 4mM HCl (make up at least ~5ml to allow for accurate measurement).
    - Sterile filter into 50 ml conical tube.
    - Make up just prior to use.
- 3% Alginate
    - Determine volume of Alginate needed ($\mathbf{A_3}$ below). Add 0.03g/ml (see **A** below) alginate to $\mathbf{A_3}$ ml alphaMEM. Do this slowly without vortexing or shaking.
    - Make up just prior to use.
- 100 ug/ml BMP-2

- 100 ul 4 mM HCl
- 10 ug BMP
- Use up 10ug or 50ug vials accordingly up to the necessary amount.
- Make this up last, just prior to use.

Procedure:

1. Calculate total volume of BMP + alginate needed:
    - **V** = # defects * 0.150 ml/defect
    - **V=_____**
    - Account for ~25% loss + extras for lost animals, etc.
2. Calculate mass of alginate in final 2% solution
    - **V** ml * 0.02g/ml = **A** g alginate
    - **A = _____**
3. Calculate volume of 3% alginate needed:
    - **A** g alginate / (0.03 g/ml alginate) = $\mathbf{A_3}$ ml
    - $\mathbf{A_3}$ **= _____**
4. Make up 3% alginate solution to volume $\mathbf{A_3}$.
    - Tare scale with new sterile 50ml conical.
    - In hood, remove alginate from sterile conical and place into the weighing conical.
    - Weigh. Remove or add alginate in hood with sterile instruments until arrived at necessary amount.
    - Add $\mathbf{A_3}$ ml alphaMEM to **A** g alginate, slowly. Do not shake, invert, or vortex.
5. Determine desired dose: **D** (ie. 5 ug/defect)
    - **D** = _____
6. Calculate amount of BMP solution needed:
    - **B = (D** / (0.150 ml)***V) /** 100 ug/ml
    - **B = _____**
7. Make up BMP-2 solution at 100 ug/ml to volume **B**.
8. Calculate amount of extra media needed:

- **M = V - A_3 – B**
- **M = _____**

9. Calculate amount of $CaSO_4$ needed:
    - **C** = **V**/25
    - **C = _____**
10. Put on sterile gloves.
11. Set out sterile drape in hood.
12. Have assistant empty 1ml syringes, leuerlock connectors & caps onto drape.
13. Mix **A_3**, **B**, and **M** in between syringes, removing all bubbles at end.
14. Mix this with **C** into a separate syringe. Do this *rapidly*, taking care not to let any bubbles in at the beginning. Some bubbles will form in the mixing process. The fewer the better.
15. Place cap on and refrigerate at 4^oC until use the next day.
16. Keep on ice during surgery.

B.2. FLUOROPHORE TAGGING OF BMP

Materials:

- rhBMP-2 (R&D Systems)
- 4 mM HCl
- 100 mM $NaPO_4$ (monobasic) pH 7.5
- 3 kd Millipore Amicon Ultra Centrifugal Filters (Cat # UFC500396)
- Centrifuge
- Phosphate buffered Saline (w/o Ca & Mg)
- Visen Medical VivoTag-S 750 In vivo NIR fluorochrome label (Part # 10123 – 1mg)
- Zeba Spin Desalting Column (Thermo Scientific #89882)

Solution Preparations:

- 4mm HCl
  -
- 100 ug/ml BMP-2
  - 100 ul 4 mM HCl
  - 10 ug BMP
- 100 mM $NaPO_4$
  - 1.38 g $NaPO_4$
  - 100 ml DI H_20
  - pH to 7.5 using 3N NaOH
- 50 ug/ml fluorochrome label
  - 20 ml $NaPO_4$
  - 1 mg label

Procedure:

1. Make up BMP-2 solution
2. Buffer exchange to $NaPO_4$
   - Pipette BMP into 3kD microcentrifuge filter
   - Add 400 ul $NaPO_4$
   - Centrifuge at 14000 g for 30 min.
   - Add 500 ul $NaPO_4$
   - Centrifuge at 14000 g for 30 min.
   - Collect by centrifuging at 4000 g for 30 sec. with filter upside down into new tube – yields ~20 ul
3. Add 80 ul 50 ug/ml label to BMP

a. This gives 6.67nM BMP and 40.8 nM label => 6.12 molar excess of dye.

4. Incubate 4 hrs at room temp in **dark.**
5. Exchange buffer to PBS through Zeba spin desalting column
    a. Remove bottom closure and loosen cap
    b. Place column in 1.5-2ml collection tube.
    c. Centrifuge at 1500 g for 1 minute to remove storage solution
    d. Place mark on side of column where compacted resin is slanted upward. Place column in the centrifuge with the mark facing outward in all subsequent steps.
    e. Add 300 ul of buffer (PBS) on top of resin bed. Centrifuge at 1500 g for 1 min
    f. Repeat last step 3 additional times, discarding buffer from the collection tube.
    g. Place column in new collection tube, remove cap and apply 100 ul of sample to the top of the compacted resin bed.
    h. Centrifuge at 1500 g for 2 minutes to collect sample. Discard column after use.
6. The BMP is now labeled.
7. Use nanodrop to determine final BMP concentration (to 1 sig fig).
8. Run ~2 ug labeled and unlabeled BMP in parallel lanes in SDS-PAGE gel to ensure protein is tagged and excess dye is eliminated.
9. Image using IVIS at 745 nm excitation and 780 nm emission.

B.3. MICROCT ANGIOGRAPHY: RAT PERFUSION TECHNIQUE

Materials:

- 0.9% normal saline
- 0.4% (m/v) papaverine hydrochloride (Sigma-Aldrich) in 0.9% saline (vasodilator)
- Microfil MV-122 kit (yellow color lead chromate compound) (http://www.flowtech-inc.com)
- 10% neutral buffered formalin
- properly labeled waste bottles for formalin waste
- 1 pair small surgical scissors, 1 pair large scissors, 2 hemostats, 1 small curved pair of forceps, additional instruments by personal preference
- 18 gauge (green) 2" long catheter (Terumo SurFlo)
- needles
- 1ml slip tip and 30ml luer lock syringes
- peristaltic pump
- peristaltic pump tubing (Cole-Parmer Masterflex 96410-16)
- small tubing for connecting pump tubing to catheter (Cole-Parmer 95802-02)
- male and female luer lock connectors as needed
- diaper pads
- 50ml conicals for mixing Microfil and harvesting legs
- gauze and cotton swabs
- 2-0 needle-less suture
- Super glue

scale-up is based on 2 ml blood/25 g mouse, assumes rats have a blood volume of ~64 ml/kg

Solution Preparations:

- 0.9% normal saline (~150 ml/rat)
  9 g sodium chloride
  1000 ml DI water
- 0.4% Papavirin solution (~200 ml/rat)
  9 g sodium chloride
  4 g papaverine hydrochloride
  1000 ml DI water
- 10% neutral buffered formalin (~250 ml/rat)
- contrast agent (make ~30 ml/rat)
  do not add catalyst until immediately before perfusing animal
  mix 9.5% catalyst, 66.7% MV (yellow) compound, 23.8% diluent
  (ie. 21ml MV, 7.5 ml diluents, 3 ml catalyst per animal)
  do not heat MV compound

Procedure:

1. Set up the peristaltic pump, check the flow, and bleed all air out of the line using the saline solution. You may have to start flow by siphoning the saline through the tubing using a syringe.
2. Induce anesthesia at 5% isoflurane in an induction chamber.
3. Switch animal over to the face mask at 2% isoflurane.
4. Check for pedal withdrawal reflex using the toe pinch. When this reflex is not observed, the animal has reached a deep surgical plane and the procedure can begin.
5. Using needles, pin animals hands and feet to styrofoam. Legs should be as straight as possible.
6. Using scissors, cut transversely through the skin & muscles just below the xyphoid process of the rib cage to expose the diaphragm.
7. Gently cut the diaphragm, taking care not to puncture the heart or underlying vessels.
8. Cut through the rib cage to allow opening of the chest cavity. A large hemostat can be used to help keep the chest cavity open by clamping to xyphoid and positioning the instrument as necessary.
9. Carefully dissect the heart free of the connective tissue holding it to the rib cage.
10. Using small blunt tip forceps, pass a piece of 2-0 suture behind the aorta.
11. While the heart is still pumping, insert the 18g catheter into the left ventricle (apex of the heart). Blood should begin to back out of the catheter.
12. Carefully advance the soft catheter end up into the ascending aorta while backing the needle out.
13. Using a single loop with the 2-0 suture, constrict the aorta around the catheter within its lumen to prevent back-flow later in the perfusion process. Optionally, place a small amount of super glue at the insertion point for additional stability.
14. Attach the connection tubing to the catheter, making sure to minimize any air in the tubing.
15. Cut the inferior vena cava.
16. Immediately, turn on the pump, pefusing with saline ~25-50 ml

17. Perfuse withpapaverine solution ~150-200 ml. Perfusion volume is an estimate. The goal is to perfuse until vessels are clear. The liver should blanch quite quickly. Skin can carefully be cut away on the leg for “windows” to inspect perfusion of the hind limbs. The tail tip can also be cut, but should be clamped with a hemostat after observation. Kidneys can be inspected to evaluate perfusion also.
18. Clear with saline ~25-50 ml
19. Perfuse with 10% NBF ~150-250 ml. Again, perfusion volume is an estimate. The goal is to perfuse until the extremities are fully fixed. Inflation of the lungs is an indicator of backflow in the system. After ~!00 ml, one may observe relative inflation of the GI system, which is not abnormal.
20. Clear with Saline ~25-50 ml
21. Mix MV-122 with diluent in a 50 ml conical tube. Then, addcatalyst, mix, and immediately transfer to a 30 ml syringe for injection. Exhaust as much air as possible from the syringe before attaching to tubing.
22. Switch luer-lock connector from pump tubing to syringe, being careful to minimize induction of air to the system. Slowly perfuse the animal manually, taking care not to let the catheter back out.
23. Store animal in 4C refrigerator overnight to allow the microfil to polymerize.
24. Remove the hindlimbs and store in formalin for up to two weeks to fix the tissue.
25. MicroCT scan to get composite image of bone and vasculature.
26. Decalcify hindlimbs in Cal-Ex II for 2 weeks. Use only gentle agitation if any. Strong agitation will shake polymerized microfil out of the vessels.
27. MicroCT scan to get vasculature alone.

APPENDIX C: FIXATION PLATE DRAWINGS

C.1. STIFF FIXATION PLATE DRAWINGS

C.1.1 Polysulfone Plate

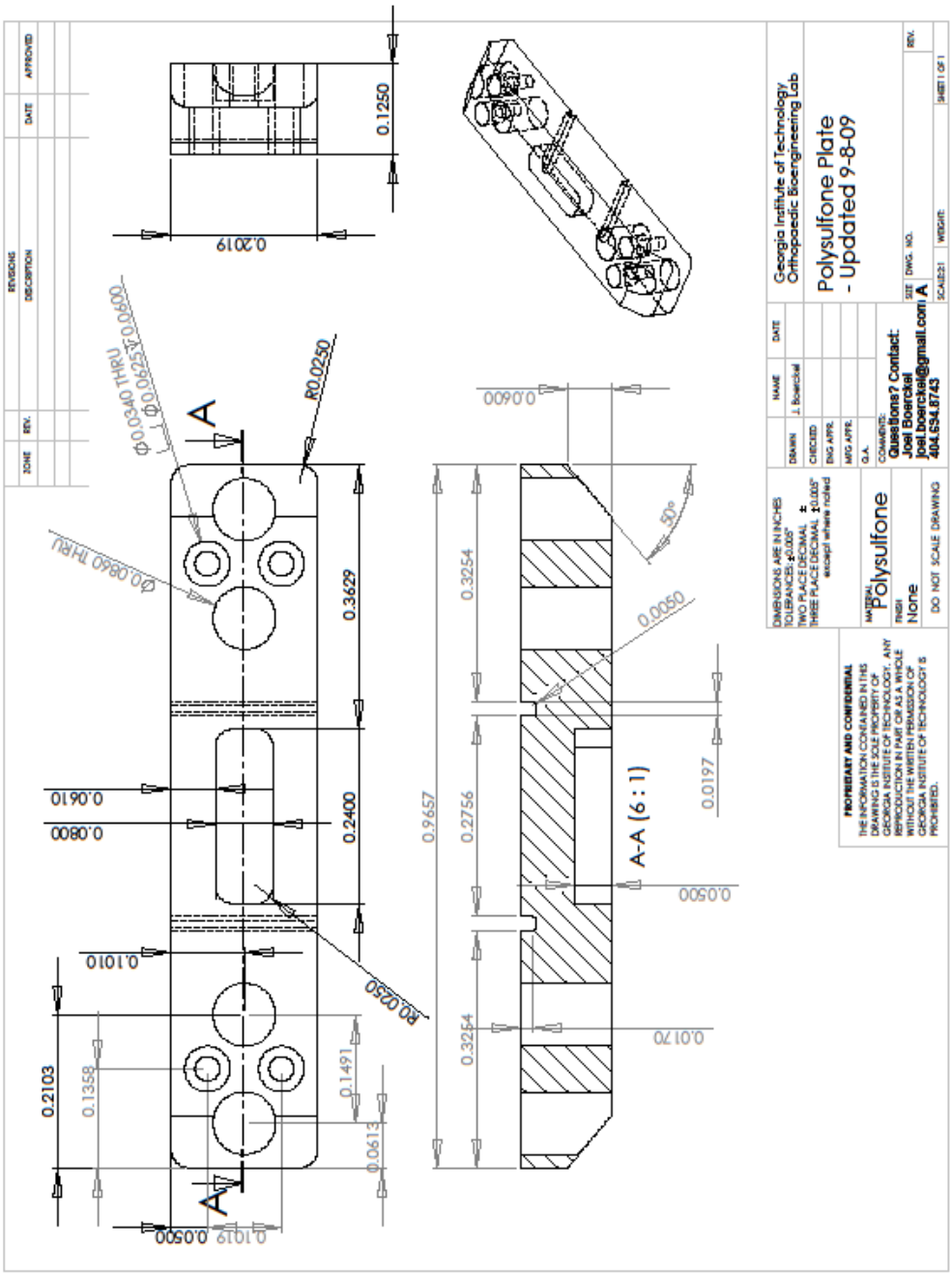

C.1.2 Steel Plate

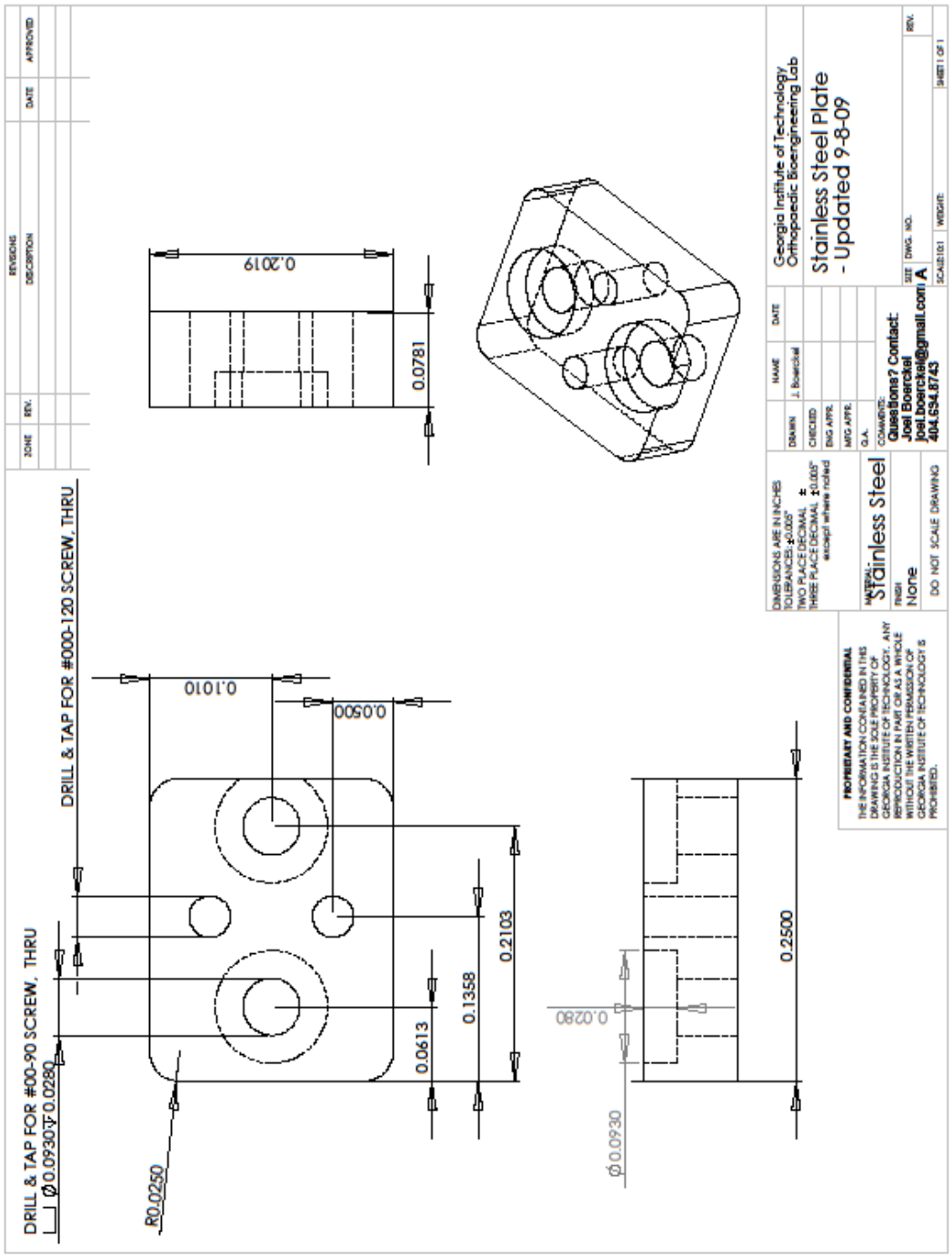

C.2. COMPLIANT FIXATION PLATE DRAWINGS

C.2.1 Polysulfone Plate

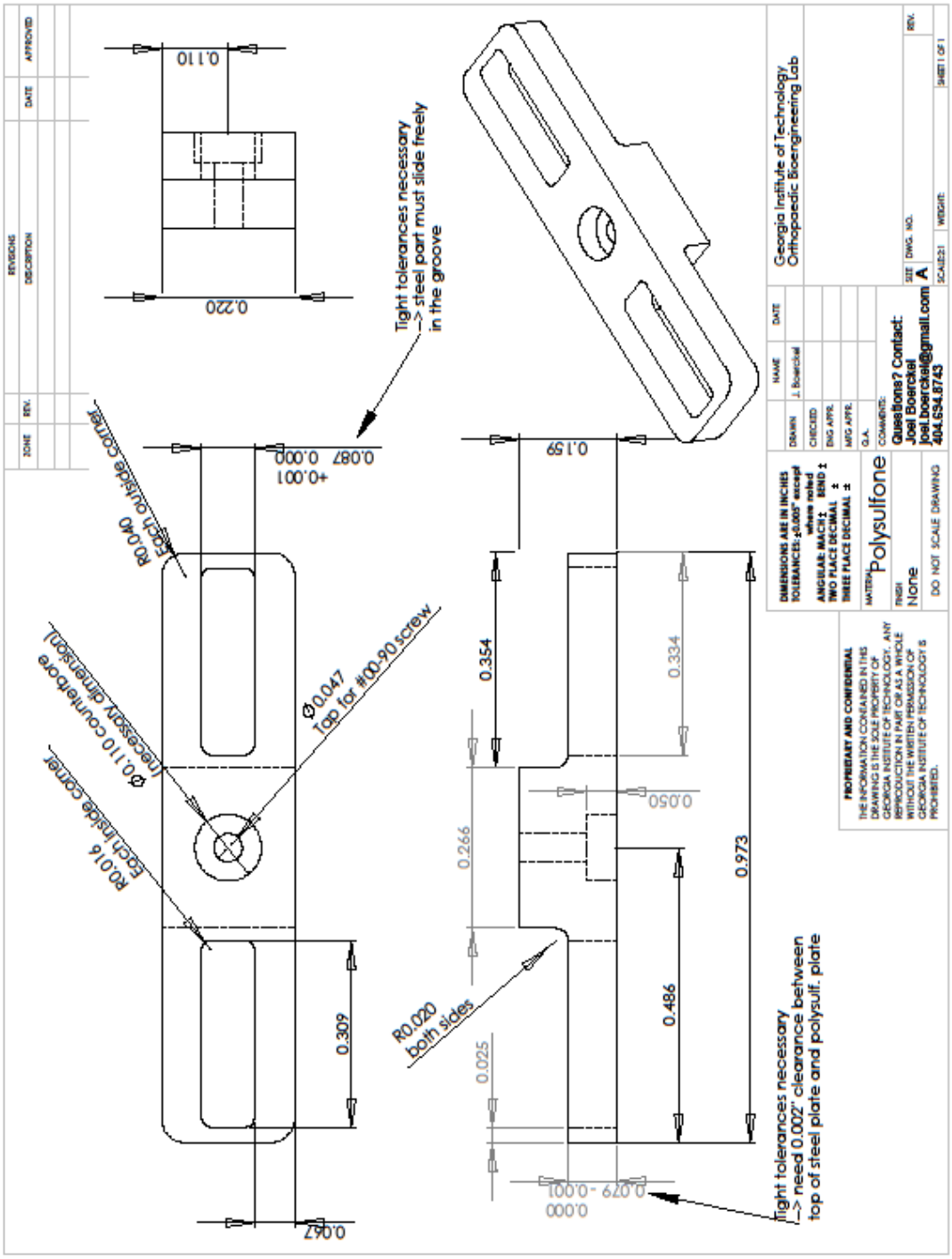

C.2.2 Steel Plate

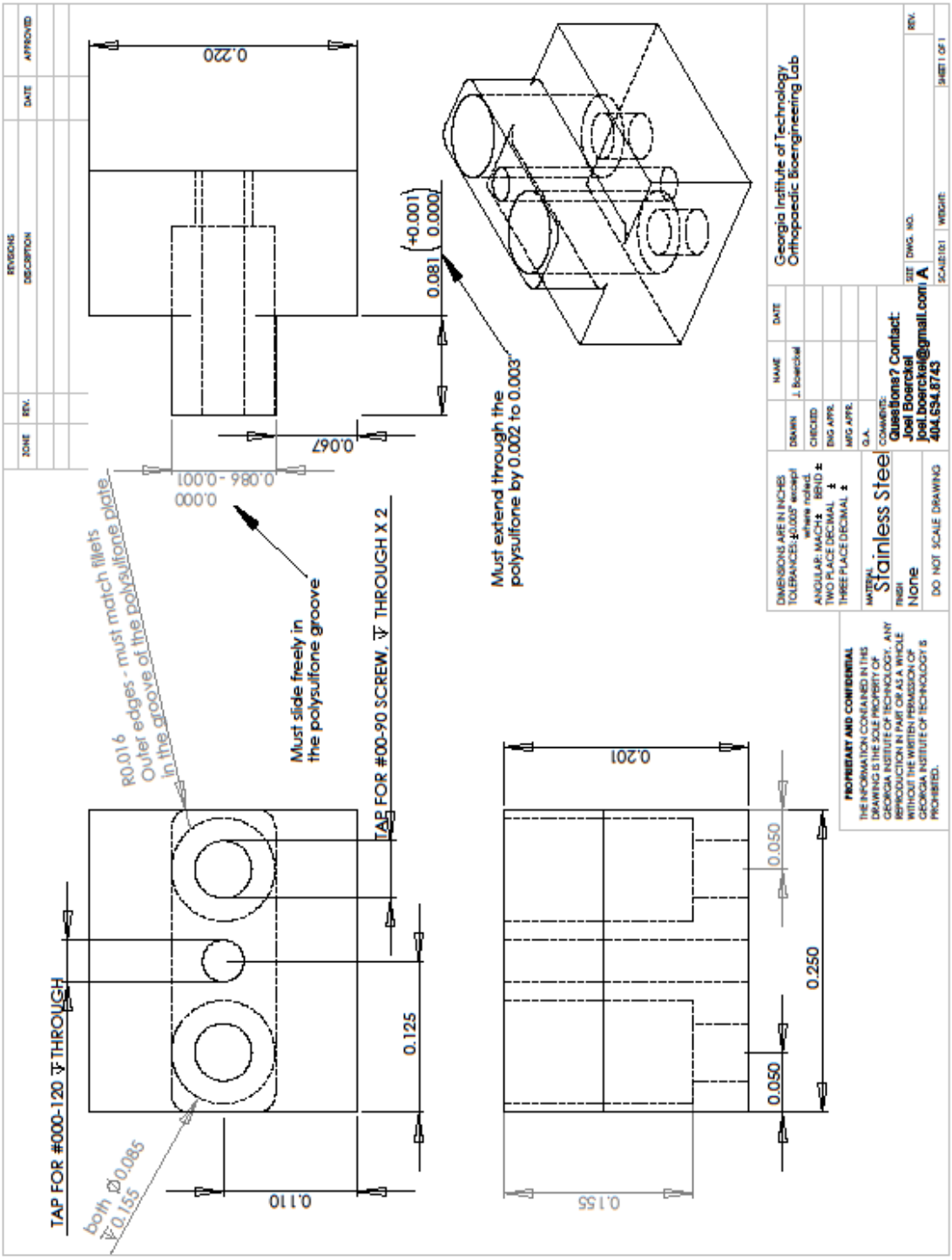

C.2.3 Top Plate

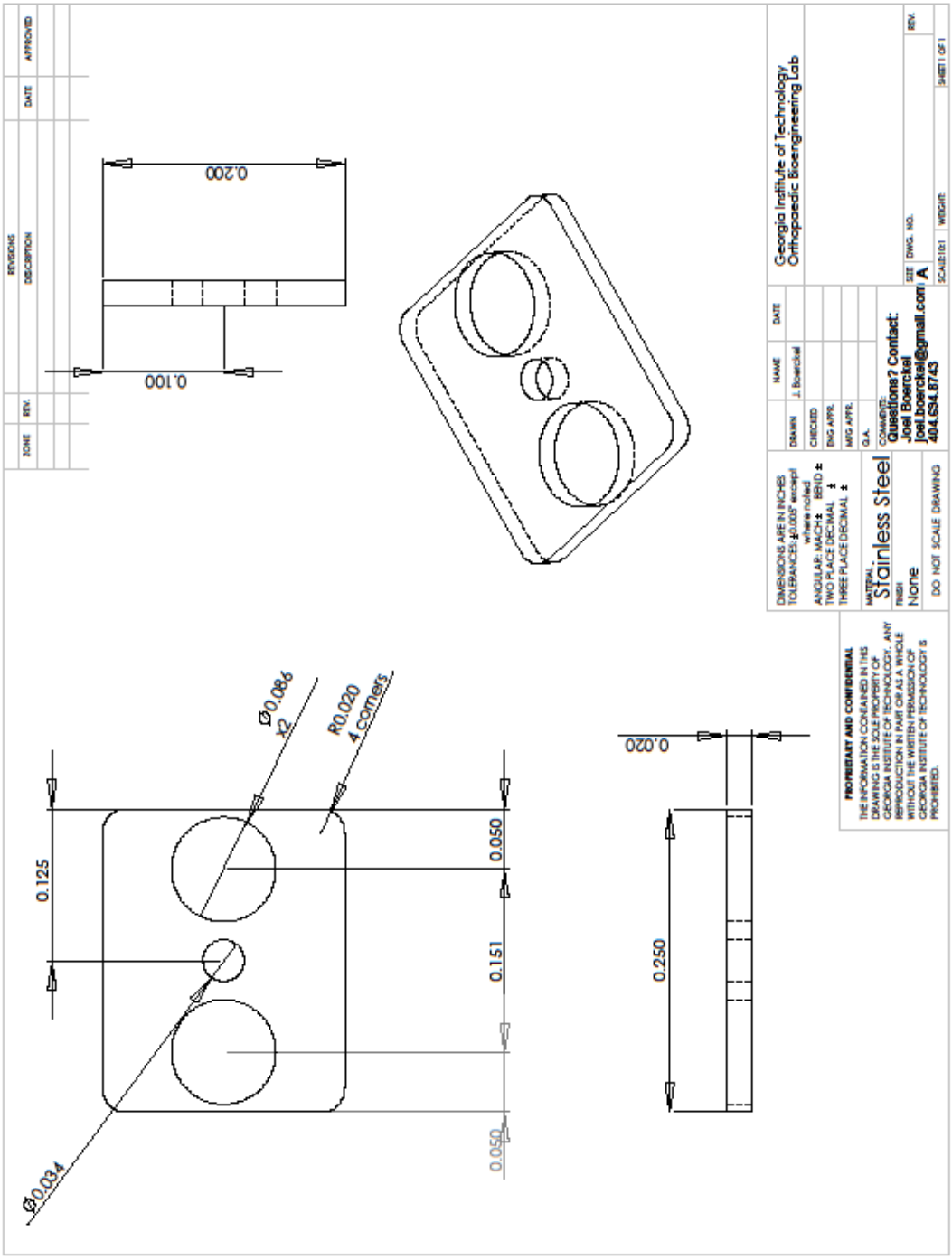

C.2.4 Rigid Clip

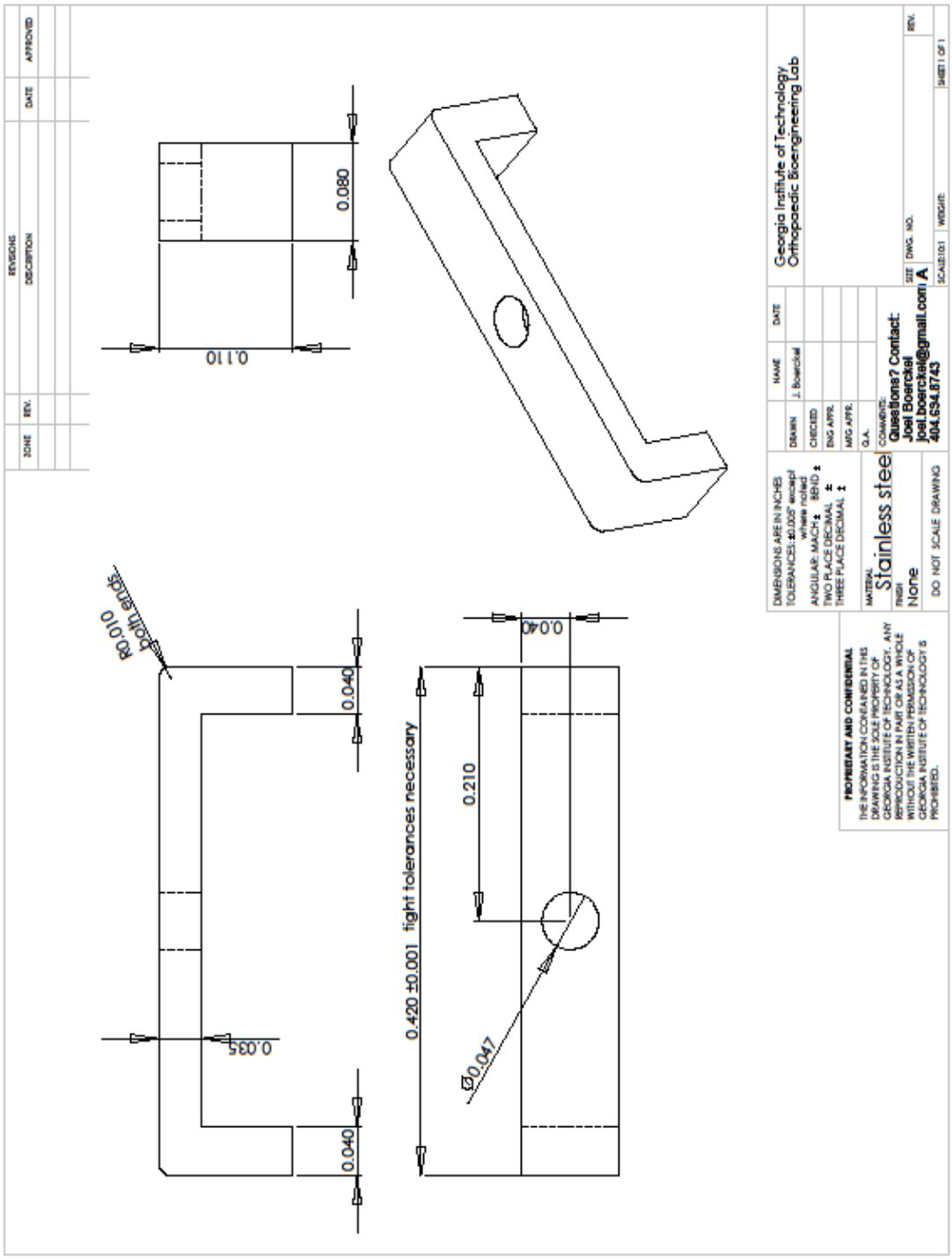

REFERENCES

1. Goodship, AE and Kenwright J. The influence of induced micromovement upon the healing of experimental tibial fractures. J Bone Joint Surg Br 1985;674:650-655.
2. Richards, M, Goulet JA, Weiss JA, Waanders NA, Schaffler MB, and Goldstein SA. Bone regeneration and fracture healing. Experience with distraction osteogenesis model. Clin Orthop Relat Res 1998;355 Suppl:S191-204.
3. Matsumoto, T, Yung YC, Fischbach C, Kong HJ, Nakaoka R, and Mooney DJ. Mechanical strain regulates endothelial cell patterning in vitro. Tissue Eng 2007;131:207-217.
4. Yung, YC, Chae J, Buehler MJ, Hunter CP, and Mooney DJ. Cyclic tensile strain triggers a sequence of autocrine and paracrine signaling to regulate angiogenic sprouting in human vascular cells. Proc Natl Acad Sci U S A 2009;10636:15279-15284.
5. Colnot, C, de la Fuente L, Huang S, Hu D, Lu C, St-Jacques B, et al. Indian hedgehog synchronizes skeletal angiogenesis and perichondrial maturation with cartilage development. Development 2005;1325:1057-1067.
6. Johnson, EE, Urist MR, and Finerman GA. Resistant nonunions and partial or complete segmental defects of long bones. Treatment with implants of a composite of human bone morphogenetic protein (BMP) and autolyzed, antigen-extracted, allogeneic (AAA) bone. Clin Orthop Relat Res 1992;277:229-237.
7. Woolf, AD and Pfleger B. Burden of major musculoskeletal conditions. Bull World Health Organ 2003;819:646-656.
8. Jones, AL, Bucholz RW, Bosse MJ, Mirza SK, Lyon TR, Webb LX, et al. Recombinant human BMP-2 and allograft compared with autogenous bone graft for reconstruction of diaphyseal tibial fractures with cortical defects. A randomized, controlled trial. J Bone Joint Surg Am 2006;887:1431-1441.
9. Sasso, RC, LeHuec JC, and Shaffrey C. Iliac crest bone graft donor site pain after anterior lumbar interbody fusion: a prospective patient satisfaction outcome assessment. J Spinal Disord Tech 2005;18 Suppl:S77-81.
10. Koefoed, M, Ito H, Gromov K, Reynolds DG, Awad HA, Rubery PT, et al. Biological effects of rAAV-caAlk2 coating on structural allograft healing. Mol Ther 2005;122:212-218.
11. Ignatius, A, Blessing H, Liedert A, Schmidt C, Neidlinger-Wilke C, Kaspar D, et al. Tissue engineering of bone: effects of mechanical strain on osteoblastic cells in type I collagen matrices. Biomaterials 2005;263:311-318.
12. Vance, J, Galley S, Liu DF, and Donahue SW. Mechanical stimulation of MC3T3 osteoblastic cells in a bone tissue-engineering bioreactor enhances prostaglandin E2 release. Tissue Eng 2005;1111-12:1832-1839.
13. Duty, AO, Oest ME, and Guldberg RE. Cyclic mechanical compression increases mineralization of cell-seeded polymer scaffolds in vivo. J Biomech Eng 2007;1294:531-539.

14. Kolambkar, YM, Dupont KM, Boerckel JD, Huebsch N, Mooney DJ, Hutmacher DW, et al. An alginate-based hybrid system for growth factor delivery in the functional repair of large bone defects. Biomaterials 2011;321:65-74.
15. Street, J, Bao M, deGuzman L, Bunting S, Peale FV, Jr., Ferrara N, et al. Vascular endothelial growth factor stimulates bone repair by promoting angiogenesis and bone turnover. Proc Natl Acad Sci U S A 2002;9915:9656-9661.
16. Rai, B, Oest ME, Dupont KM, Ho KH, Teoh SH, and Guldberg RE. Combination of platelet-rich plasma with polycaprolactone-tricalcium phosphate scaffolds for segmental bone defect repair. J Biomed Mater Res A 2007;814:888-899.
17. Cowin, SC, Bone mechanics handbook. 2nd ed. 2001, Boca Raton, FL: CRC Press.1 v. (various pagings).
18. Bilezikian, JP, Raisz LG, and Martin TJ, Principles of bone biology. 3rd ed. 2008, San Diego, Calif.: Academic Press/Elsevier.2 v. (xxiv, 1942, liv p. + 1922 p. of plates).
19. Asakura, A, Komaki M, and Rudnicki M. Muscle satellite cells are multipotential stem cells that exhibit myogenic, osteogenic, and adipogenic differentiation. Differentiation 2001;684-5:245-253.
20. Qi, H, Aguiar DJ, Williams SM, La Pean A, Pan W, and Verfaillie CM. Identification of genes responsible for osteoblast differentiation from human mesodermal progenitor cells. Proc Natl Acad Sci U S A 2003;1006:3305-3310.
21. Doherty, MJ, Ashton BA, Walsh S, Beresford JN, Grant ME, and Canfield AE. Vascular pericytes express osteogenic potential in vitro and in vivo. J Bone Miner Res 1998;135:828-838.
22. Kuznetsov, SA, Mankani MH, Gronthos S, Satomura K, Bianco P, and Robey PG. Circulating skeletal stem cells. J Cell Biol 2001;1535:1133-1140.
23. van der Plas, A and Nijweide PJ. Isolation and purification of osteocytes. J Bone Miner Res 1992;74:389-396.
24. Sikavitsas, VI, Temenoff JS, and Mikos AG. Biomaterials and bone mechanotransduction. Biomaterials 2001;2219:2581-2593.
25. Sikavitsas, VI, Temenoff JS, and Mikos AG. Biomaterials and bone mechanotransduction. Biomaterials 2001;2219:2581-2593.
26. Burger, EH, Klein-Nulend J, van der Plas A, and Nijweide PJ. Function of osteocytes in bone--their role in mechanotransduction. J Nutr 1995;1257 Suppl:2020S-2023S.
27. Mullender, MG and Huiskes R. Osteocytes and bone lining cells: which are the best candidates for mechano-sensors in cancellous bone? Bone 1997;206:527-532.
28. Young, MF. Bone matrix proteins: their function, regulation, and relationship to osteoporosis. Osteoporos Int 2003;14 Suppl 3:S35-42.
29. Kay, MI, Young RA, and Posner AS. Crystal Structure of Hydroxyapatite. Nature 1964;204:1050-1052.
30. Gravallese, EM. Osteopontin: a bridge between bone and the immune system. J Clin Invest 2003;1122:147-149.
31. Shapiro, F. Bone development and its relation to fracture repair. The role of mesenchymal osteoblasts and surface osteoblasts. Eur Cell Mater 2008;15:53-76.

32. Rubin, J, Rubin C, and Jacobs CR. Molecular pathways mediating mechanical signaling in bone. Gene 2006;367:1-16.
33. Jones, HH, Priest JD, Hayes WC, Tichenor CC, and Nagel DA. Humeral hypertrophy in response to exercise. J Bone Joint Surg Am 1977;592:204-208.
34. Haapasalo, H, Kontulainen S, Sievanen H, Kannus P, Jarvinen M, and Vuori I. Exercise-induced bone gain is due to enlargement in bone size without a change in volumetric bone density: a peripheral quantitative computed tomography study of the upper arms of male tennis players. Bone 2000;273:351-357.
35. Kontulainen, S, Sievanen H, Kannus P, Pasanen M, and Vuori I. Effect of long-term impact-loading on mass, size, and estimated strength of humerus and radius of female racquet-sports players: a peripheral quantitative computed tomography study between young and old starters and controls. J Bone Miner Res 2002;1712:2281-2289.
36. Frost, HM, Bone remodelling dynamics. The Henry Ford Hospital surgical monographs. 1963, Springfield, Ill.,: Thomas.175 p.
37. Robling, AG, Bellido T, and Turner CH. Mechanical stimulation in vivo reduces osteocyte expression of sclerostin. J Musculoskelet Neuronal Interact 2006;64:354.
38. Mackie, EJ. Osteoblasts: novel roles in orchestration of skeletal architecture. Int J Biochem Cell Biol 2003;359:1301-1305.
39. Knothe Tate, ML, Adamson JR, Tami AE, and Bauer TW. The osteocyte. Int J Biochem Cell Biol 2004;361:1-8.
40. Robling, AG, Castillo AB, and Turner CH. Biomechanical and molecular regulation of bone remodeling. Annu Rev Biomed Eng 2006;8:455-498.
41. Frost, HM. Bone "mass" and the "mechanostat": a proposal. Anat Rec 1987;2191:1-9.
42. Lanyon, LE and Rubin CT. Static vs dynamic loads as an influence on bone remodelling. J Biomech 1984;1712:897-905.
43. Rubin, CT and Lanyon LE. Regulation of bone formation by applied dynamic loads. J Bone Joint Surg Am 1984;663:397-402.
44. Rubin, CT and Lanyon LE. Regulation of bone mass by mechanical strain magnitude. Calcif Tissue Int 1985;374:411-417.
45. Turner, CH, Forwood MR, Rho JY, and Yoshikawa T. Mechanical loading thresholds for lamellar and woven bone formation. J Bone Miner Res 1994;91:87-97.
46. Turner, CH, Owan I, and Takano Y. Mechanotransduction in bone: role of strain rate. Am J Physiol 1995;2693 Pt 1:E438-442.
47. Turner, CH. Three rules for bone adaptation to mechanical stimuli. Bone 1998;235:399-407.
48. Carter, DR, Fyhrie DP, and Whalen RT. Trabecular bone density and loading history: regulation of connective tissue biology by mechanical energy. J Biomech 1987;208:785-794.
49. Lanyon, LE. The success and failure of the adaptive response to functional load-bearing in averting bone fracture. Bone 1992;13 Suppl 2:S17-21.
50. Fyhrie, DP and Schaffler MB. The adaptation of bone apparent density to applied load. J Biomech 1995;282:135-146.

51. Carmeliet, G, Vico L, and Bouillon R. Space flight: a challenge for normal bone homeostasis. Crit Rev Eukaryot Gene Expr 2001;111-3:131-144.
52. Duncan, RL and Turner CH. Mechanotransduction and the functional response of bone to mechanical strain. Calcif Tissue Int 1995;575:344-358.
53. Owan, I, Burr DB, Turner CH, Qiu J, Tu Y, Onyia JE, et al. Mechanotransduction in bone: osteoblasts are more responsive to fluid forces than mechanical strain. Am J Physiol 1997;2733 Pt 1:C810-815.
54. Smalt, R, Mitchell FT, Howard RL, and Chambers TJ. Induction of NO and prostaglandin E2 in osteoblasts by wall-shear stress but not mechanical strain. Am J Physiol 1997;2734 Pt 1:E751-758.
55. Price, C, Zhou X, Li W, and Wang L. Real-time measurement of solute transport within the lacunar-canalicular system of mechanically loaded bone: Direct evidence for load-induced fluid flow. J Bone Miner Res 2011;262:277-285.
56. Qin, YX, Lin W, and Rubin C. The pathway of bone fluid flow as defined by in vivo intramedullary pressure and streaming potential measurements. Ann Biomed Eng 2002;305:693-702.
57. Klein-Nulend, J, van der Plas A, Semeins CM, Ajubi NE, Frangos JA, Nijweide PJ, et al. Sensitivity of osteocytes to biomechanical stress in vitro. FASEB J 1995;95:441-445.
58. Cowin, SC, Weinbaum S, and Zeng Y. A case for bone canaliculi as the anatomical site of strain generated potentials. J Biomech 1995;2811:1281-1297.
59. Piekarski, K and Munro M. Transport mechanism operating between blood supply and osteocytes in long bones. Nature 1977;2695623:80-82.
60. Weinbaum, S, Cowin SC, and Zeng Y. A model for the excitation of osteocytes by mechanical loading-induced bone fluid shear stresses. J Biomech 1994;273:339-360.
61. Knothe Tate, ML, Knothe U, and Niederer P. Experimental elucidation of mechanical load-induced fluid flow and its potential role in bone metabolism and functional adaptation. Am J Med Sci 1998;3163:189-195.
62. Cowin, SC. Mechanosensation and fluid transport in living bone. J Musculoskelet Neuronal Interact 2002;23:256-260.
63. Han, Y, Cowin SC, Schaffler MB, and Weinbaum S. Mechanotransduction and strain amplification in osteocyte cell processes. Proc Natl Acad Sci U S A 2004;10147:16689-16694.
64. Turner, CH and Pavalko FM. Mechanotransduction and functional response of the skeleton to physical stress: the mechanisms and mechanics of bone adaptation. J Orthop Sci 1998;36:346-355.
65. Guharay, F and Sachs F. Stretch-activated single ion channel currents in tissue-cultured embryonic chick skeletal muscle. J Physiol 1984;352:685-701.
66. Sukharev, SI, Blount P, Martinac B, and Kung C. Mechanosensitive channels of Escherichia coli: the MscL gene, protein, and activities. Annu Rev Physiol 1997;59:633-657.
67. Ryder, KD and Duncan RL. Parathyroid hormone enhances fluid shear-induced [Ca2+]i signaling in osteoblastic cells through activation of mechanosensitive and voltage-sensitive Ca2+ channels. J Bone Miner Res 2001;162:240-248.

68. Saunders, MM, You J, Trosko JE, Yamasaki H, Li Z, Donahue HJ, et al. Gap junctions and fluid flow response in MC3T3-E1 cells. Am J Physiol Cell Physiol 2001;2816:C1917-1925.
69. Lu, X, Baik A, Chiang V, and Guo XE. Voltage-Sensitive Calcium Channels May Differentiate Intercellular Calcium Signaling between Osteocyte and Osteoblast Networks under Fluid Flow. In 57th Annual Meeting of the Orthopaedic Research Society. 2011. Long Beach, CA
70. Rezzonico, R, Cayatte C, Bourget-Ponzio I, Romey G, Belhacene N, Loubat A, et al. Focal adhesion kinase pp125FAK interacts with the large conductance calcium-activated hSlo potassium channel in human osteoblasts: potential role in mechanotransduction. J Bone Miner Res 2003;1810:1863-1871.
71. Wozniak, M, Fausto A, Carron CP, Meyer DM, and Hruska KA. Mechanically strained cells of the osteoblast lineage organize their extracellular matrix through unique sites of alphavbeta3-integrin expression. J Bone Miner Res 2000;159:1731-1745.
72. Whitfield, JF. The solitary (primary) cilium--a mechanosensory toggle switch in bone and cartilage cells. Cell Signal 2008;206:1019-1024.
73. Malone, AM, Anderson CT, Tummala P, Kwon RY, Johnston TR, Stearns T, et al. Primary cilia mediate mechanosensing in bone cells by a calcium-independent mechanism. Proc Natl Acad Sci U S A 2007;10433:13325-13330.
74. Rizzo, V, McIntosh DP, Oh P, and Schnitzer JE. In situ flow activates endothelial nitric oxide synthase in luminal caveolae of endothelium with rapid caveolin dissociation and calmodulin association. J Biol Chem 1998;27352:34724-34729.
75. Rizzo, V, Sung A, Oh P, and Schnitzer JE. Rapid mechanotransduction in situ at the luminal cell surface of vascular endothelium and its caveolae. J Biol Chem 1998;27341:26323-26329.
76. Kawamura, S, Miyamoto S, and Brown JH. Initiation and transduction of stretch-induced RhoA and Rac1 activation through caveolae: cytoskeletal regulation of ERK translocation. J Biol Chem 2003;27833:31111-31117.
77. Bonewald, LF and Johnson ML. Osteocytes, mechanosensing and Wnt signaling. Bone 2008;424:606-615.
78. Robinson, JA, Chatterjee-Kishore M, Yaworsky PJ, Cullen DM, Zhao W, Li C, et al. Wnt/beta-catenin signaling is a normal physiological response to mechanical loading in bone. J Biol Chem 2006;28142:31720-31728.
79. Mao, J, Wang J, Liu B, Pan W, Farr GH, 3rd, Flynn C, et al. Low-density lipoprotein receptor-related protein-5 binds to Axin and regulates the canonical Wnt signaling pathway. Mol Cell 2001;74:801-809.
80. Staal, FJ, Noort Mv M, Strous GJ, and Clevers HC. Wnt signals are transmitted through N-terminally dephosphorylated beta-catenin. EMBO Rep 2002;31:63-68.
81. Case, N, Ma M, Sen B, Xie Z, Gross TS, and Rubin J. Beta-catenin levels influence rapid mechanical responses in osteoblasts. J Biol Chem 2008;28343:29196-29205.
82. Norvell, SM, Alvarez M, Bidwell JP, and Pavalko FM. Fluid shear stress induces beta-catenin signaling in osteoblasts. Calcif Tissue Int 2004;755:396-404.

83. Santos, A, Bakker AD, Zandieh-Doulabi B, de Blieck-Hogervorst JM, and Klein-Nulend J. Early activation of the beta-catenin pathway in osteocytes is mediated by nitric oxide, phosphatidyl inositol-3 kinase/Akt, and focal adhesion kinase. Biochem Biophys Res Commun 2010;3911:364-369.
84. Sawakami, K, Robling AG, Ai M, Pitner ND, Liu D, Warden SJ, et al. The Wnt co-receptor LRP5 is essential for skeletal mechanotransduction but not for the anabolic bone response to parathyroid hormone treatment. J Biol Chem 2006;28133:23698-23711.
85. Habas, R, Kato Y, and He X. Wnt/Frizzled activation of Rho regulates vertebrate gastrulation and requires a novel Formin homology protein Daam1. Cell 2001;1077:843-854.
86. Kundu, AK, Khatiwala CB, and Putnam AJ. Extracellular matrix remodeling, integrin expression, and downstream signaling pathways influence the osteogenic differentiation of mesenchymal stem cells on poly(lactide-co-glycolide) substrates. Tissue Eng Part A 2009;152:273-283.
87. Alenghat, FJ, Tytell JD, Thodeti CK, Derrien A, and Ingber DE. Mechanical control of cAMP signaling through integrins is mediated by the heterotrimeric Galphas protein. J Cell Biochem 2009;1064:529-538.
88. Gardinier, JD, Majumdar S, Duncan RL, and Wang L. Cyclic Hydraulic Pressure and Fluid Flow Differentially Modulate Cytoskeleton Re-Organization in MC3T3 Osteoblasts. Cell Mol Bioeng 2009;21:133-143.
89. Pavalko, FM and Burridge K. Disruption of the actin cytoskeleton after microinjection of proteolytic fragments of alpha-actinin. J Cell Biol 1991;1143:481-491.
90. Yang, CM, Hsieh HL, Yao CC, Hsiao LD, Tseng CP, and Wu CB. Protein kinase C-delta transactivates platelet-derived growth factor receptor-alpha in mechanical strain-induced collagenase 3 (matrix metalloproteinase-13) expression by osteoblast-like cells. J Biol Chem 2009;28438:26040-26050.
91. Liu, D, Genetos DC, Shao Y, Geist DJ, Li J, Ke HZ, et al. Activation of extracellular-signal regulated kinase (ERK1/2) by fluid shear is Ca(2+)- and ATP-dependent in MC3T3-E1 osteoblasts. Bone 2008;424:644-652.
92. Chen, NX, Geist DJ, Genetos DC, Pavalko FM, and Duncan RL. Fluid shear-induced NFkappaB translocation in osteoblasts is mediated by intracellular calcium release. Bone 2003;333:399-410.
93. Rice, KM, Desai DH, Preston DL, Wehner PS, and Blough ER. Uniaxial stretch-induced regulation of mitogen-activated protein kinase, Akt and p70 S6 kinase in the ageing Fischer 344 x Brown Norway rat aorta. Exp Physiol 2007;925:963-970.
94. Cheng, M, Wu J, Li Y, Nie Y, and Chen H. Activation of MAPK participates in low shear stress-induced IL-8 gene expression in endothelial cells. Clin Biomech (Bristol, Avon) 2008;23 Suppl 1:S96-S103.
95. Herbenick, MA, Sprott D, Stills H, and Lawless M. Effects of a cyclooxygenase 2 inhibitor on fracture healing in a rat model. Am J Orthop (Belle Mead NJ) 2008;377:E133-137.

96. Gerstenfeld, LC, Cullinane DM, Barnes GL, Graves DT, and Einhorn TA. Fracture healing as a post-natal developmental process: molecular, spatial, and temporal aspects of its regulation. J Cell Biochem 2003;885:873-884.
97. Yu, YY, Lieu S, Lu C, and Colnot C. Bone morphogenetic protein 2 stimulates endochondral ossification by regulating periosteal cell fate during bone repair. Bone 2010;471:65-73.
98. Nakahara, H, Bruder SP, Haynesworth SE, Holecek JJ, Baber MA, Goldberg VM, et al. Bone and cartilage formation in diffusion chambers by subcultured cells derived from the periosteum. Bone 1990;113:181-188.
99. Urist, MR. Bone: formation by autoinduction. Science 1965;150698:893-899.
100. Jaiswal, N, Haynesworth SE, Caplan AI, and Bruder SP. Osteogenic differentiation of purified, culture-expanded human mesenchymal stem cells in vitro. J Cell Biochem 1997;642:295-312.
101. Dupont, KM, Sharma K, Stevens HY, Boerckel JD, Garcia AJ, and Guldberg RE. Human stem cell delivery for treatment of large segmental bone defects. Proc Natl Acad Sci U S A 2010;1078:3305-3310.
102. Cullinane, DM, Salisbury KT, Alkhiary Y, Eisenberg S, Gerstenfeld L, and Einhorn TA. Effects of the local mechanical environment on vertebrate tissue differentiation during repair: does repair recapitulate development? J Exp Biol 2003;206Pt 14:2459-2471.
103. Augat, P, Margevicius K, Simon J, Wolf S, Suger G, and Claes L. Local tissue properties in bone healing: influence of size and stability of the osteotomy gap. J Orthop Res 1998;164:475-481.
104. Wolf, S, Janousek A, Pfeil J, Veith W, Haas F, Duda G, et al. The effects of external mechanical stimulation on the healing of diaphyseal osteotomies fixed by flexible external fixation. Clin Biomech (Bristol, Avon) 1998;134-5:359-364.
105. Klein, P, Schell H, Streitparth F, Heller M, Kassi JP, Kandziora F, et al. The initial phase of fracture healing is specifically sensitive to mechanical conditions. J Orthop Res 2003;214:662-669.
106. Yamagishi, M and Yoshimura Y. The biomechanics of fracture healing. J Bone Joint Surg Am 1955;37-A5:1035-1068.
107. Kenwright, J, Richardson JB, Cunningham JL, White SH, Goodship AE, Adams MA, et al. Axial movement and tibial fractures. A controlled randomised trial of treatment. J Bone Joint Surg Br 1991;734:654-659.
108. Claes, LE, Heigele CA, Neidlinger-Wilke C, Kaspar D, Seidl W, Margevicius KJ, et al. Effects of mechanical factors on the fracture healing process. Clin Orthop Relat Res 1998;355 Suppl:S132-147.
109. Epari, DR, Taylor WR, Heller MO, and Duda GN. Mechanical conditions in the initial phase of bone healing. Clin Biomech (Bristol, Avon) 2006;216:646-655.
110. Epari, DR, Schell H, Bail HJ, and Duda GN. Instability prolongs the chondral phase during bone healing in sheep. Bone 2006;386:864-870.
111. Epari, DR, Kassi JP, Schell H, and Duda GN. Timely fracture-healing requires optimization of axial fixation stability. J Bone Joint Surg Am 2007;897:1575-1585.

112. Schell, H, Thompson MS, Bail HJ, Hoffmann JE, Schill A, Duda GN, et al. Mechanical induction of critically delayed bone healing in sheep: radiological and biomechanical results. J Biomech 2008;4114:3066-3072.
113. Claes, L, Veeser A, Gockelmann M, Simon U, and Ignatius A. A novel model to study metaphyseal bone healing under defined biomechanical conditions. Arch Orthop Trauma Surg 2009;1297:923-928.
114. Claes, L, Augat P, Schorlemmer S, Konrads C, Ignatius A, and Ehrnthaller C. Temporary distraction and compression of a diaphyseal osteotomy accelerates bone healing. J Orthop Res 2008;266:772-777.
115. Claes, LE, Wilke HJ, Augat P, Rubenacker S, and Margevicius KJ. Effect of dynamization on gap healing of diaphyseal fractures under external fixation. Clin Biomech (Bristol, Avon) 1995;105:227-234.
116. Claes, LE and Heigele CA. Magnitudes of local stress and strain along bony surfaces predict the course and type of fracture healing. J Biomech 1999;323:255-266.
117. Claes, L, Eckert-Hubner K, and Augat P. The effect of mechanical stability on local vascularization and tissue differentiation in callus healing. J Orthop Res 2002;205:1099-1105.
118. Park, SH, O'Connor K, McKellop H, and Sarmiento A. The influence of active shear or compressive motion on fracture-healing. J Bone Joint Surg Am 1998;806:868-878.
119. Augat, P, Merk J, Wolf S, and Claes L. Mechanical stimulation by external application of cyclic tensile strains does not effectively enhance bone healing. J Orthop Trauma 2001;151:54-60.
120. Augat, P, Burger J, Schorlemmer S, Henke T, Peraus M, and Claes L. Shear movement at the fracture site delays healing in a diaphyseal fracture model. J Orthop Res 2003;216:1011-1017.
121. Wolf, JW, Jr., White AA, 3rd, Panjabi MM, and Southwick WO. Comparison of cyclic loading versus constant compression in the treatment of long-bone fractures in rabbits. J Bone Joint Surg Am 1981;635:805-810.
122. Gardner, MJ, van der Meulen MC, Demetrakopoulos D, Wright TM, Myers ER, and Bostrom MP. In vivo cyclic axial compression affects bone healing in the mouse tibia. J Orthop Res 2006;248:1679-1686.
123. Yamaji, T, Ando K, Wolf S, Augat P, and Claes L. The effect of micromovement on callus formation. J Orthop Sci 2001;66:571-575.
124. Schell, H, Epari DR, Kassi JP, Bragulla H, Bail HJ, and Duda GN. The course of bone healing is influenced by the initial shear fixation stability. J Orthop Res 2005;235:1022-1028.
125. Rontgen, V, Blakytny R, Matthys R, Landauer M, Wehner T, Gockelmann M, et al. Fracture healing in mice under controlled rigid and flexible conditions using an adjustable external fixator. J Orthop Res 2010;2811:1456-1462.
126. Foxworthy, M and Pringle RM. Dynamization timing and its effect on bone healing when using the Orthofix Dynamic Axial Fixator. Injury 1995;262:117-119.
127. Claes, L, Ruter A, and Mayr E. Low-intensity ultrasound enhances maturation of callus after segmental transport. Clin Orthop Relat Res 2005;430:189-194.

128. Xie, L, Jacobson JM, Choi ES, Busa B, Donahue LR, Miller LM, et al. Low-level mechanical vibrations can influence bone resorption and bone formation in the growing skeleton. Bone 2006;395:1059-1066.
129. Goodship, AE, Lawes TJ, and Rubin CT. Low-magnitude high-frequency mechanical signals accelerate and augment endochondral bone repair: preliminary evidence of efficacy. J Orthop Res 2009;277:922-930.
130. Gilsanz, V, Wren TA, Sanchez M, Dorey F, Judex S, and Rubin C. Low-level, high-frequency mechanical signals enhance musculoskeletal development of young women with low BMD. J Bone Miner Res 2006;219:1464-1474.
131. Mosley, JR and Lanyon LE. Strain rate as a controlling influence on adaptive modeling in response to dynamic loading of the ulna in growing male rats. Bone 1998;234:313-318.
132. Sigurdsen, U, Reikeras O, and Utvag SE. The influence of compression on the healing of experimental tibial fractures. Injury 2010.
133. Kenwright, J and Albinana J. Problems encountered in leg shortening. J Bone Joint Surg Br 1991;734:671-675.
134. Ilizarov, GA. Clinical application of the tension-stress effect for limb lengthening. Clin Orthop Relat Res 1990;250:8-26.
135. Hente, R, Fuchtmeier B, Schlegel U, Ernstberger A, and Perren SM. The influence of cyclic compression and distraction on the healing of experimental tibial fractures. J Orthop Res 2004;224:709-715.
136. Ilizarov, GA. [Basic principles of transosseous compression and distraction osteosynthesis]. Ortop Travmatol Protez 1971;3211:7-15.
137. Jazrawi, LM, Majeska RJ, Klein ML, Kagel E, Stromberg L, and Einhorn TA. Bone and cartilage formation in an experimental model of distraction osteogenesis. J Orthop Trauma 1998;122:111-116.
138. Ilizarov, GA. The principles of the Ilizarov method. 1988. Bull Hosp Jt Dis 1997;561:49-53.
139. Smith-Adaline, EA, Volkman SK, Ignelzi MA, Jr., Slade J, Platte S, and Goldstein SA. Mechanical environment alters tissue formation patterns during fracture repair. J Orthop Res 2004;225:1079-1085.
140. Palomares, KT, Gleason RE, Mason ZD, Cullinane DM, Einhorn TA, Gerstenfeld LC, et al. Mechanical stimulation alters tissue differentiation and molecular expression during bone healing. J Orthop Res 2009;279:1123-1132.
141. Pauwels, F, Biomechanics of the locomotor apparatus : contributions on the functional anatomy of the locomotor apparatus. 1980, Berlin ; New York: Springer-Verlag.viii, 518 p.
142. Epari, DR, Lienau J, Schell H, Witt F, and Duda GN. Pressure, oxygen tension and temperature in the periosteal callus during bone healing--an in vivo study in sheep. Bone 2008;434:734-739.
143. Ilizarov, GA. The tension-stress effect on the genesis and growth of tissues: Part II. The influence of the rate and frequency of distraction. Clin Orthop Relat Res 1989;239:263-285.
144. Kojimoto, H, Yasui N, Goto T, Matsuda S, and Shimomura Y. Bone lengthening in rabbits by callus distraction. The role of periosteum and endosteum. J Bone Joint Surg Br 1988;704:543-549.

145. Ilizarov, GA, Devyatov AA, and Kamerin VK. Plastic reconstruction of longitudinal bone defects by means of compression and subsequent distraction. Acta Chir Plast 1980;221:32-41.
146. Carter, DR, Beaupre GS, Giori NJ, and Helms JA. Mechanobiology of skeletal regeneration. Clin Orthop Relat Res 1998;355 Suppl:S41-55.
147. Perren, SM. Physical and biological aspects of fracture healing with special reference to internal fixation. Clin Orthop Relat Res 1979;138:175-196.
148. Perren, SM, Cordey, J., ed. The Concept of Interfragmentary Strain. Current Concepts in Internal Fixation of Fractures. 1980.
149. Lienau, J, Schell H, Duda GN, Seebeck P, Muchow S, and Bail HJ. Initial vascularization and tissue differentiation are influenced by fixation stability. J Orthop Res 2005;233:639-645.
150. Laurencin, CT and Khan Y. Bone Graft Subsititutes. 2006 12/3/2009 [cited 2011 2/10/2011]; Available from: http://emedicine.medscape.com/article/1230616-overview.
151. Cypher, TJ and Grossman JP. Biological principles of bone graft healing. J Foot Ankle Surg 1996;355:413-417.
152. Berrey, BH, Jr., Lord CF, Gebhardt MC, and Mankin HJ. Fractures of allografts. Frequency, treatment, and end-results. J Bone Joint Surg Am 1990;726:825-833.
153. Zabka, AG, Pluhar GE, Edwards RB, 3rd, Manley PA, Hayashi K, Heiner JP, et al. Histomorphometric description of allograft bone remodeling and union in a canine segmental femoral defect model: a comparison of rhBMP-2, cancellous bone graft, and absorbable collagen sponge. J Orthop Res 2001;192:318-327.
154. Ito, H, Koefoed M, Tiyapatanaputi P, Gromov K, Goater JJ, Carmouche J, et al. Remodeling of cortical bone allografts mediated by adherent rAAV-RANKL and VEGF gene therapy. Nat Med 2005;113:291-297.
155. Boyce, T, Edwards J, and Scarborough N. Allograft bone. The influence of processing on safety and performance. Orthop Clin North Am 1999;304:571-581.
156. Update: allograft-associated bacterial infections--United States, 2002. MMWR Morb Mortal Wkly Rep 2002;5110:207-210.
157. Lieberman, JR, Daluiski A, and Einhorn TA. The role of growth factors in the repair of bone. Biology and clinical applications. J Bone Joint Surg Am 2002;84-A6:1032-1044.
158. Guldberg, RE, Boerckel J.D., Dupont K.M., Johnson M.R., Lin A.S.P., Oest M.E., Peister A., O'Keefe R.J., ed. "Translational Approaches for Engineering Bone Repair". Translational Approaches in Tissue Engineering and Regenerative Medicine, ed. J. Mao, Vunjak-Novakovic, G., Mikos, A., Atala, A. 2008, Artech House.125-144.
159. Shen, X, Wan C, Ramaswamy G, Mavalli M, Wang Y, Duvall CL, et al. Prolyl hydroxylase inhibitors increase neoangiogenesis and callus formation following femur fracture in mice. J Orthop Res 2009.
160. Wan, C, Gilbert SR, Wang Y, Cao X, Shen X, Ramaswamy G, et al. Activation of the hypoxia-inducible factor-1alpha pathway accelerates bone regeneration. Proc Natl Acad Sci U S A 2008;1052:686-691.
161. Kimelman-Bleich, N, Pelled G, Zilberman Y, Kallai I, Mizrahi O, Tawackoli W, et al. Targeted gene-and-host progenitor cell therapy for nonunion bone fracture repair. Mol Ther 2011;191:53-59.

162. Dupont, K, Stevens H, Boerckel J, Diab T, Takahata M, Schwarz E, et al. Synthetic Scaffold Functionalization by Adeno-Associated Virus Encoding BMP2 for Orthotopic Bone Defect Repair. In 56th Annual Meeting of the Orthopaedic Research Society. 2010. New Orleans, LA

163. Peister, A, Deutsch ER, Kolambkar Y, Hutmacher DW, and Guldberg RE. Amniotic fluid stem cells produce robust mineral deposits on biodegradable scaffolds. Tissue Eng Part A 2009;1510:3129-3138.
164. Kolambkar, YM, Peister A, Ekaputra AK, Hutmacher DW, and Guldberg RE. Colonization and osteogenic differentiation of different stem cell sources on electrospun nanofiber meshes. Tissue Eng Part A 2010;1610:3219-3230.
165. Seeherman, H, Wozney J, and Li R. Bone morphogenetic protein delivery systems. Spine (Phila Pa 1976) 2002;2716 Suppl 1:S16-23.
166. Riley, EH, Lane JM, Urist MR, Lyons KM, and Lieberman JR. Bone morphogenetic protein-2: biology and applications. Clin Orthop Relat Res 1996;324:39-46.
167. Sampath, TK, Muthukumaran N, and Reddi AH. Isolation of osteogenin, an extracellular matrix-associated, bone-inductive protein, by heparin affinity chromatography. Proc Natl Acad Sci U S A 1987;8420:7109-7113.
168. Luu, HH, Song WX, Luo X, Manning D, Luo J, Deng ZL, et al. Distinct roles of bone morphogenetic proteins in osteogenic differentiation of mesenchymal stem cells. J Orthop Res 2007;255:665-677.
169. Cheng, H, Jiang W, Phillips FM, Haydon RC, Peng Y, Zhou L, et al. Osteogenic activity of the fourteen types of human bone morphogenetic proteins (BMPs). J Bone Joint Surg Am 2003;85-A8:1544-1552.
170. Kang, Q, Sun MH, Cheng H, Peng Y, Montag AG, Deyrup AT, et al. Characterization of the distinct orthotopic bone-forming activity of 14 BMPs using recombinant adenovirus-mediated gene delivery. Gene Ther 2004;1117:1312-1320.
171. Wozney, JM, Rosen V, Celeste AJ, Mitsock LM, Whitters MJ, Kriz RW, et al. Novel regulators of bone formation: molecular clones and activities. Science 1988;2424885:1528-1534.
172. Reddi, AH. BMPs: from bone morphogenetic proteins to body morphogenetic proteins. Cytokine Growth Factor Rev 2005;163:249-250.
173. Bessa, PC, Casal M, and Reis RL. Bone morphogenetic proteins in tissue engineering: the road from laboratory to clinic, part II (BMP delivery). J Tissue Eng Regen Med 2008;22-3:81-96.
174. Reddi, AH. Cartilage-derived morphogenetic proteins and cartilage morphogenesis. Microsc Res Tech 1998;432:131-136.
175. Bessa, PC, Casal M, and Reis RL. Bone morphogenetic proteins in tissue engineering: the road from the laboratory to the clinic, part I (basic concepts). J Tissue Eng Regen Med 2008;21:1-13.
176. Derynck, R and Zhang YE. Smad-dependent and Smad-independent pathways in TGF-beta family signalling. Nature 2003;4256958:577-584.

177. Nakao, A, Afrakhte M, Moren A, Nakayama T, Christian JL, Heuchel R, et al. Identification of Smad7, a TGFbeta-inducible antagonist of TGF-beta signalling. Nature 1997;3896651:631-635.
178. Shi, Y and Massague J. Mechanisms of TGF-beta signaling from cell membrane to the nucleus. Cell 2003;1136:685-700.
179. Miyazono, K, Maeda S, and Imamura T. Coordinate regulation of cell growth and differentiation by TGF-beta superfamily and Runx proteins. Oncogene 2004;2324:4232-4237.
180. Maeda, S, Hayashi M, Komiya S, Imamura T, and Miyazono K. Endogenous TGF-beta signaling suppresses maturation of osteoblastic mesenchymal cells. EMBO J 2004;233:552-563.
181. Zhang, YW, Yasui N, Ito K, Huang G, Fujii M, Hanai J, et al. A RUNX2/PEBP2alpha A/CBFA1 mutation displaying impaired transactivation and Smad interaction in cleidocranial dysplasia. Proc Natl Acad Sci U S A 2000;9719:10549-10554.
182. Einhorn, TA. Clinical applications of recombinant human BMPs: early experience and future development. J Bone Joint Surg Am 2003;85-A Suppl 3:82-88.
183. Swiontkowski, MF, Aro HT, Donell S, Esterhai JL, Goulet J, Jones A, et al. Recombinant human bone morphogenetic protein-2 in open tibial fractures. A subgroup analysis of data combined from two prospective randomized studies. J Bone Joint Surg Am 2006;886:1258-1265.
184. Liao, SS and Cui FZ. In vitro and in vivo degradation of mineralized collagen-based composite scaffold: nanohydroxyapatite/collagen/poly(L-lactide). Tissue Eng 2004;101-2:73-80.
185. Huang, Q, Goh JC, Hutmacher DW, and Lee EH. In vivo mesenchymal cell recruitment by a scaffold loaded with transforming growth factor beta1 and the potential for in situ chondrogenesis. Tissue Eng 2002;83:469-482.
186. Jiang, T, Abdel-Fattah WI, and Laurencin CT. In vitro evaluation of chitosan/poly(lactic acid-glycolic acid) sintered microsphere scaffolds for bone tissue engineering. Biomaterials 2006;2728:4894-4903.
187. VandeVord, PJ, Matthew HW, DeSilva SP, Mayton L, Wu B, and Wooley PH. Evaluation of the biocompatibility of a chitosan scaffold in mice. J Biomed Mater Res 2002;593:585-590.
188. Meinel, L, Betz O, Fajardo R, Hofmann S, Nazarian A, Cory E, et al. Silk based biomaterials to heal critical sized femur defects. Bone 2006;394:922-931.
189. Wang, Y, Kim HJ, Vunjak-Novakovic G, and Kaplan DL. Stem cell-based tissue engineering with silk biomaterials. Biomaterials 2006;2736:6064-6082.
190. Eppley, BL, Pietrzak WS, and Blanton MW. Allograft and alloplastic bone substitutes: a review of science and technology for the craniomaxillofacial surgeon. J Craniofac Surg 2005;166:981-989.
191. Minamide, A, Yoshida M, Kawakami M, Yamasaki S, Kojima H, Hashizume H, et al. The use of cultured bone marrow cells in type I collagen gel and porous hydroxyapatite for posterolateral lumbar spine fusion. Spine 2005;3010:1134-1138.

192. Behravesh, E, Yasko AW, Engel PS, and Mikos AG. Synthetic biodegradable polymers for orthopaedic applications. Clin Orthop Relat Res 1999;367 Suppl:S118-129.
193. Garcia, AJ and Reyes CD. Bio-adhesive surfaces to promote osteoblast differentiation and bone formation. J Dent Res 2005;845:407-413.
194. Keselowsky, BG, Collard DM, and Garcia AJ. Surface chemistry modulates fibronectin conformation and directs integrin binding and specificity to control cell adhesion. J Biomed Mater Res A 2003;662:247-259.
195. Ambrose, CG and Clanton TO. Bioabsorbable implants: review of clinical experience in orthopedic surgery. Ann Biomed Eng 2004;321:171-177.
196. Chong, AK and Chang J. Tissue engineering for the hand surgeon: a clinical perspective. J Hand Surg [Am] 2006;313:349-358.
197. Martin, C, Winet H, and Bao JY. Acidity near eroding polylactide-polyglycolide in vitro and in vivo in rabbit tibial bone chambers. Biomaterials 1996;1724:2373-2380.
198. Rai, B, Oest ME, Dupont KM, Ho KH, Teoh SH, and Guldberg RE. Combination of platelet-rich plasma with polycaprolactone-tricalcium phosphate scaffolds for segmental bone defect repair. J Biomed Mater Res A 2007.
199. Peter, SJ, Kim P, Yasko AW, Yaszemski MJ, and Mikos AG. Crosslinking characteristics of an injectable poly(propylene fumarate)/beta-tricalcium phosphate paste and mechanical properties of the crosslinked composite for use as a biodegradable bone cement. J Biomed Mater Res 1999;443:314-321.
200. Temenoff, JS and Mikos AG. Injectable biodegradable materials for orthopedic tissue engineering. Biomaterials 2000;2123:2405-2412.
201. Lobel, KD and Hench LL. In vitro adsorption and activity of enzymes on reaction layers of bioactive glass substrates. J Biomed Mater Res 1998;394:575-579.
202. Keshaw, H, Forbes A, and Day RM. Release of angiogenic growth factors from cells encapsulated in alginate beads with bioactive glass. Biomaterials 2005;2619:4171-4179.
203. Lu, HH, Tang A, Oh SC, Spalazzi JP, and Dionisio K. Compositional effects on the formation of a calcium phosphate layer and the response of osteoblast-like cells on polymer-bioactive glass composites. Biomaterials 2005;2632:6323-6334.
204. Roether, JA, Gough JE, Boccaccini AR, Hench LL, Maquet V, and Jerome R. Novel bioresorbable and bioactive composites based on bioactive glass and polylactide foams for bone tissue engineering. J Mater Sci Mater Med 2002;1312:1207-1214.
205. Rezwan, K, Chen QZ, Blaker JJ, and Boccaccini AR. Biodegradable and bioactive porous polymer/inorganic composite scaffolds for bone tissue engineering. Biomaterials 2006;2718:3413-3431.
206. Hench, LL, Xynos ID, and Polak JM. Bioactive glasses for in situ tissue regeneration. J Biomater Sci Polym Ed 2004;154:543-562.
207. Hinz, P, Wolf E, Schwesinger G, Hartelt E, and Ekkernkamp A. A new resorbable bone void filler in trauma: early clinical experience and histologic evaluation. Orthopedics 2002;255 Suppl:s597-600.

208. Mahr, MA, Bartley GB, Bite U, Clay RP, Kasperbauer JL, and Holmes JM. Norian craniofacial repair system bone cement for the repair of craniofacial skeletal defects. Ophthal Plast Reconstr Surg 2000;165:393-398.
209. Kang, XQ, Zang WJ, Bao LJ, Li DL, Xu XL, and Yu XJ. Differentiating characterization of human umbilical cord blood-derived mesenchymal stem cells in vitro. Cell Biol Int 2006;307:569-575.
210. Woodard, JR, Hilldore AJ, Lan SK, Park CJ, Morgan AW, Eurell JA, et al. The mechanical properties and osteoconductivity of hydroxyapatite bone scaffolds with multi-scale porosity. Biomaterials 2007;281:45-54.
211. Boden, SD, Martin GJ, Jr., Morone M, Ugbo JL, Titus L, and Hutton WC. The use of coralline hydroxyapatite with bone marrow, autogenous bone graft, or osteoinductive bone protein extract for posterolateral lumbar spine fusion. Spine 1999;244:320-327.
212. Giannoudis, PV, Dinopoulos H, and Tsiridis E. Bone substitutes: an update. Injury 2005;36 Suppl 3:S20-27.
213. Kruyt, MC, Wilson CE, de Bruijn JD, van Blitterswijk CA, Oner CF, Verbout AJ, et al. The effect of cell-based bone tissue engineering in a goat transverse process model. Biomaterials 2006;2729:5099-5106.
214. Sendemir-Urkmez, A and Jamison RD. The addition of biphasic calcium phosphate to porous chitosan scaffolds enhances bone tissue development in vitro. J Biomed Mater Res A 2006.
215. Lickorish, D, Guan L, and Davies JE. A three-phase, fully resorbable, polyester/calcium phosphate scaffold for bone tissue engineering: Evolution of scaffold design. Biomaterials 2006.
216. Zhou, Y, Chen F, Ho ST, Woodruff MA, Lim TM, and Hutmacher DW. Combined marrow stromal cell-sheet techniques and high-strength biodegradable composite scaffolds for engineered functional bone grafts. Biomaterials 2007;285:814-824.
217. Meretoja, VV, Helminen AO, Korventausta JJ, Haapa-aho V, Seppala JV, and Narhi TO. Crosslinked poly(epsilon-caprolactone/D,L-lactide)/bioactive glass composite scaffolds for bone tissue engineering. J Biomed Mater Res A 2006;772:261-268.
218. Kim, SS, Sun Park M, Jeon O, Yong Choi C, and Kim BS. Poly(lactide-co-glycolide)/hydroxyapatite composite scaffolds for bone tissue engineering. Biomaterials 2006;278:1399-1409.
219. Mehta, G, Williams CM, Alvarez L, Lesniewski M, Kamm RD, and Griffith LG. Synergistic effects of tethered growth factors and adhesion ligands on DNA synthesis and function of primary hepatocytes cultured on soft synthetic hydrogels. Biomaterials 2010;3117:4657-4671.
220. Platt, MO, Roman AJ, Wells A, Lauffenburger DA, and Griffith LG. Sustained epidermal growth factor receptor levels and activation by tethered ligand binding enhances osteogenic differentiation of multi-potent marrow stromal cells. J Cell Physiol 2009;2212:306-317.
221. Fan, VH, Tamama K, Au A, Littrell R, Richardson LB, Wright JW, et al. Tethered epidermal growth factor provides a survival advantage to mesenchymal stem cells. Stem Cells 2007;255:1241-1251.

222. Phelps, EA, Landazuri N, Thule PM, Taylor WR, and Garcia AJ. Bioartificial matrices for therapeutic vascularization. Proc Natl Acad Sci U S A 2010;1078:3323-3328.
223. Patterson, J, Siew R, Herring SW, Lin AS, Guldberg R, and Stayton PS. Hyaluronic acid hydrogels with controlled degradation properties for oriented bone regeneration. Biomaterials 2010;3126:6772-6781.
224. Simmons, CA, Alsberg E, Hsiong S, Kim WJ, and Mooney DJ. Dual growth factor delivery and controlled scaffold degradation enhance in vivo bone formation by transplanted bone marrow stromal cells. Bone 2004;352:562-569.
225. Kempen, DH, Yaszemski MJ, Heijink A, Hefferan TE, Creemers LB, Britson J, et al. Non-invasive monitoring of BMP-2 retention and bone formation in composites for bone tissue engineering using SPECT/CT and scintillation probes. J Control Release 2009;1343:169-176.
226. Rowley, JA, Madlambayan G, and Mooney DJ. Alginate hydrogels as synthetic extracellular matrix materials. Biomaterials 1999;201:45-53.
227. Alsberg, E, Anderson KW, Albeiruti A, Franceschi RT, and Mooney DJ. Cell-interactive alginate hydrogels for bone tissue engineering. J Dent Res 2001;8011:2025-2029.
228. Kolambkar YM, D, K.M, Mooney, D.J, Hutmacher, D.W., Guldberg, R.E. Effect of Nanofiber Mesh Design on BMP-mediated Segmental Bone Defect Repair In 55th Annual Meeting of the Orthopaedic Research Society. 2009. Las Vegas, Nevada.
229. Bakker, AD, Soejima K, Klein-Nulend J, and Burger EH. The production of nitric oxide and prostaglandin E(2) by primary bone cells is shear stress dependent. J Biomech 2001;345:671-677.
230. Vezeridis, PS, Semeins CM, Chen Q, and Klein-Nulend J. Osteocytes subjected to pulsating fluid flow regulate osteoblast proliferation and differentiation. Biochem Biophys Res Commun 2006;3483:1082-1088.
231. Tanaka, SM, Li J, Duncan RL, Yokota H, Burr DB, and Turner CH. Effects of broad frequency vibration on cultured osteoblasts. J Biomech 2003;361:73-80.
232. Rath, B, Nam J, Knobloch TJ, Lannutti JJ, and Agarwal S. Compressive forces induce osteogenic gene expression in calvarial osteoblasts. J Biomech 2008;415:1095-1103.
233. Takai, E, Mauck RL, Hung CT, and Guo XE. Osteocyte viability and regulation of osteoblast function in a 3D trabecular bone explant under dynamic hydrostatic pressure. J Bone Miner Res 2004;199:1403-1410.
234. Trepczik, B, Lienau J, Schell H, Epari DR, Thompson MS, Hoffmann JE, et al. Endochondral ossification in vitro is influenced by mechanical bending. Bone 2007;403:597-603.
235. Cartmell, SH, Porter BD, Garcia AJ, and Guldberg RE. Effects of medium perfusion rate on cell-seeded three-dimensional bone constructs in vitro. Tissue Eng 2003;96:1197-1203.
236. Mauney, JR, Sjostorm S, Blumberg J, Horan R, O'Leary JP, Vunjak-Novakovic G, et al. Mechanical stimulation promotes osteogenic differentiation of human bone marrow stromal cells on 3-D partially demineralized bone scaffolds in vitro. Calcif Tissue Int 2004;745:458-468.

237. Byrne, EM, Farrell E, McMahon LA, Haugh MG, O'Brien FJ, Campbell VA, et al. Gene expression by marrow stromal cells in a porous collagen-glycosaminoglycan scaffold is affected by pore size and mechanical stimulation. J Mater Sci Mater Med 2008;1911:3455-3463.
238. Tanaka, SM, Sun HB, Roeder RK, Burr DB, Turner CH, and Yokota H. Osteoblast responses one hour after load-induced fluid flow in a three-dimensional porous matrix. Calcif Tissue Int 2005;764:261-271.
239. Matziolis, G, Tuischer J, Kasper G, Thompson M, Bartmeyer B, Krocker D, et al. Simulation of cell differentiation in fracture healing: mechanically loaded composite scaffolds in a novel bioreactor system. Tissue Eng 2006;121:201-208.
240. Rutherford, RB, Vascular surgery. 6th ed. 2005, Philadelphia: Saunders.
241. Carmeliet, P. Mechanisms of angiogenesis and arteriogenesis. Nat Med 2000;64:389-395.
242. Scholz, D, Ziegelhoeffer T, Helisch A, Wagner S, Friedrich C, Podzuweit T, et al. Contribution of arteriogenesis and angiogenesis to postocclusive hindlimb perfusion in mice. J Mol Cell Cardiol 2002;347:775-787.
243. Wang, Y, Wan C, Deng L, Liu X, Cao X, Gilbert SR, et al. The hypoxia-inducible factor alpha pathway couples angiogenesis to osteogenesis during skeletal development. J Clin Invest 2007;1176:1616-1626.
244. Gerber, HP, Vu TH, Ryan AM, Kowalski J, Werb Z, and Ferrara N. VEGF couples hypertrophic cartilage remodeling, ossification and angiogenesis during endochondral bone formation. Nat Med 1999;56:623-628.
245. Carlevaro, MF, Cermelli S, Cancedda R, and Descalzi Cancedda F. Vascular endothelial growth factor (VEGF) in cartilage neovascularization and chondrocyte differentiation: auto-paracrine role during endochondral bone formation. J Cell Sci 2000;113 (Pt 1):59-69.
246. Hausman, MR, Schaffler MB, and Majeska RJ. Prevention of fracture healing in rats by an inhibitor of angiogenesis. Bone 2001;296:560-564.
247. Perren, SM, Cordey, J., The Concept of Interfragmentary Strain. Current concepts of internal fixation of fractures, ed. H.K. Uhthoff and E. Stahl. 1980, Berlin ; New York: Springer-Verlag.ix, 452 p.
248. Lu, C, Hansen E, Sapozhnikova A, Hu D, Miclau T, and Marcucio RS. Effect of age on vascularization during fracture repair. J Orthop Res 2008;2610:1384-1389.
249. Taylor, DK, Meganck JA, Terkhorn S, Rajani R, Naik A, O'Keefe RJ, et al. Thrombospondin-2 Influences the Proportion of Cartilage and Bone During Fracture Healing. J Bone Miner Res 2009.
250. Wallace, AL, Draper ER, Strachan RK, McCarthy ID, and Hughes SP. The vascular response to fracture micromovement. Clin Orthop Relat Res 1994;301:281-290.
251. Lienau, J, Schmidt-Bleek K, Peters A, Haschke F, Duda GN, Perka C, et al. Differential regulation of blood vessel formation between standard and delayed bone healing. J Orthop Res 2009.
252. Rihn, JA, Kirkpatrick K, and Albert TJ. Graft options in posterolateral and posterior interbody lumbar fusion. Spine (Phila Pa 1976) 2010;3517:1629-1639.

253. Zhang, X, Awad HA, O'Keefe RJ, Guldberg RE, and Schwarz EM. A perspective: engineering periosteum for structural bone graft healing. Clin Orthop Relat Res 2008;4668:1777-1787.
254. Guldberg, RE. Spatiotemporal delivery strategies for promoting musculoskeletal tissue regeneration. J Bone Miner Res 2009;249:1507-1511.
255. Langer, R and Folkman J. Polymers for the sustained release of proteins and other macromolecules. Nature 1976;2635580:797-800.
256. Sampath, TK and Reddi AH. Homology of bone-inductive proteins from human, monkey, bovine, and rat extracellular matrix. Proc Natl Acad Sci U S A 1983;8021:6591-6595.
257. Sampath, TK and Reddi AH. Dissociative extraction and reconstitution of extracellular matrix components involved in local bone differentiation. Proc Natl Acad Sci U S A 1981;7812:7599-7603.
258. Urist, MR and Strates BS. Bone morphogenetic protein. J Dent Res 1971;506:1392-1406.
259. Urist, MR, Mikulski A, and Lietze A. Solubilized and insolubilized bone morphogenetic protein. Proc Natl Acad Sci U S A 1979;764:1828-1832.
260. Ebara, S and Nakayama K. Mechanism for the action of bone morphogenetic proteins and regulation of their activity. Spine (Phila Pa 1976) 2002;2716 Suppl 1:S10-15.
261. Minear, S, Leucht P, Miller S, and Helms JA. rBMP represses Wnt signaling and influences skeletal progenitor cell fate specification during bone repair. J Bone Miner Res 2010;256:1196-1207.
262. Boden, SD, Kang J, Sandhu H, and Heller JG. Use of recombinant human bone morphogenetic protein-2 to achieve posterolateral lumbar spine fusion in humans: a prospective, randomized clinical pilot trial: 2002 Volvo Award in clinical studies. Spine (Phila Pa 1976) 2002;2723:2662-2673.
263. McKay, B and Sandhu HS. Use of recombinant human bone morphogenetic protein-2 in spinal fusion applications. Spine (Phila Pa 1976) 2002;2716 Suppl 1:S66-85.
264. Johnsson, R, Stromqvist B, and Aspenberg P. Randomized radiostereometric study comparing osteogenic protein-1 (BMP-7) and autograft bone in human noninstrumented posterolateral lumbar fusion: 2002 Volvo Award in clinical studies. Spine (Phila Pa 1976) 2002;2723:2654-2661.
265. Vaccaro, AR, Patel T, Fischgrund J, Anderson DG, Truumees E, Herkowitz HN, et al. A pilot study evaluating the safety and efficacy of OP-1 Putty (rhBMP-7) as a replacement for iliac crest autograft in posterolateral lumbar arthrodesis for degenerative spondylolisthesis. Spine (Phila Pa 1976) 2004;2917:1885-1892.
266. Kanayama, M, Hashimoto T, Shigenobu K, Yamane S, Bauer TW, and Togawa D. A prospective randomized study of posterolateral lumbar fusion using osteogenic protein-1 (OP-1) versus local autograft with ceramic bone substitute: emphasis of surgical exploration and histologic assessment. Spine (Phila Pa 1976) 2006;3110:1067-1074.
267. Cahill, KS, Chi JH, Day A, and Claus EB. Prevalence, complications, and hospital charges associated with use of bone-morphogenetic proteins in spinal fusion procedures. JAMA 2009;3021:58-66.

268. Benglis, D, Wang MY, and Levi AD. A comprehensive review of the safety profile of bone morphogenetic protein in spine surgery. Neurosurgery 2008;625 Suppl 2:ONS423-431; discussion ONS431.
269. Paramore, CG, Lauryssen C, Rauzzino MJ, Wadlington VR, Palmer CA, Brix A, et al. The safety of OP-1 for lumbar fusion with decompression-- a canine study. Neurosurgery 1999;445:1151-1155; discussion 1155-1156.
270. Garrison, KR, Donell S, Ryder J, Shemilt I, Mugford M, Harvey I, et al. Clinical effectiveness and cost-effectiveness of bone morphogenetic proteins in the non-healing of fractures and spinal fusion: a systematic review. Health Technol Assess 2007;1130:1-150, iii-iv.
271. Visser, R, Arrabal PM, Becerra J, Rinas U, and Cifuentes M. The effect of an rhBMP-2 absorbable collagen sponge-targeted system on bone formation in vivo. Biomaterials 2009;3011:2032-2037.
272. Geiger, M, Li RH, and Friess W. Collagen sponges for bone regeneration with rhBMP-2. Adv Drug Deliv Rev 2003;5512:1613-1629.
273. Dahabreh, Z, Calori GM, Kanakaris NK, Nikolaou VS, and Giannoudis PV. A cost analysis of treatment of tibial fracture nonunion by bone grafting or bone morphogenetic protein-7. Int Orthop 2009;335:1407-1414.
274. Orthopaedic and Rehabilitation Devices Advisory Panel, USFaDA, Executive Summary for P050036 Medtronic's AMPLIFY™ rhBMP-2 Matrix. 2010.
275. Oest, ME, Dupont KM, Kong HJ, Mooney DJ, and Guldberg RE. Quantitative assessment of scaffold and growth factor-mediated repair of critically sized bone defects. J Orthop Res 2007.
276. Boerckel, JD, Dupont KM, Kolambkar YM, Lin AS, and Guldberg RE. In vivo model for evaluating the effects of mechanical stimulation on tissue-engineered bone repair. J Biomech Eng 2009;1318:084502.
277. Alsberg, E, Kong HJ, Hirano Y, Smith MK, Albeiruti A, and Mooney DJ. Regulating bone formation via controlled scaffold degradation. J Dent Res 2003;8211:903-908.
278. Rosenberg, L. Chemical basis for the histological use of safranin O in the study of articular cartilage. J Bone Joint Surg Am 1971;531:69-82.
279. You, JO, Park SB, Park HY, Haam S, Chung CH, and Kim WS. Preparation of regular sized Ca-alginate microspheres using membrane emulsification method. J Microencapsul 2001;184:521-532.
280. Kempen, DH, Lu L, Classic KL, Hefferan TE, Creemers LB, Maran A, et al. Non-invasive screening method for simultaneous evaluation of in vivo growth factor release profiles from multiple ectopic bone tissue engineering implants. J Control Release 2008;1301:15-21.
281. Kolambkar, YM, Peister A, Ekaputra AK, Hutmacher DW, and Guldberg RE. Colonization and Osteogenic Differentiation of Different Stem Cell Sources on Electrospun Nanofiber Meshes. Tissue Eng Part A 2010.
282. M, LI, Eriksen EF, and Bunger C. Bone morphogenetic protein-2 but not bone morphogenetic protein-4 and -6 stimulates chemotactic migration of human osteoblasts, human marrow osteoblasts, and U2-OS cells. Bone 1996;181:53-57.

283. Ruhe, PQ, Boerman OC, Russel FG, Spauwen PH, Mikos AG, and Jansen JA. Controlled release of rhBMP-2 loaded poly(dl-lactic-co-glycolic acid)/calcium phosphate cement composites in vivo. J Control Release 2005;1061-2:162-171.
284. Delgado, JJ, Evora C, Sanchez E, Baro M, and Delgado A. Validation of a method for non-invasive in vivo measurement of growth factor release from a local delivery system in bone. J Control Release 2006;1142:223-229.
285. Yamamoto, M, Takahashi Y, and Tabata Y. Controlled release by biodegradable hydrogels enhances the ectopic bone formation of bone morphogenetic protein. Biomaterials 2003;2424:4375-4383.
286. Peters, MC, Isenberg BC, Rowley JA, and Mooney DJ. Release from alginate enhances the biological activity of vascular endothelial growth factor. J Biomater Sci Polym Ed 1998;912:1267-1278.
287. Ruhe, PQ, Boerman OC, Russel FG, Mikos AG, Spauwen PH, and Jansen JA. In vivo release of rhBMP-2 loaded porous calcium phosphate cement pretreated with albumin. J Mater Sci Mater Med 2006;1710:919-927.
288. Woo, BH, Fink BF, Page R, Schrier JA, Jo YW, Jiang G, et al. Enhancement of bone growth by sustained delivery of recombinant human bone morphogenetic protein-2 in a polymeric matrix. Pharm Res 2001;1812:1747-1753.
289. Uludag, H, Gao T, Porter TJ, Friess W, and Wozney JM. Delivery systems for BMPs: factors contributing to protein retention at an application site. J Bone Joint Surg Am 2001;83-A Suppl 1Pt 2:S128-135.
290. Wang, Y, Zhang L, Hu M, Wen W, Xiao H, and Niu Y. Effect of chondroitin sulfate modification on rhBMP-2 release kinetics from collagen delivery system. J Biomed Mater Res A 2010;922:693-701.
291. Friess, W, Uludag H, Foskett S, Biron R, and Sargeant C. Characterization of absorbable collagen sponges as recombinant human bone morphogenetic protein-2 carriers. Int J Pharm 1999;1851:51-60.
292. Winn, SR, Uludag H, and Hollinger JO. Carrier systems for bone morphogenetic proteins. Clin Orthop Relat Res 1999;367 Suppl:S95-106.
293. Genes, NG, Rowley JA, Mooney DJ, and Bonassar LJ. Effect of substrate mechanics on chondrocyte adhesion to modified alginate surfaces. Arch Biochem Biophys 2004;4222:161-167.
294. Putnam, C. Protein Calculator v3.3. March 28, 2006 August 24, 2010]; Available from: http://www.scripps.edu/~cdputnam/protcalc.html.
295. Silva, EA and Mooney DJ. Spatiotemporal control of vascular endothelial growth factor delivery from injectable hydrogels enhances angiogenesis. J Thromb Haemost 2007;53:590-598.
296. Ruppert, R, Hoffmann E, and Sebald W. Human bone morphogenetic protein 2 contains a heparin-binding site which modifies its biological activity. Eur J Biochem 1996;2371:295-302.
297. Haidar, ZS, Hamdy RC, and Tabrizian M. Biocompatibility and safety of a hybrid core-shell nanoparticulate OP-1 delivery system intramuscularly administered in rats. Biomaterials 2010;3110:2746-2754.
298. Wei, G, Jin Q, Giannobile WV, and Ma PX. The enhancement of osteogenesis by nano-fibrous scaffolds incorporating rhBMP-7 nanospheres. Biomaterials 2007;2812:2087-2096.

299. Li, B, Yoshii T, Hafeman AE, Nyman JS, Wenke JC, and Guelcher SA. The effects of rhBMP-2 released from biodegradable polyurethane/microsphere composite scaffolds on new bone formation in rat femora. Biomaterials 2009;3035:6768-6779.
300. Brown, KV, Li B, Guda T, Perrien DS, Guelcher S, and Wenke JC. Improving Bone Formation in a Rat Femur Segmental Defect by Controlling BMP-2 Release. Tissue Eng Part A 2011.
301. Carter, DR, Van Der Meulen MC, and Beaupre GS. Mechanical factors in bone growth and development. Bone 1996;181 Suppl:5S-10S.
302. Baker, AH. Non-Union in Fractures. The Ulster Medical Journal 1934;34:277-283.
303. Mroz, TE, Wang JC, Hashimoto R, and Norvell DC. Complications related to osteobiologics use in spine surgery: a systematic review. Spine (Phila Pa 1976) 2010;359 Suppl:S86-104.
304. Axelrad, TW and Einhorn TA. Bone morphogenetic proteins in orthopaedic surgery. Cytokine Growth Factor Rev 2009;205-6:481-488.
305. Kolambkar, YM, Dupont KM, Boerckel JD, Huebsch N, Mooney DJ, Hutmacher DW, et al. An alginate-based hybrid system for growth factor delivery in the functional repair of large bone defects. Biomaterials 2010.
306. Guldberg, RE, Caldwell NJ, Guo XE, Goulet RW, Hollister SJ, and Goldstein SA. Mechanical stimulation of tissue repair in the hydraulic bone chamber. J Bone Miner Res 1997;128:1295-1302.
307. Case, ND, Duty AO, Ratcliffe A, Muller R, and Guldberg RE. Bone formation on tissue-engineered cartilage constructs in vivo: effects of chondrocyte viability and mechanical loading. Tissue Eng 2003;94:587-596.
308. Kolambkar, YM, Peister A, Ekaputra AK, Hutmacher DW, and Guldberg RE. Colonization and Osteogenic Differentiation of Different Stem Cell Sources on Electrospun Nanofiber Meshes. Tissue Engineering In press.
309. Junqueira, LC, Bignolas G, and Brentani RR. Picrosirius staining plus polarization microscopy, a specific method for collagen detection in tissue sections. Histochem J 1979;114:447-455.
310. Abramoff, MD, Magelhaes PJ, and Ram SJ. Image Processing with ImageJ. Biophotonics International 2004;117:36-42.
311. Clarke, KA. Differential fore- and hindpaw force transmission in the walking rat. Physiol Behav 1995;583:415-419.
312. Robling, AG. Is bone's response to mechanical signals dominated by muscle forces? Med Sci Sports Exerc 2009;4111:2044-2049.
313. Oxlund, H, Andersen NB, Ortoft G, Orskov H, and Andreassen TT. Growth hormone and mild exercise in combination markedly enhance cortical bone formation and strength in old rats. Endocrinology 1998;1394:1899-1904.
314. Kolambkar, YM, Dupont KM, Boerckel JD, Heubsch N, Mooney DJ, Hutmacher DW, et al. An Alginate-based Hybrid System for Growth Factor Delivery in the Functional Repair of Large Bone Defects. Biomaterials 2010;[Epub ahead of print].

315. Kanichai, M, Ferguson D, Prendergast PJ, and Campbell VA. Hypoxia promotes chondrogenesis in rat mesenchymal stem cells: a role for AKT and hypoxia-inducible factor (HIF)-1alpha. J Cell Physiol 2008;2163:708-715.
316. Cullinane, DM, Fredrick A, Eisenberg SR, Pacicca D, Elman MV, Lee C, et al. Induction of a neoarthrosis by precisely controlled motion in an experimental mid-femoral defect. J Orthop Res 2002;203:579-586.
317. Stoeger, T, Proetzel GE, Welzel H, Papadimitriou A, Dony C, Balling R, et al. In situ gene expression analysis during BMP2-induced ectopic bone formation in mice shows simultaneous endochondral and intramembranous ossification. Growth Factors 2002;204:197-210.
318. Rui, YF, Lui PP, Ni M, Chan LS, Lee YW, and Chan KM. Mechanical loading increased BMP-2 expression which promoted osteogenic differentiation of tendon-derived stem cells. J Orthop Res 2010.
319. Cuenca-Lopez, MD, Peris JL, Garcia-Rosello M, Atienza C, Prat J, Becerra J, et al. Action of recombinant human BMP-2 on fracture healing in rabbits is dependent on the mechanical environment. J Tissue Eng Regen Med 2010;47:543-552.
320. AAOS_Council_on_Research_and_Scientific_Affairs, Research Priorities for the United Research Agenda, A.A.o.O. Surgeons, Editor. 2003: Rosemont, IL.
321. Ando, J, Nomura H, and Kamiya A. The effect of fluid shear stress on the migration and proliferation of cultured endothelial cells. Microvasc Res 1987;331:62-70.
322. Krishnan, L, Underwood CJ, Maas S, Ellis BJ, Kode TC, Hoying JB, et al. Effect of mechanical boundary conditions on orientation of angiogenic microvessels. Cardiovasc Res 2008;782:324-332.
323. Joung, IS, Iwamoto MN, Shiu YT, and Quam CT. Cyclic strain modulates tubulogenesis of endothelial cells in a 3D tissue culture model. Microvasc Res 2006;711:1-11.
324. Wilson, CJ, Kasper G, Schutz MA, and Duda GN. Cyclic strain disrupts endothelial network formation on Matrigel. Microvasc Res 2009;783:358-363.
325. Sarmiento, A, Latta LL, and Tarr RR. The effects of function in fracture healing and stability. Instr Course Lect 1984;33:83-106.
326. Duvall, CL, Taylor WR, Weiss D, and Guldberg RE. Quantitative microcomputed tomography analysis of collateral vessel development after ischemic injury. Am J Physiol Heart Circ Physiol 2004;2871:H302-310.
327. Cowin, SC and Doty SB, Tissue mechanics. 2007, New York: Springer.xvi, 682 p.
328. Moutsatsos, IK, Turgeman G, Zhou S, Kurkalli BG, Pelled G, Tzur L, et al. Exogenously regulated stem cell-mediated gene therapy for bone regeneration. Mol Ther 2001;34:449-461.
329. Langenfeld, EM and Langenfeld J. Bone morphogenetic protein-2 stimulates angiogenesis in developing tumors. Mol Cancer Res 2004;23:141-149.
330. Deckers, MM, van Bezooijen RL, van der Horst G, Hoogendam J, van Der Bent C, Papapoulos SE, et al. Bone morphogenetic proteins stimulate angiogenesis through osteoblast-derived vascular endothelial growth factor A. Endocrinology 2002;1434:1545-1553.

331. van Royen, N, Piek JJ, Schaper W, and Fulton WF. A critical review of clinical arteriogenesis research. J Am Coll Cardiol 2009;551:17-25.
332. Egginton, S. Invited review: activity-induced angiogenesis. Pflugers Arch 2009;4575:963-977.
333. Barron, MJ, Tsai CJ, and Donahue SW. Mechanical stimulation mediates gene expression in MC3T3 osteoblastic cells differently in 2D and 3D environments. J Biomech Eng 2010;1324:041005.
334. Groothuis, A, Duda GN, Wilson CJ, Thompson MS, Hunter MR, Simon P, et al. Mechanical stimulation of the pro-angiogenic capacity of human fracture haematoma: involvement of VEGF mechano-regulation. Bone 2010;472:438-444.
335. Clarke, MS and Feeback DL. Mechanical load induces sarcoplasmic wounding and FGF release in differentiated human skeletal muscle cultures. FASEB J 1996;104:502-509.
336. Cao, R, Brakenhielm E, Pawliuk R, Wariaro D, Post MJ, Wahlberg E, et al. Angiogenic synergism, vascular stability and improvement of hind-limb ischemia by a combination of PDGF-BB and FGF-2. Nat Med 2003;95:604-613.
337. Kilarski, WW, Samolov B, Petersson L, Kvanta A, and Gerwins P. Biomechanical regulation of blood vessel growth during tissue vascularization. Nat Med 2009;156:657-664.
338. Matsumoto, T, Sasaki J, Alsberg E, Egusa H, Yatani H, and Sohmura T. Three-dimensional cell and tissue patterning in a strained fibrin gel system. PLoS One 2007;211:e1211.
339. Liu, Y, Manjubala I, Schell H, Epari DR, Roschger P, Duda GN, et al. Size and habit of mineral particles in bone and mineralized callus during bone healing in sheep. J Bone Miner Res 2010;259:2029-2038.
340. Manjubala, I, Liu Y, Epari DR, Roschger P, Schell H, Fratzl P, et al. Spatial and temporal variations of mechanical properties and mineral content of the external callus during bone healing. Bone 2009;452:185-192.
341. Uhrig, BA, Clements IP, Boerckel JD, Bellamkonda RV, and Guldberg RE. A Composite Injury Model of Severe Lower Limb Bone and Nerve Trauma. In Abstract presented at the Orthopaedic Research Society Meeting. 2011. Long Beach, CA.
342. Wehner, T, Wolfram U, Henzler T, Niemeyer F, Claes L, and Simon U. Internal forces and moments in the femur of the rat during gait. J Biomech 2010;4313:2473-2479.
343. Willett, N, M.T.A. L, Uhrig BA, Warren G, and Guldberg RE. Functional and Structural Analysis of Limb Restoration Using a Novel Rat Model of Composite Bone and Muscle Injury. In Abstract presented at the Orthopaedic Research Society Meeting. 2011. Long Beach, CA.
344. Folkman, J. Angiogenesis. Annu Rev Med 2006;57:1-18.
345. Norrby, K. In vivo models of angiogenesis. J Cell Mol Med 2006;103:588-612.
346. Staton, CA, Stribbling SM, Tazzyman S, Hughes R, Brown NJ, and Lewis CE. Current methods for assaying angiogenesis in vitro and in vivo. Int J Exp Pathol 2004;855:233-248.
347. Jain, RK, Schlenger K, Hockel M, and Yuan F. Quantitative angiogenesis assays: progress and problems. Nat Med 1997;311:1203-1208.

348. Baker, JH, Huxham LA, Kyle AH, Lam KK, and Minchinton AI. Vascular-specific quantification in an in vivo Matrigel chamber angiogenesis assay. Microvasc Res 2006;712:69-75.
349. Passaniti, A, Taylor RM, Pili R, Guo Y, Long PV, Haney JA, et al. A simple, quantitative method for assessing angiogenesis and antiangiogenic agents using reconstituted basement membrane, heparin, and fibroblast growth factor. Lab Invest 1992;674:519-528.
350. Guedez, L, Rivera AM, Salloum R, Miller ML, Diegmueller JJ, Bungay PM, et al. Quantitative assessment of angiogenic responses by the directed in vivo angiogenesis assay. Am J Pathol 2003;1625:1431-1439.
351. Akhtar, N, Dickerson EB, and Auerbach R. The sponge/Matrigel angiogenesis assay. Angiogenesis 2002;51-2:75-80.
352. Ley, CD, Olsen MW, Lund EL, and Kristjansen PE. Angiogenic synergy of bFGF and VEGF is antagonized by Angiopoietin-2 in a modified in vivo Matrigel assay. Microvasc Res 2004;683:161-168.
353. Lawley, TJ and Kubota Y. Induction of morphologic differentiation of endothelial cells in culture. J Invest Dermatol 1989;932 Suppl:59S-61S.
354. Lin, AS, Barrows TH, Cartmell SH, and Guldberg RE. Microarchitectural and mechanical characterization of oriented porous polymer scaffolds. Biomaterials 2003;243:481-489.
355. Koontz, JT, Charras GT, and Guldberg RE. A microstructural finite element simulation of mechanically induced bone formation. J Biomech Eng 2001;1236:607-612.